The University of Nottingham

Discrete Element Method (DEM) Modelling of Rock Flow and Breakage Within a Cone Crusher

By Huiqi Li

BEng, MSc

A Thesis submitted to The University of Nottingham

for the degree of Doctor of Philosophy

September, 2013

DECLARATION OF ORIGINALITY

Title of Thesis: *Discrete Element Method (DEM) modelling of rock flow and breakage within a cone crusher*

I declare that the thesis hereby submitted for the degree of Doctor of Philosophy at the University of Nottingham is my own work except as cited in the references and has not been previously submitted for any degree.

The following publications are fully related to the research work conducted in this PhD program:

Journal papers:

McDowell, G.R., Li, H. and Lowndes, I. (2011) The importance of particle shape in discrete element modelling of particle flow in a chute. *Geotechnique Letters* 1, No. 3, 59-64.

Li, H., McDowell, G.R. and Lowndes, I. (2012) A laboratory investigation and discrete element modelling of rock flow in a chute. *Powder Technology* 229, 199-205.

Li, H., McDowell, G.R. and Lowndes, I. (2013) Discrete element modelling of rock breakage using dense random packing agglomerates. *Géotechnique Letters 3*, No. July-September (2013): 98-102.

Cil, M.B., Alshibli, K.A., McDowell, G.R. and Li, H. (2013) Discussion: 3D assessment of fracture of sand particles using discrete element method. *Geotechnique Letters 3*, No January-March, 13-15

Conference paper:

McDowell, G. R., de Bono, J., Chen, C., Cai, W. Ferellec, J-F., Li, H. and Falagush, O., 2012. Recent applications of DEM in Geomechanics. 3rd international Workshop on Modern trends in Geomechanics,, Nottingham, UK.

Name: Li Huiqi

Signature:

Date:

ABSTRACT

A cone crusher is a crushing machine which is widely used in the mining, construction and recycling industries. Previous research studies have proposed empirical mathematical models to simulate the operational performance of a cone crusher. These models attempt to match the size distributions of the feed and product streams. The flow of the rock and its breakage within the cone crusher chamber are not explicitly modelled by these methods. Moreover, the ability to investigate the changes in crusher performance affected by changes to the crusher design geometry and/or operating variables (including cavity profile, closed size setting and eccentric speed) are not easily achieved. Improvements to system design and performance are normally achieved by the combination of iterative modifications made to the design and manufacture of a series of prototype machines, and from a subsequent analysis of the results obtained from expensive and time consuming rock testing programs. The discrete element method (DEM) has in recent years proved to be a powerful tool in the execution of fundamental research to investigate the behaviour of granular material flow and rock breakage. Consequently, DEM models may provide the computational means to simulate the flow and breakage of rock as it passes through a cone crusher chamber. Thus, the development of field validated models may provide a cost effective tool to predict the changes in crusher performance that may be produced by incremental changes made to the dimensions or power delivered to the crusher chamber. To obtain an improved understanding of the fundamental mechanisms that take place within a cone crusher chamber, the two processes of rock flow and rock

breakage may be decoupled. Consequently, this study firstly characterised the flow behaviour of broken rock through a static crusher chamber by conducting a series of experiments to investigate the flow of regular river pebbles down an inclined chute. A parallel computational study constructed and solved a series of DEM models to replicate the results of these experimental studies. An analysis of the results of these studies concluded that an accurate model replication of the shape of the pebbles and the method used to load the pebbles into the inclined chute were important to ensure that the DEM models successfully reproduced the observed particle flow behaviour. These studies also established relationships between the chute geometry and the time taken for the loaded pebble streams to clear the chute.

To investigate the rock breakage behaviour observed within a cone crusher chamber, thirty quasi-spherical particles of Glensanda ballast aggregate were diametrically crushed in the laboratory using a Zwick crushing machine. The crushed rock particles used were of three sieve size fractions: 14-28mm, 30-37.5mm and 40-60mm. The effects that either a variation in the particle size or strength has on and the number and size distribution of the progeny rock fragments produced on breakage were studied. Subsequently, a series of DEM simulation models were constructed and solved to replicate the experimental results obtained from these crushing tests. The aggregate particles were represented by agglomerates consisting of a number of smaller diameter bonded micro-spheres. A new method was proposed to generate a dense, isotropic agglomerate with negligible initial overlap between the micro-spheres by inserting particles to fill the voids in the agglomerate In addition, the effects that a variation in the particle packing configurations had on the simulated strength and breakage patterns experienced by the model agglomerate rock particles were investigated. The results from these DEM model studies were validated against the

experimental data obtained from the ballast rock breakage tests. A comparative analysis of the experimental and modelling studies concluded that once the bond strengths between the constituent micro-spheres matched the values determined from the rock breakage tests, then the numerical models were able to replicate the measured variations in the aggregate particle strengths.

Finally, the individual validated DEM aggregate particle flow and breakage modes were combined to construct a preliminary coupled prototype DEM model to simulate the flow and breakage of an aggregate feed through a cone crusher chamber. The author employed two modelling approaches: the population balance model (PBM) and bonded particle model (BPM) to simulate the observed particle breakage characteristics. The application of the PBM model was successfully validated against historical experimental data available in the literature. However, the potential wider use of the BPM model was deemed impractical due to the high computation time. From a comparative analysis of the particle size distributions of the feed and computed product streams by the two modelling approaches, it is concluded that the simpler PBM produces more practical computationally efficient numerical solutions.

Acknowledgements

Foremost, I would like to thank my first supervisor, Prof Glenn McDowell, for his excellent guidance, unflagging encouragement, and continuous advice throughout this research. His wisdom and insight have guided to me to conduct research of interest. Without his support, this thesis would not have been possible.

I also wish to express my gratitude to my second supervisor, Dr. Ian Lowndes, who has supported me throughout this project with his expert supervision and endless patience. I want to also thank Ian for serving me as a role model to me as a junior member of academic. He has been a strong and supportive adviser to me throughout my PhD career, but he has always given me great freedom to shape my ideas and interest.

My sincere thanks also goes to Dr. Jean-francois Ferellec, for his continuous help and valuable comments throughout this project.

I am also grateful to all the technicians in the School of Civil Engineering for their help with the experimentation, in particular Mel Hemsley, Bal Loyla and Michael Langford

Finally, my greatest gratitude goes to my parents, my sister and my girlfriend fort their endless love and support.

Contents

List of Figures

List of Tables

Notation

A_{cross}	Cross-sectional area of clump
α_{local}	Local damping coefficient
β	Bite angle
β_i	Critical damping ratio
b	Size effect factor
BPM	Bonded particle model
C_i	Damping constant
C_i^{crit}	Critical damping constant
CSS	Closed size setting
d	Particle size
D_i	Damping force in viscous damping system
F_i	The contact force vector
F_i^S	Shear component vector of the contact force
F_i^n	Normal component vector of the contact force
$F_{\max}^{\ s}$	Maximum allowable shear contact force

$F_c^{\ n}$	Normal contact bond strength
F_c^s	Shear contact bond strength
F^g	Generalized force
F^d	Damping force in local damping system
F_f	Diametrical fracture force
g_i	Body force acceleration vector
H_i	Angular momentum of the particle
HCP	Hexagonal closed packing
k^n, k^s	Normal and shear stiffness at the contact
m	Weibull modulus
M_i	Resultant moment acting on the particle
n_i	Unite Normal
P_s	Survival probability
OSS	Open size setting
rpm	Revolutions per minute
PBM	Population balance model
q	Octahedral stress

r_{max}, r_{min}	Maximum and minimum radius of micro-ball in dense random packing agglomerate
r_0	Radius ratio of dense random packing agglomerate
s	Eccentric throw
γ	Eccentric angle
U^n	The overlap between two entities.
V_{clump}	Volume of clump
V_i^s	Shear component of the contact velocity
ω_{spin}	Spinning angular velocity of the cone
ω_{ecc}	Eccentric angular velocity of the cone
$\dot{\omega}_i$	Angular velocity of the particle
$\ddot{x}_i$	Acceleration of particle
Δt	Incremental time step
ΔU_i^s	Shear component of the contact displacement-increment vector
ΔF_i^s	Shear elastic force-increment vector
$\sigma_1, \sigma_2, \sigma_3$	Principle stress in three directions
σ_o	37% tensile strength
$\sigma_{o,d}$	Stress for particles of size d such that 37% of tested particles survive

σ_{av}	Average tensile stress at failure
ε	Restitution coefficient

CHAPTER 1 INTRODUCTION

1.1 Background and problem definition

Rock comminution plays an important role in both the aggregate and wider mineral extractive industries as the extracted minerals cannot be effectively utilised until their extracted size distribution is reduced. This size reduction is achieved by comminution methods including the use of crushers. Cone crushers are one of the most common types of mineral crushing machine. Cone crushers have been widely used in the mining and aggregates industries to crush medium or above medium sized rock materials. Figure 1.1 shows a Maxtrak 1000 mobile cone crusher that are typically employed within small to medium sized surface aggregate rock quarries.

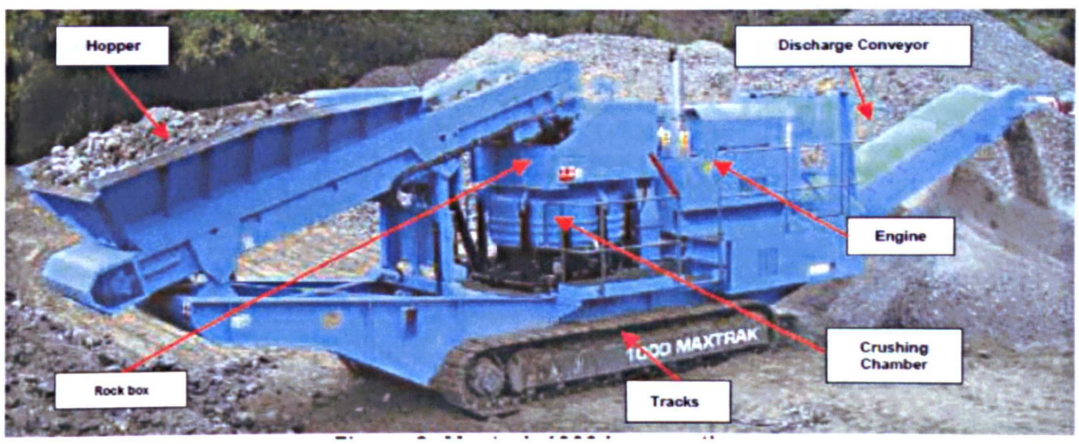

Figure 1.1A Maxtrak 1000 cone crusher in operation at a quarry

Although the operational design of cone crushers has experienced a significant improvement since the first models were developed in the mid-1920s, further improvements to the development of crusher performance have been restricted. Firstly,

it is proved difficult to successfully predict the crusher product in terms of the size distribution and shape of the rock particles. A number of previous researchers have addressed this problem, by the development and solution of iterative empirical models based on experimental observation (Gauldie, 1953; Whiten, 1972; Evertsson, 1997). These inverse solution methods attempt to match the size distributions of the feed and product streams. However, engineers have been unable to adapt these models to assist in the development of modified designs to improve the operational performance of these machines.

In particular, these iterative inverse solution models do not allow the design engineer to investigate the influence of the effects that changes to crusher variables such as the cavity profile, the cone throw or rotational speed settings may have on the crusher performance. The alternative use of an incremental build and test of design prototypes is both expensive, often requiring the production of several models to achieve the required production specification. For example, it can take eight to ten months to validate the result of a change of a cavity profile, which is very expensive and inefficient.

The development and application of validated computational simulation models of cone crushers would significantly reduce the lead time and costs. The discrete element method (DEM) (Cundall and Strack, 1979) provides a potential method with which to investigate the mechanical behaviour of the flow and breakage of granular material at both the micro and macro scales. The construction of DEM agglomerate particle models, include algorithms to represent the changes in the finite displacements, rotations and bonds between the discrete particles that form the agglomerates, when these agglomerates are subjected to an external load. The new position, rotation and

contacts that result from the application of these temporally changing applied loads are iteratively determined during the calculation process. These discrete particle body models may also be bonded together, to form more realistic composite rock models. This methodology has been employed by researchers to conduct studies to investigate the deformation and flow of granular materials. Over the past thirty years, DEM models have been widely used to investigate the mechanical behaviour of granular material. The results of some recent research studies might usefully be adapted to investigate the rock breakage and flow mechanisms observed within cone crushers., These include the models of rock breakage within ball mills investigated by Cleary (2001a), (2001b); and Cleary et al (2003). Thus, DEM models may provide a powerful tool with which to model the coupled flow and breakage of rocks within cone crushers.

1.2 Aims and Objectives

The aim of this project is to gain an improved fundamental understanding of the characteristics of rock flow and breakage within a cone crusher chamber by the use of validated DEM models.

The objectives of this project may be stated as:

1. To develop DEM models to replicate the flow and breakage observed within cone crushers
2. To develop a more fundamental understanding of the rock and machine parameters that contributes to the optimum flow and breakage of rock within cone crushers

3. To investigate the influence of chamber geometry on the predicted rock flow and breakage.
4. To investigate the role of the feed rock size distribution on the predicted product rock size distribution produced.
5. To validate the models developed against known machine and rock parameters.

Figure 1.2 shows the investigative strategy used during the execution of this research project to gain a greater understanding of flow and breakage occurred within the crushing chamber. Initially, the fundamental aggregate rock flow and breakage modes observed within the crusher chamber were decoupled and individually studied. Firstly, the gravity flow of rocks that occurs in the crusher chamber was investigated by performing a series of laboratory experiments of the flow of a collection of smooth regular shaped river gravel pebbles of a known particle size distribution from an inclined rectangular Perspex chute. as the chute charged with the pebbles is shown in figure 1.2. The results of the laboratory experiments were then used to validate the results of DEM models and to increase the understanding of the flow processes. Secondly, to develop an appropriate rock breakage model, a series of diametrical laboratory compression tests were performed on a sized collection of aggregate ballast particles.

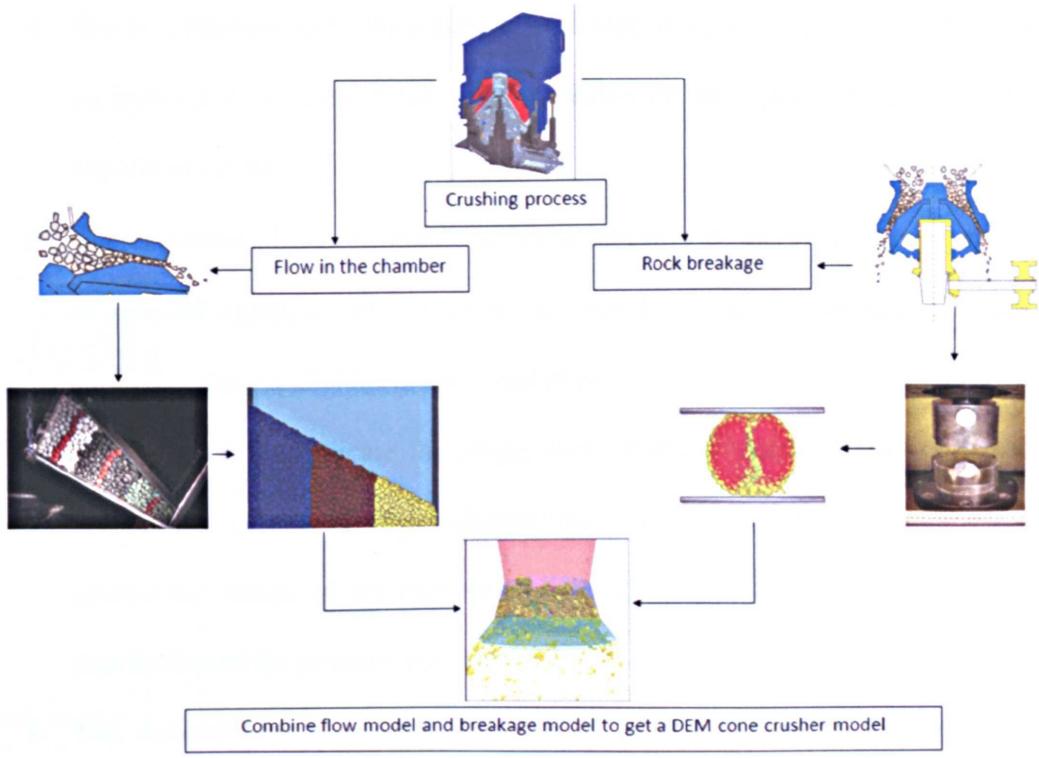

Figure 1.2 The strategy to model the cone crusher using the DEM

To achieve these aims, the following investigative methodology was adopted:

1. A critical literature review was performed to determine the methods used and the results obtained to characterise the principal mechanisms and parameters that govern the operation and performance of cone crushers. A critical literature review of rock comminution methods and the characterisation and analytical methods used to determine rock particle size.
2. A critical literature review to identify the fundamental principles and codes of practice that govern a robust construction and application of DEM and PFC^{3D}models.
3. A critical review of the literature that reports previous experimental studies that have investigated the flow of particles within an inclined chute.

4. The development and solution of DEM models to simulate particle flow down an inclined experimental chute. A validation of the model simulations with experimental data.
5. The execution of experimental studies to investigate the breakage of a range of sizes of aggregate rock particles subjected to vertical compression loads applied across parallel horizontal steel plates .
6. DEM models to replicate the single rock breakage characteristics observed above. The results of these simulations were compared to and validated against the results of the experimental work in terms of the shape and size distribution of the progeny particles.
7. The development and solution of DEM models to predict the flow and breakage of multiple particulate feeds through a cone crusher chamber.
8. A parametric model study to investigate the influence that the dimensions of the crusher chamber geometry have on the predicted rock flow and breakage determined from an examination of the particle size distributions within the product streams
9. The validation of the results predicted by the cone crusher models against actual field collected feed and product samples for a given rock type.
10. The identification of the physical operating characteristics of cone crushers that define the production of regular product size distributions and shape for given rock type feed size distributions.

1.3 Thesis outline

Chapter One presents a brief introduction to background behind the engineering problem investigated, provides a definition of the aims and objectives of the research studies proposed, and presents an outline of the experimental and computational modelling methodology that was adopted. Chapter Two details a summary of the theory behind the discrete element method (DEM) models used including, a definition of the calculation principles and a description of the relevant constitutive models employed from the PFC^{3D} (Itasca, 2008) code used in the execution of this project.

Chapter Three reports the results of a critical review of the results and conclusions of related research studies published in the literature. In particular, this chapter presents the research highlights of studies conducted to: establish the working mechanisms that govern the performance of cone crushers; identify the rock flow and breakage behaviours within the crusher chamber; develop and apply DEM models to granular material flow; establish basic theories to describe rock breakage; develop and apply DEM models to replicate rock breakage events; develop and apply iterative mathematical models to replicate the rock breakage experienced within cone crushers.

Chapter Four summarises the background behind and the results obtained from the fundamental experimental and DEM simulation studies conducted to characterise rock flow down an inclined chute. Two types of chute flow experiments were conducted. The first set of flow experiments employed a chute charged with a single sieve size of pebbles. The purpose of these experiments were to obtain a basic understanding of the flows of similar sized but differently shaped particulate, The second set of

experiments initially charged the chute with number of equal volume bands of particles. The sieve size of the particles loaded into each of the bands increased from the bottom (outlet) to the top (inlet) of the chute. These banded particulate sized flow experiments were conducted to investigate the nature of the flow of an incrementally size reducing particulate stream as it moves down the cone crusher chamber. Corresponding discussion of the development and application of DEM models to replicate the experimental observations are also presented in this chapter.

Chapter Five details the results of the experimental and computational modelling studies to investigate the compressive breakage of a series of sizes of aggregate rock particles. The experimental studies established data to describe the distribution of the particle strengths, the effect of particle size on particle strength and the size distribution of the progeny rock fragments. The simulation studies employed a novel algorithm with which to generate a dense random packing agglomerate to represent the initial rock particles.

Chapter Six presents the results of two forms of a coupled DEM model that simulates the combined flow and breakage of a feed of rock particles as they move through the cone crusher chamber. The particle breakage may be modelled either using the PBM or the BPM algorithm.

Chapter Seven presents a review of the major conclusions and research contributions made by this study and a discussion of the potential future extensions that may be pursued.

CHAPTER 2

LITERATURE REVIEW OF THE DISCRETE ELEMENT METHOD

2.1 Introduction

The discrete element method or distinct element method (DEM) is a numerical method to compute the motion and locations of a large number of micro and macro sized particles and was first proposed by Cundall (1971). Cundall and Strack (1979) firstly applied the discrete element method (DEM) to model granular materials. The results of these initial numerical and experimental photo elastic studies confirmed that DEM is a valid tool with which to investigate the fundamental behaviour of granular materials. Parallel with the development of increased computational capacity, DEM has been increasingly used to investigate the micro mechanical behaviour of granular materials. However, some of the micro property effects, such as particle shape, interparticle friction, contact constitutive law and fabric (i.e. particle arrangement and orientation), are not yet fully understood,.

DEM is now widely used to investigate a wide range of engineering problems associated with granular or discontinuous materials, including: granular flows, powder mechanics, and rock mechanics. To model granular materials, the use of DEM enables the user to investigate the influence of a number of parameters many of

which are not easily measured in laboratory experiments. These parameters include: interparticle friction, the distribution of contact forces, the particle coordination number, and the particle movements. Furthermore, the use of a DEM model allows the user to consistently employ an identically distributed initial particulate sample size distribution subjected to a range of different loading. Therefore, unlike experimental sample preparation methods, the DEM models ensure that the material properties of the initial samples put under load are identical. This chapter also introduces the reader to the fundamental models employed by DEM and presents an overview of the computational model solution algorithms employed by the PFC^{3D} commercial code that is employed by this study.

2.2 Introduction to the discrete element method

The discrete element method was first developed by Cundall (1971) to study rock mechanics problems and was later extended to investigate granular materials by Cundall and Strack (1979). Cundall and Hart (1992) defined the scope of the application of the discrete element method and summarized fundamental principles governing the modelling of discrete element systems. In their definition, the DEM permits the computation of the finite displacement and rotation of discrete bodies, including complete detachment, and automatically recognises the establishment of new contacts as the calculation progresses.

The DEM models granular materials as packed assemblies of discrete elements. This method is based on the use of an explicit numerical scheme in which the interaction of the particles is modelled contact by contact and the relative motion of the particles is

modelled particle by particle. Therefore, the DEM makes it possible to analyse the mechanics of granular materials at both the micro and macro scale (Itasca, 2008).

In the DEM, the interaction of the particles is treated as a dynamic process, whereby a state of equilibrium exists whenever the internal forces balance. The contact forces and displacements of a stressed assembly of particles are found by tracing the movements of the individual particles. Movements result from the propagation through the particle system of disturbances caused by specified wall and/or particle motion, and body forces (Itasca, 2008).

The dynamic behaviour is represented numerically by a time-stepping algorithm in which it is assumed that the velocities and accelerations are constant within each time-step. The solution scheme is identical to that used by the explicit finite difference method for continuum analysis. DEM is based upon the idea that the time-step is so small that, during a single time-step, disturbances cannot propagate from any particle further than its immediate neighbours. Then, at all times, the forces acting on any particle are determined exclusively by its interaction with the particles with which it is in contact.

The calculations in DEM are based on two laws: the application of Newton's second law to the particles, and a force-displacement law at the contacts between the particles. Newton's second law is used to calculate the motion of each particle arising from the contact and body forces acting upon it. The force-displacement law is used to evaluate the contact force from the computed displacement, and then to update the contact forces arising from the relative motion determined at each contact point.

2.3 PFC^{3D} particle-flow model

As described by Cundall and Strack (1979), the computational algorithms used by the PFC^{3D} code, employ the distinct element method (DEM) to model the movement and interaction of spherical particles. The resultant simulation models are formed by a collection of distinct spheres that displace independently of one another and interact only at the contact or interfaces between the particles. The modelling assumptions made by the PFC^{3D} computational algorithms are:

1. The particles are treated as rigid bodies
2. The contacts occur over a vanishingly small area
3. A soft-contact approach is used to define the contacts, such that the rigid particles are allowed to overlap with one another at the contact points.
4. The magnitude of the overlap permitted between adjacent particles is related to the contact force via the force-displacement law.
5. Bonds can exist at the contacts between particles.
6. All particles are spherical. However, the use of clump logic is permitted which supports the creation of super-particles of arbitrary shape. Consequently, each created clump consists of a set of overlapping spheres, and acts as a rigid body with a deformable boundary. (Lu, M., 2007)

In the construction of PFC^{3D} simulation models, the spherical particles and walls are defined as the two basic entities. Walls allow the user to apply velocity boundary conditions to assemblies of balls to simulate compaction or confinement. The balls and walls interact with one another via the forces that arise at the contacts. The PFC^{3D} code is suitable to model the stress-strain response of a granular material whose deformation results primarily from the sliding and rotation of the rigid particles and

the interlocking at the particle interfaces. More complex behaviours of granular materials may be modelled by allowing the particles to be bonded together at their contact points, so that internal forces are allowed to develop at the contacts. An outline of the basic conceptual models and mathematical principles employed by the PFC^{3D} code are presented in the following sections.

2.4 The calculation procedures of the PFC^{3D} code

The computational solution of a simulation model created with the PFC^{3D} code requires the repeated application of the law of motion to each particle in each calculation cycle. A Contact that initially exist between adjacent balls and/or a ball and a wall, may be broken and/or additional contacts formed during the simulation (Zhou et al, 2006).

The calculation cycle used by the PFC^{3D} code is a time-stepping algorithm that requires: the repeated application of the law of motion to each particle, a force-displacement law to each contact, and a constant update of the wall positions. Figure 2.1 illustrates the calculation cycle. At the start of each time-step, the contacts are updated from the particle and wall positions. The force-displacement law is then applied to each contact to update the contact forces based on the relative motion between the two contacted entities and the contact constitutive model. Then, the law of motion is applied to each particle to update its velocity and position based on the resultant force and the moment arising from the contact forces and any body forces acting on the ball. Also the wall positions are updated based on the specified wall velocities.

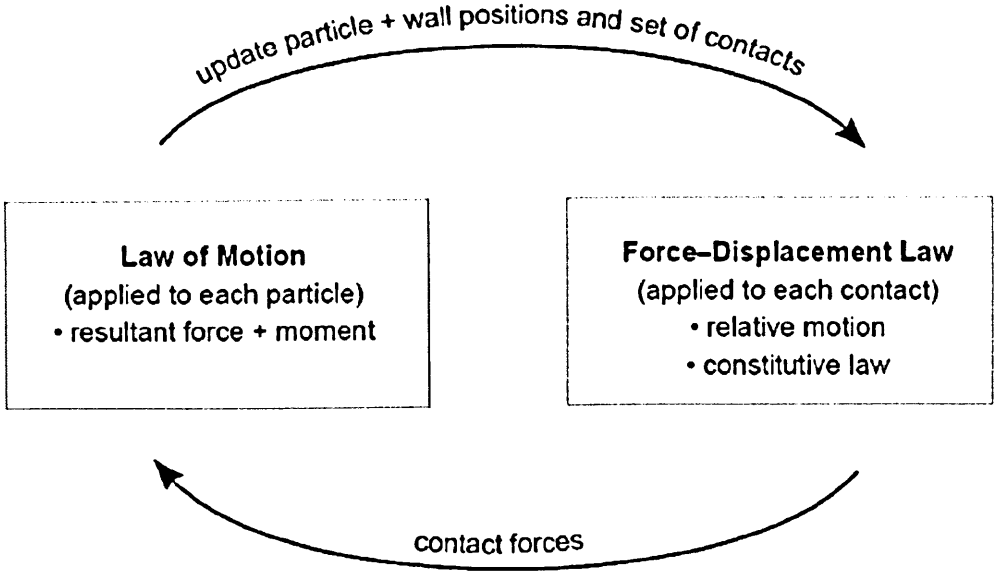

Figure 2.1 Calculation cycle use by the PFC^{3D} computational code (Itasca, 2008)

Force-Displacement Law

The contact force vector F_i can be resolved into normal and shear components with respect to the contact plane and expressed as:

$$F_i = F_i^s + F_i^n \qquad \textbf{Equation 2-1}$$

Where F_i^n and F_i^s stand for the normal and shear component vectors respectively.

The force displacement law relates the relative displacement between two entities at a contact to the contact force acting on the entities via the normal and shear stiffness computed at the contact. The normal contact force vector is calculated by the evaluation of the expression:

$$F_I^n = K^n U^n n_i \qquad \textbf{Equation 2-2}$$

Where K^n is the normal stiffness at the contact, computed from the application of the current contact-stiffness model. n_i is the unit normal and U^n is the overlap between the two entities. (Itasca, 2008)

The shear contact force is calculated in an incremental fashion. When the contact is formed, the total shear contact force is initialized to zero. Each subsequent incremental change in the relative shear-displacement increment produces an incremental increase in the elastic shear force. The shear component of the contact displacement-increment vector that occurs over an incremental time step, Δt, is calculated as:

$$\Delta U_i^s = V_i^s \Delta t \qquad \textbf{Equation 2-3}$$

where V_i^s is the shear component of the contact velocity respect to the contact plane.

The shear elastic force-increment vector is calculated by the evaluation of the expression:

$$\Delta F_i^s = -k^s \Delta U_i^s \qquad \textbf{Equation 2-4}$$

where k^s stands for the shear stiffness at the contact.

Finally, the new shear contact force is calculated by a summation of the shear force vectors present at the start of the time step, where the shear elastic force increment vector is evaluated from the expression (Itasca, 2008):

$$F_i^s = \{F_j^s\}^{old} + \Delta F_i^s \qquad \textbf{Equation 2-5}$$

Law of Motion

The motion of a single particle is determined by a resolution of the resultant force and the moment vectors acting upon it. The equations of motion may be expressed as two vector equations. One of the equations of motion relates the resultant force to the translational motion, as:

$$F_i = m(\ddot{x}_i - g_i) \qquad \textbf{Equation 2-6}$$

where F_i is the resultant force, m is the total mass of the particle, and g_i is the body force acceleration vector. The other equation of motion relates the resultant moment to the rotational motion, as

$$M_i = \dot{H}_i \qquad \textbf{Equation 2-7}$$

where M_i is the resultant moment acting on the particle, and H_i is the angular momentum of the particle. For a spherical particle of radius R with uniform density, Equation 2-7 may be written to define the global-axis system as

$$M_i = I\dot{\omega}_i = (\frac{2}{5}mR^2)\dot{\omega}_i \qquad \textbf{Equation 2-8}$$

The equations of motion, given by Equations 2-6 and 2-8, are integrated using a centred finite-difference procedure involving a time-step of Δt. The quantities $\dot{x}_i$ and ω_i, are computed at the mid-time-step intervals of $t \pm n\Delta t/2$, while the quantities x_i, $\ddot{x}_i$, $\dot{w}_i$, F_i, and M_i are computed at the primary intervals of $t \pm n\Delta t$. The accelerations are calculated from an evaluation of the expressions:

$$\ddot{x}_i^{(t)} = \frac{1}{\Delta t}(\dot{x}_i^{(t+\Delta t/2)} - \dot{x}_i^{(t-\Delta t/2)}) \qquad \textbf{Equation 2-9}$$

$$\dot{\omega}_i^{(t)} = \frac{1}{\Delta t}(\omega_i^{(t+\Delta t/2)} - \omega_i^{(t-\Delta t/2)})$$ **Equation 2-10**

Inserting these expressions into Equations 2-6 and 2-8 and solving for the velocities at time t±Δt/2 result in:

$$\dot{x}_i^{(t+\Delta t/2)} = \dot{x}_i^{(t-\Delta t/2)} + (\frac{F_i^{(t)}}{m} + g_i)\Delta t$$ **Equation 2-11**

$$\omega_i^{(t+\Delta t/2)} = \omega_i^{(t-\Delta t/2)} + (\frac{M_i^{(t)}}{I})\Delta t$$ **Equation 2-12**

Finally, the position of the particle centre for the next cycle is calculated from an evaluation of the expression:

$$x_i^{(t+\Delta t)} = x_i^{(t)} + \dot{x}_i^{(t+\Delta t/2)} \Delta t$$ **Equation 2-13**

2.5 Contacts constitutive models in PFC^{3D}

The overall constitutive behaviour of a material may be simulated by a model constructed with the PFC^{3D} code by associating a simple constitutive model to each contact. Three parallel models may be simultaneously resolved at the ball-wall or ball-ball contacts. These three model components, define the contact force-displacement behaviour, as shown in figure 2.2. A dashpot model is always used to model either system damping or energy dissipation. The behaviour experienced at contacts are normally modelled using a linear or Hertz model. The simulation of a parallel bond is achieved by the addition of a parallel-bond component to a contact. A description of all of these is detailed in the following sections.

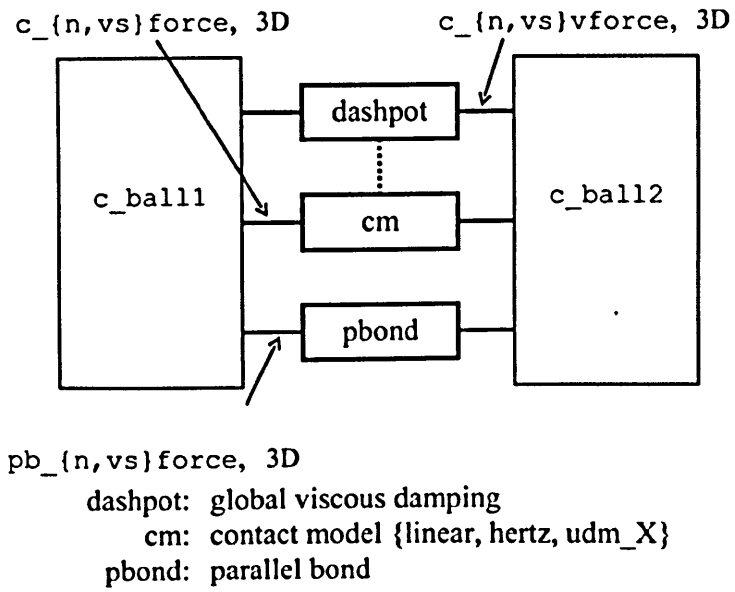

Figure 2.2 Components at a contact in PFC^{3D} (Itasca, 2008)

2.5.1 The damping system employed within PFC3D

Energy supplied to a system of particles is dissipated through frictional sliding. The damping algorithms available within PFC^{3D} code may be employed to dissipate energy by effectively damping the governing equations of motion. In the PFC^{3D} code, system damping systems may be achieved by the application of a local or viscous damping model.

Local Damping

The local damping model available in the PFC^{3D} code is similar to that described in Cundall (1987). It is easily implemented by the addition of a damping force to the equations of motion, given by equations 2-6 and 2-8, given by the following expression

$$F^g + F^d = M\ddot{x}_i \qquad \text{Equation 2-14}$$

Where F^g and M are the generalized force and mass components respectively, F^g includes the contribution from gravity, and F^d is the damping force. The damping force is calculated as:

$$F^d = -\alpha_{local} F^g \qquad \text{Equation 2-15}$$

Here α_{local} means local damping coefficient whose default value is 0.7.

The application of a local damping model has the following advantages:

1, Only the accelerated motion is damped, therefore, no erroneous damping forces arise from the steady-state motion

2, The damping constant, α_{local}, is non-dimensional.

3, Since damping is frequency-independent, regions of the model assembly with different natural periods are damped equally, by using the same damping constant.

However, the local damping coefficient is just an artificial value which may be inappropriate in some cases, for example where as the particles are in free flight under gravity or where a large group of particles are driven by a specified-velocity boundary condition.

Viscous Damping

As the focus of this research, is dynamic particle flow, that the use of a local damping system is not appropriate. To obtain a realistic energy dissipation, it is necessary to set all of the local damping coefficients to zero and to employ viscous damping.

When the viscous damping models are active, normal and shear dashpots are added at each contact. These dashpots act in parallel with the existing contact model-for example, the linear contact model as shown in Figure 2.3. A damping force, D_i (i=n:normal, s:shear), is added to the contact force, in which the normal and shear components are given by the expression:

$$D_i = C_i|V_i| \qquad \textbf{Equation 2-16}$$

Where C_i is the damping constant, V_i is the relative velocity at the contact, and the damping force acts to oppose the normal direction of motion. The damping constant is not specified directly; instead the critical damping ratio β_i is specified, and the damping constant satisfies the equation:

$$C_i = \beta_i C_i^{crit} \qquad \textbf{Equation 2-17}$$

Where C_I^{crit} is the critical damping constant.

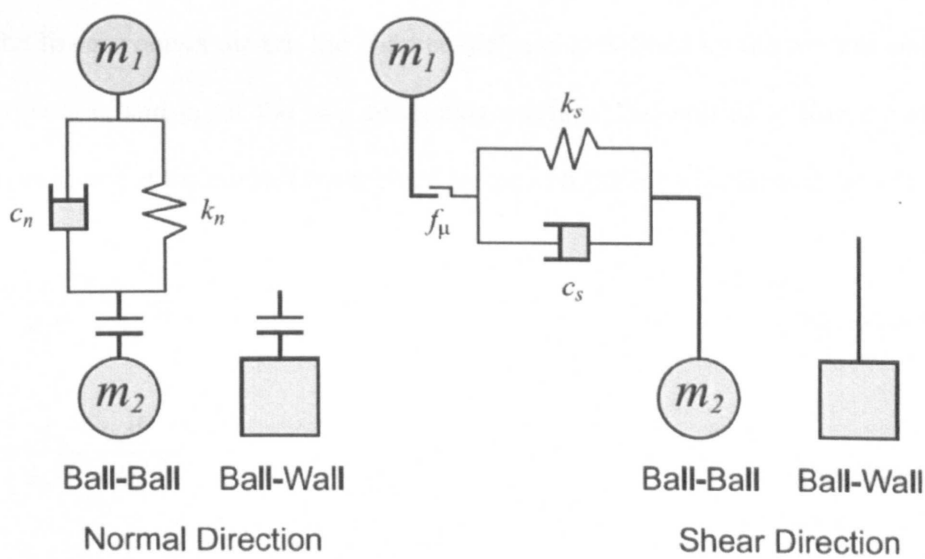

Figure 2.3 Viscous damping activated at a contact using the linear contact model (Itasca, 2008)

$$C_I^{crit} = 2mw_i = 2\sqrt{mk_i}$$ **Equation 2-18**

Where w_i is the natural frequency of the undamped system, k_i is the contact tangent stiffness, and m is the effective system mass. In the case of a ball-wall contact, m is taken as the ball mass, whereas in the case of ball-ball contact, m is taken as the average mass of the two contacting balls. Therefore the critical damping ratio β is given by (Ginsberg and Genin, 1984)

$$\beta = \frac{C_i}{2\sqrt{mk_i}}$$ **Equation 2-19**

2.5.2 Contact models

The PFC^{3D} code provides the user with two standard basic contact models : the linear and Hertzian contact models. The models establish two different contact stiffnesses.

Linear contact model

For the linear contact model, the contact stiffness is defined by the normal and shear stiffnesses, k_n and k_s, of the two contacting entities. The normal stiffness and shear stiffness acting at the contact are derived by the solution of equations 2-20 and 2-21

$$K^n = \frac{k_n^{[A]} k_n^{[B]}}{k_n^{[A]} + k_n^{[B]}}$$ **Equation 2-20**

$$K^s = \frac{k_s^{[A]} k_s^{[B]}}{k_s^{[A]} + k_s^{[B]}}$$ **Equation 2-21**

Where the superscripts [A] and [B] denote the two entities in contact.

Hertz contact model

The Hertz-Mindlin contact model is a nonlinear contact formulation based on an approximation of the theory proposed by Mindlin and Deresiewicz (1953) and described in Cundall (1988). However, this model is strictly only applicable to the case of spheres in contact, and therefore does not reproduce the continuous nonlinearity observed under shear. The model is defined in terms of the shear modulus, G, and the Poisson's ratio, ν, of the two contacting balls. The normal stiffness and shear stiffness acting at the contact are given by the expression:

$$K^n = \left(\frac{2\tilde{G}\sqrt{2\tilde{R}}}{3(1-\tilde{\nu})}\right)\sqrt{U^n} \qquad \textbf{Equation 2-22}$$

$$K^s = \left(\frac{2(\tilde{G}^2\ 3(1-\tilde{\nu})\tilde{R})^{1/3}}{2-\tilde{\nu}}\right)\left|F_i^n\right|^{1/3} \qquad \textbf{Equation 2-23}$$

Where U^n is the sphere overlap, and $\left|F_i^n\right|$ is the magnitude of the normal contact force. The multipliers to both of these equations are a function of the geometric and material properties of the two entities in contact. For ball-ball contact, the multipliers depend on the following properties:

$$\tilde{R} = \frac{2R^A R^B}{R^A + R^B} \qquad \textbf{Equation 2-24}$$

$$\tilde{G} = \frac{1}{2}(G^A + G^B) \qquad \textbf{Equation 2-25}$$

$$\tilde{\nu} = \frac{1}{2}(\nu^A + \nu^B) \qquad \textbf{Equation 2-26}$$

Where, G, is the elastic shear modulus; ν, is Poisson's ratio; R, is sphere radius and the superscripts A and B denote the two spheres in contact. For the case of a ball-wall contact, the wall is replaced by an identical ball positioned symmetrically about the wall location.

2.5.3 Parallel bond

A parallel bond between two particles may be envisaged as a finite sized piece of cementitious material acting over a circular cross-section lying between the particles. The parallel bond can transmit both forces and moments between the particles. The constitutive behaviour of the parallel bond model is shown in the Figure 2.4. As a result of the parallel bond stiffness, any relative motion at the contact causes a force and a moment to develop within the bond material. The parallel bond model breaks when either of these normal and shear maximum stresses exceeds the corresponding parallel bond strength.

The total force and moment associated with a parallel bond are denoted by $\bar{F}_i$ and $\bar{M}_i$, with the convention that this force and moment represent the action of the bond on sphere B in the Figure 2.4,. Each of these vectors may be resolved into normal and shear components with respect to the contact plane given by the equations:

$$\bar{F}_i = \bar{F}_i^n + \bar{F}_i^s \qquad \textbf{Equation 2-27}$$

$$\bar{M}_i = \bar{M}_i^n + \bar{M}_i^s \qquad \textbf{Equation 2-28}$$

Where $\bar{F}_i^n, \bar{F}_i^s$ and $\bar{M}_i^n, \bar{M}_i^s$ denote the normal and shear component vectors respectively. These vectors are shown in Figure 2.4, where the parallel bond is depicted as a cylinder of elastic material, the incremental normal and shear component vectors may be expressed by :

$$\Delta F_i^n = (-k^n A \Delta U^n) n_i \qquad \textbf{Equation 2-29}$$

$$\Delta F_i^s = -k^s A \Delta U^n \qquad \textbf{Equation 2-30}$$

$$\Delta M_i^n = (-k^n J \Delta \theta^n) n_i \qquad \textbf{Equation 2-31}$$

$$\Delta M_i^s = -k^n I \Delta \theta^s \qquad \textbf{Equation 2-32}$$

The maximum tensile and shear stresses acting on the bond periphery can becalculated by:

$$\sigma_{max} = \frac{-\bar{F}^n}{A} + \frac{\left|\bar{M}_i^s\right|}{I}\bar{R} \qquad \textbf{Equation 2-33}$$

$$\tau_{max} = \frac{\left|\bar{F}_i^s\right|}{A} + \frac{\left|\bar{M}^n\right|}{J}\bar{R} \qquad \textbf{Equation 2-34}$$

Where, *A*, is the area of the bond disk; *J*, is the polar moment of inertia of the disc cross-section; *I*, is the moment of inertia of the disc cross-section about an axis through the contact point; and $\bar{R}$ is the radius of the bond disc. The values of these parameters may be calculated from the expressions:

$$\bar{R} = \varphi R_{min} \qquad \textbf{Equation 2-35}$$

$$A = \pi \bar{R}^2$$ **Equation 2-36**

$$J = \frac{1}{2}\pi \bar{R}^4$$ **Equation 2-37**

$$I = \frac{1}{4}\pi \bar{R}^4$$ **Equation 2-38**

where φ is an input value of parallel bond radius multiplier, $R_{\min}$ represents the minimum radius of the two bonded balls.

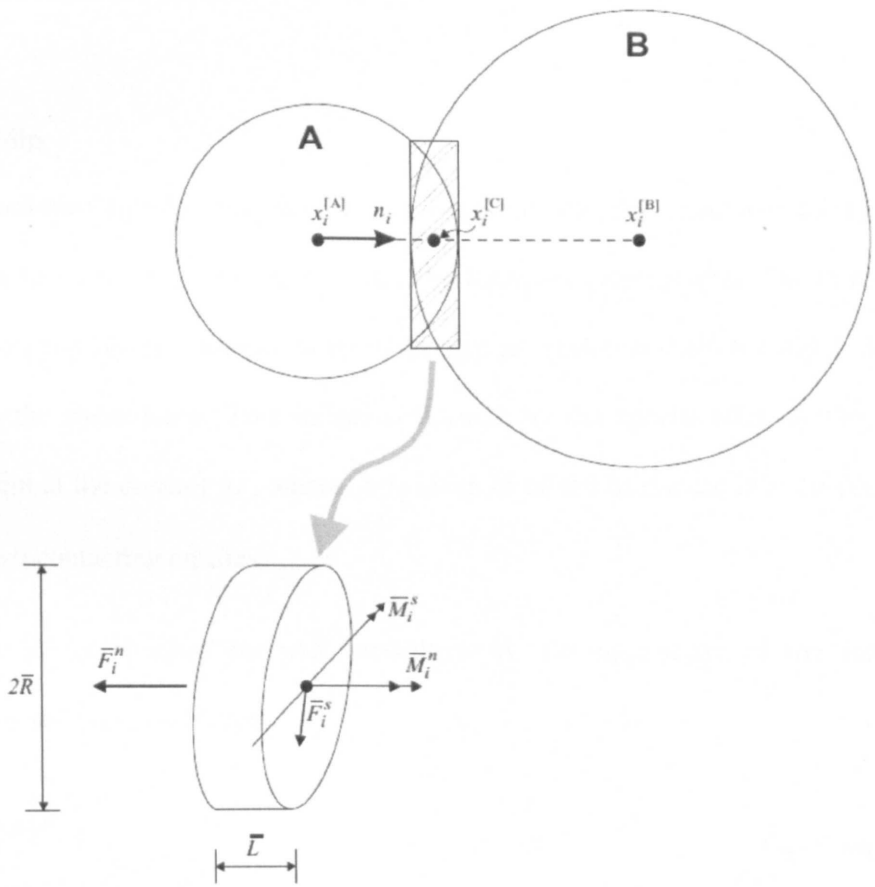

Figure 2.4 Parallel bond depicted as a cylinder of cementitious material (Itasca, 2008)

2.6 Component behaviour

The application of the contact model introduced in section 2.5 may result in the production of three types of system behaviour: stiffness, slip and bonding.

2.6.1 Stiffness

The relationship between the contact stiffnesses and the contact forces and relative displacements in the normal and shear directions are described by equations 2-2 and 2-4. The contact stiffnesses differ for the linear and Hertz contact models, as described in section 2.5.2.

2.6.2 Slip

Slip is initiated by the introduction of a coupling between shear and normal force, such that the two contacting entities may slip relative to one another. The introduction of this relationship provides no normal strength in tension and allows slip to occur by limiting the shear force. This model is defined by the specification of the friction coefficient at the contact μ, where μ is taken to be the minimum friction coefficient of the two contacting entities.

The contact is checked for slip conditions by the calculation of the maximum allowable shear contact force:

$$F_{max}{}^{s} = \mu \left| F_i^{n} \right| \qquad \textbf{Equation 2-39}$$

Slip is allowed to occur if $\left|F_i^{s}\right| > F_{max}{}^{s}$. The magnitude of F_i^{s} will be set equal to $F_{max}{}^{s}$ in the next iterative calculation cycle.

2.6.3 Bonding

The PFC^{3D} code contains a class of sub models that allow particles to be bonded together at contacts. The two standard bonding models are the contact bond and parallel bond. Both bonds can be envisioned as a glue, invisibly joining the two particles. The concept and use of parallel bond models has been introduced in section 2.5.3. A contact bond can be envisaged as, an infinitesimally small piece of glue, being formed by a pair of elastic springs that possess constant normal and shear stiffnesses acting at the contact point. These two springs have specified shear and tensile normal strengths. The magnitude of the shear contact force is limited by the shear contact bond strength and the tensile force that may be developed at a contact in the contact bonds. The magnitude of the tensile normal contact force is determined from the normal contact bond strength.

A contact bond consists of a combination of a normal contact bond strength F_c^n and shear contact bond strength F_c^s. If the magnitude of the tensile normal contact force equals or exceeds the normal contact bond strength, the bond will break, and both the normal and shear contact forces are set to zero. If the magnitude of the shear contact force equals or exceeds the shear contact force, or equals or exceeds the shear bond strength, the bond will break. However, for these cases the contact forces are not altered, provided that the shear force does not exceed the friction limit, and provided that the normal force is compressive.

The force-displacement behaviour relating the normal and shear components of a contact force and the relative displacement for particle contacts that occur at a point is shown in Figure 2.5. Either the contact bond or the slip behaviour is active at any

given time. Note that additional force and moment may also be acting if a parallel bond is present.

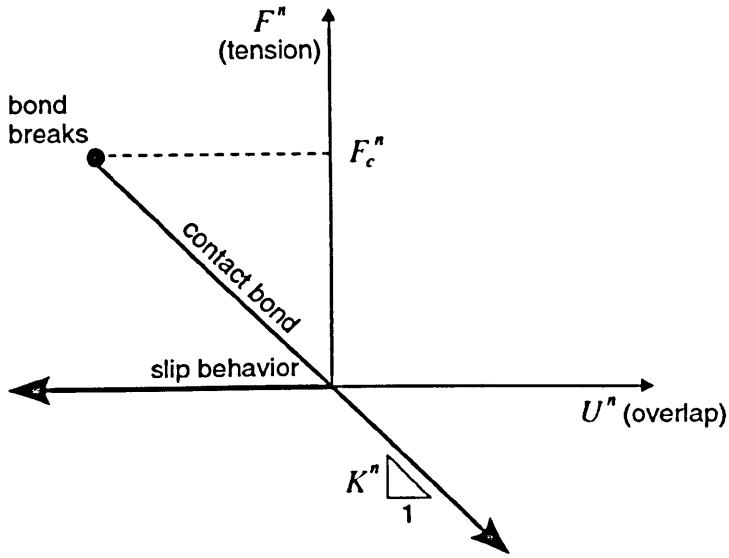

(a): Normal component of contact force

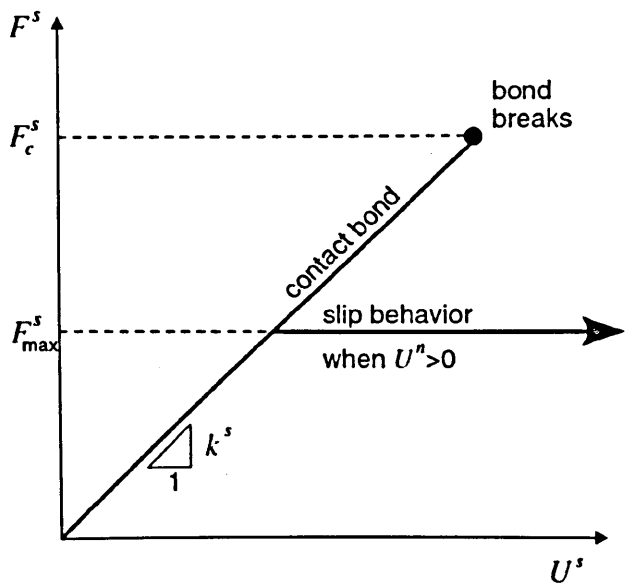

(b): shear component of contact force

Figure 2.5: Constitutive behaviour of contact occurring at a point (Itasca, 2008)

2.7 Clump logic

A clump is a single entity of overlapping balls and behaves as a rigid body (i.e. the balls comprising the clump remain at a fixed distance from each other). During the execution of the calculations, internal overlapping contacts are ignored to save on the computational time as compared to when all the contacts are active. Thus, a clump acts as a rigid body (with a deformable boundary) that will not break apart, regardless of the forces acting upon it. In this sense, a clump differs from a group of particles that are bounded to one another.

The total mass of a clump, m, with a centre of mass of clump located at, $x_i^{[G]}$, and the moments and products of inertia I_{ii} and I_{ij}, are defined by the following equations:

$$m = \sum_{p=1}^{N_p} m^{[p]} \qquad \textbf{Equation 2-40}$$

$$x_i^{[G]} = \frac{1}{m} \sum_{p=1}^{N_p} m^{[p]} x_i^{[p]} \qquad \textbf{Equation 2-41}$$

$$I_{ii} = \sum_{p=1}^{N_p} \left\{ m^{[p]} \left(x_j^{[p]} - x_j^{[G]} \right) \left(x_j^{[p]} - x_j^{[G]} \right) + \frac{2}{5} m^{[p]} R^{[p]} R^{[p]} \right\} \qquad \textbf{Equation 2-42}$$

$$I_{ij} = \sum_{p=1}^{N_p} \left\{ m^{[p]} \left(x_i^{[p]} - x_i^{[G]} \right) \left(x_j^{[p]} - x_j^{[G]} \right) \right\} (j \neq i) \qquad \textbf{Equation 2-43}$$

Where N_p is the number of balls that form the clump, $m^{[p]}$, is the mass of a ball, $x^{[p]}$, is the centroid location of the ball and , $R^{[p]}$, is the radius of the ball.

The motion of a clump is determined by the resultant force and moment vectors acting upon it. Because a clump is treated as a rigid body, its motion may be described in

terms of the translational motion of the entire clump. The equation representing this translational motion may be written in the vector from

$$F_i = m(\ddot{x}_i - g_i)$$ **Equation 2-44**

Where, F_i, is the resultant force (i.e., the sum of all externally-applied forces acting on the clump) and , g_i, is the body force acceleration vector arising from gravity loading.

The equation for rotational motion may be written in the vector form

$$M_i = \dot{H}_i$$ **Equation 2-45**

where, M_i, is the resultant moment about the centre of mass, and , $\dot{H}_i$, is the time rate-of-change of the angular momentum of the clump.

The resultant moment in Eq. (2-41) is computed by

$$M_i = \sum_{p=1}^{N_p}\left(\tilde{M}_i^{[p]} + \varepsilon_{ijk}\left(x_j^{[p]} - x_j^{[G]}\right)F_k^{[p]} + \sum_{c=1}^{N_c}\varepsilon_{ijk}\left(x_j^{[c]} - x_j^{[p]}\right)F_k^{[p,c]}\right)$$ **Equation 2-46**

where , $\tilde{M}_i^{[p]}$, is the externally-applied moment acting on particle (p), $F_k^{[p]}$, is the resultant force acting on particle (p) at its centroid, and , $F_k^{[p,c]}$,is the force acting on particle (p) at contact (c).

The time rate-of-change of the angular momentum for a system can be written as

$$\dot{H}_i = \alpha_i I_{ii} - \alpha_j I_{ij} + \varepsilon_{ijk}\omega_j(\omega_k I_{kk} - \omega_l I_{kl}) \ (j \neq i, l \neq k)$$ **Equation 2-47**

Where $\alpha_i = \dot{\omega}_i$.

2.8 Summary

DEM has been used by many researchers to model geotechnical problems. The basic concepts and general mathematical background to the model algorithms available within the commercial PFC^{3D} computational code have been reviewed. DEM is a powerful tool with which to conduct fundamental research into the behaviour of granular materials. The main disadvantage of DEM simulation is the enormous potential computational expense, as often the solution to many problems requires the use of very small time or spatial increments to ensure accuracy and numerical stability. In addition the models often require the use of a large number of discrete particles to ensure a sufficient number of contacts. DEM enables the user to investigate particle properties which cannot be obtained using conventional continuum mechanics, including: particle-particle friction, contact force distribution and coordination numbers. As circular (2D) or spherically (3D) shaped particles can roll and thus lead to a lower strength of the assembly, researchers have proposed clump models to represent complex particle shapes. These clump models, constructed from an amalgamation of a number of spherical particles, constrain the rotation of the constituent circular/spherical particles. The accuracy of the DEM models to granular materials and rock mechanics is highly dependent on the determination of the correct physical particle parameters, including the particle shape, rotation and friction coefficient.

CHAPTER 3 LITERATURE REVIEW OF CONE CRUSHER RESEARCH STUDIES

3.1 Introduction

This chapter is divided into four sub sections. Section 3.2 introduces the reader to the types of modern crusher machines employed in the minerals extraction and construction industries. In particular, this section provides an overview of engineering design and general working principles of cone crushers. Section 3.3 presents a critical review of the recent research studies published in the literature that have studied the use of DEM models to investigate the flow of granular material. The extension of the use of DEM models to study rock breakage is reviewed in Section 3.4. , Section 3.5 concludes this chapter by providing a critical review of the research published in the literature that have developed empirical mathematical models that replicate the flow and breakage of rock streams within cone crushers.

3.2 The cone crusher

3.2.1 Crushers and the cone crusher

Crushing is the first mechanical stage in the process of comminution in which the main objective is either the liberation of the valuable minerals from the gangue (Wills and Napier-Munn, 2006) or the production of aggregate for construction materials. The earliest crusher machines developed included stamp mills and super heavy duty

flour grinding mills. In recent times, the main crushers employed have been the jaw, gyratory and cone crushers. (Napier-Munn et al, 1996)

A jaw crusher has distinctive operational and design features, which consist of two plates which open and shut like the jaws of an animal (Grieco and Grieco, 1985). Figure 3.1 shows the structure of jaw crusher in operation. The jaws are set an acute angle to each other, and one jaw is pivoted so that is swings relative to the other fixed jaw. Material fed into the jaws is alternately nipped and released to fall further under gravity into the crushing chamber. Another important feature of all jaw crushers is the heavy flywheel attached to the drive, which is necessary to store energy on the idling half of the stroke and deliver it on the crushing half. Jaw crushers are also limited in capacity for their weight and size as they work only on a half-cycle (Wills and Napier-Munn, 2006). Therefore, due to its alternate loading and release of stress, it must be very rugged and needs to be set in strong foundations to accommodate the vibrations.

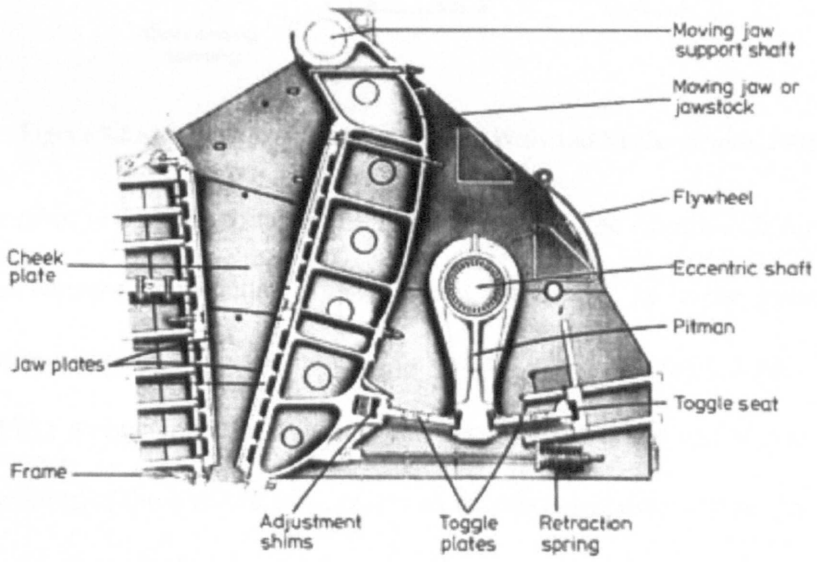

Figure 3.1 Structure of Jaw Crusher (Wills and Napier-Munn, 2006)

Gyratory crushers are mainly used on surface crushing plants and a few currently operate in underground mines (Wills and Napier-Munn, 2006). Figure 3.2 shows the structural components of a gyratory crushing machine. It can be seen the gyratory crusher consists essentially of a long spindle, carrying a hard steel conical grinding element, the head, seated in an eccentric sleeve. Material travels downwards between the two surfaces being progressively crushed until it is small enough to fall out through the gap between the two surfaces.

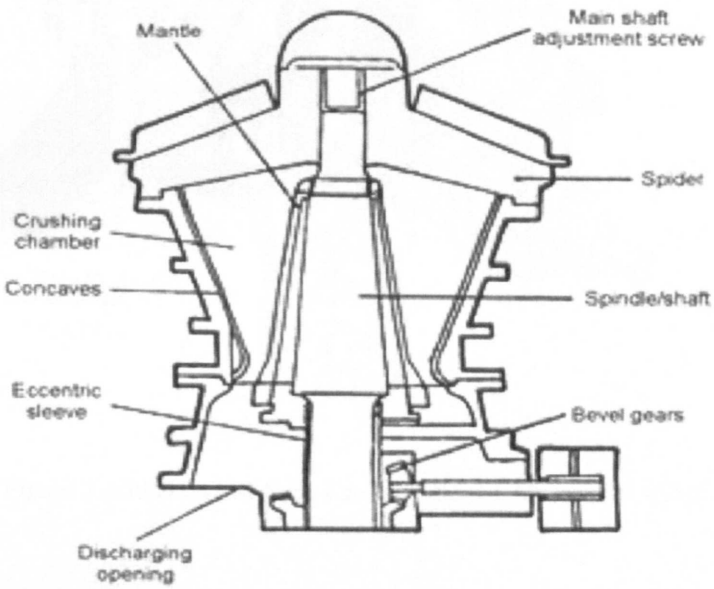

Figure 3.2 Structure of Gyratory Crusher (Wills and Napier-Munn, 2006)

A cone crusher is a modified from of gyratory crusher. The essential difference is that the shorter spindle of the cone crusher is not suspended, as in the gyratory, but is supported in a curved, universal bearing below the gyratory head or cone. The mantle is shaped like a cone and attached at a stationary bearing at the top and an off centred rotating bearing at the bottom; this creates an eccentric gyrating action. Taking a cross sectional cut through the chamber essentially shows that the crushing action of the

rotating cone and mantle effectively act as two jaw crushers working back to back. Figure 3.3 shows the structure of cone crusher (Wills and Napier-Munn, 2006).

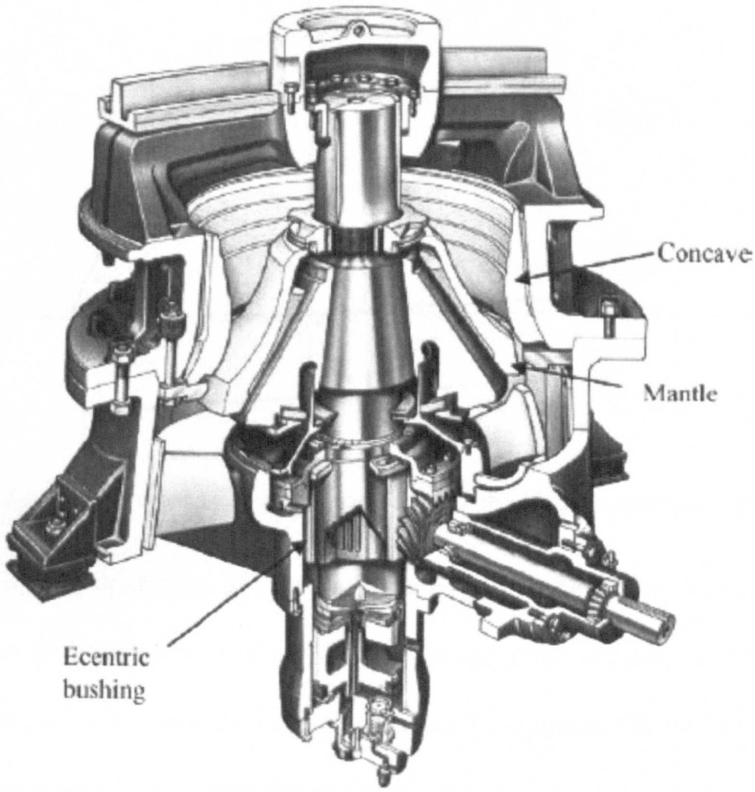

Figure 3.3 Structure of Cone Crusher (Napier-Munn et al, 1996)

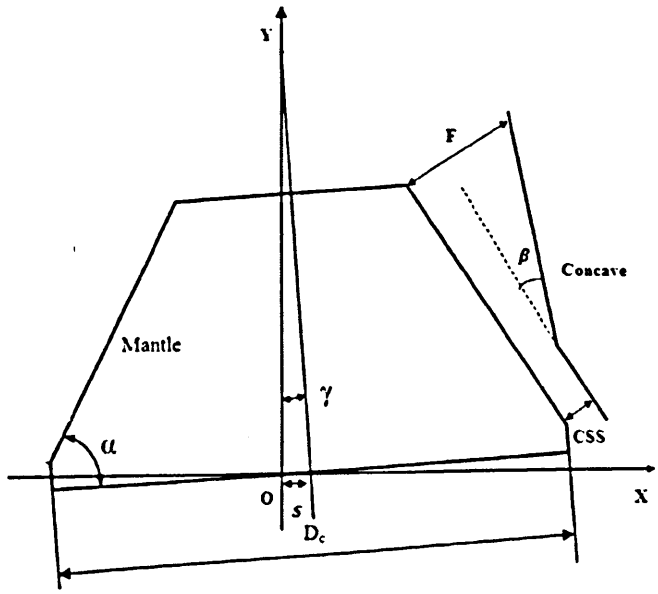

Figure 3.4 Vertical cross-section of a cone crusher showing the operation principle

Fig 3.4 shows the operating principles of a cone crusher. The eccentric gyratory motion of the mantle when a cross section of the cone crusher is taken shows a cyclically motion of backwards and forwards of the mantle. Therefore the distance between concave and mantle will change over time. The furthest distance is named as the Open Size Setting (OSS) while the smallest distance is known as Closed Size Setting (CSS). Taking a fixed point in the chamber the distance between the mantle and concave will vary as shown in figure 3.5. The distance between the surfaces of the mantle and concave periodically changes from between the CSS to OSS over a rotation of 2π. The number of OSS and CSS settings that a given rock particle will experience as it travels down the chamber is dependent on the revolutions per minute (rpm) of the mantle. The CSS is the point at which the material will be under compression and during which potential breakage will occur. The periodic opening of the chamber to the OSS setting will allow the compressed material to relax and to flow down the chamber. This is a step wise motion with the CSS decreasing each time.

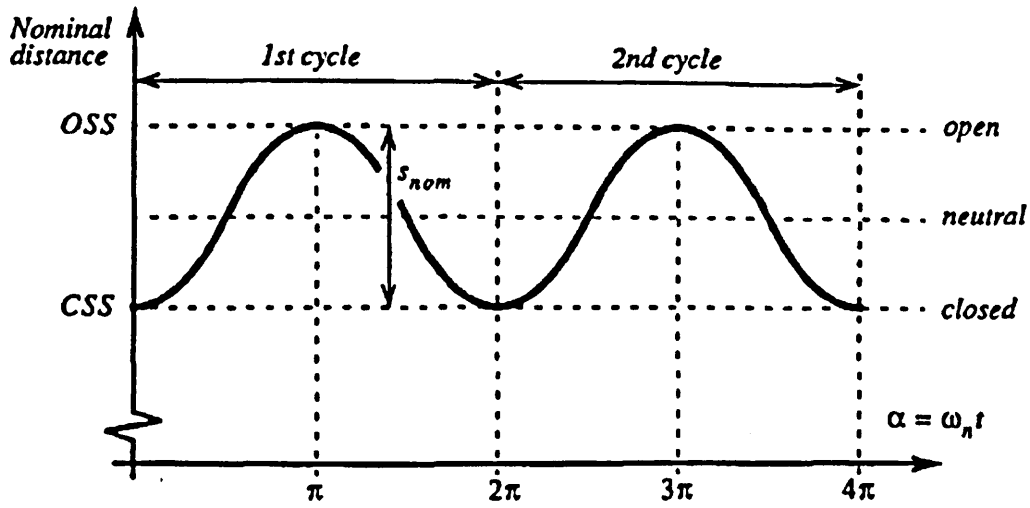

Figure 3.5 Fixed point in the chamber the distance between mantle and concave varies with time (Evertsson, 2000)

3.2.2 Design and performance parameters of a cone crusher

Closed side setting

The Closed side setting (CSS) (see figure 3.4) is the most commonly used parameter to adjust the degree of comminution achieved by a crushing machine and thus influence the product particle size distribution. The laboratory experiments performed by Karra (1983) concluded that the CSS has the largest influence on the product size distribution. The later work of Evertsson (2000) confirmed that the CSS affects the product particle size distribution due to change in the distance between the mantle and concave, which changes the crushing ratio and capacity of the machine. The effects on the product size distribution effected by a change in the CSS crusher parameter is shown in figure 3.6.

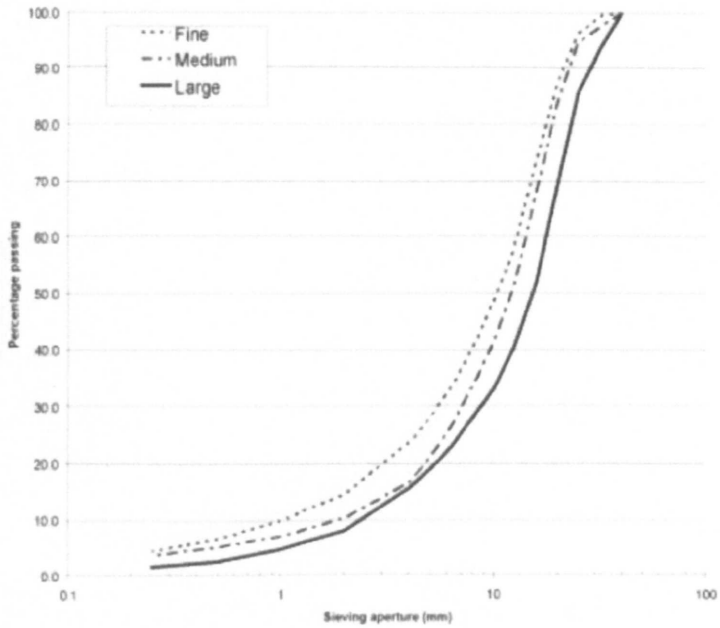

Figure 3.6 The effect that a change in the CSS has on the product size distribution (Hulthen, 2010).

Eccentric rotational speed

Eccentric rotational speed also has a significant on the size distribution of the product produced by a cone crusher. The eccentric rotational speed affects the number of material compressions experienced by a single rock particle as it travels through the crusher chamber, and thus the effective compression ratio, and resultant particle size distribution of product. Figure 3.7 shows the effect of the eccentric rotational speeds on the product size distribution delivered by a hydrocone crusher for the same feed stream size distribution.

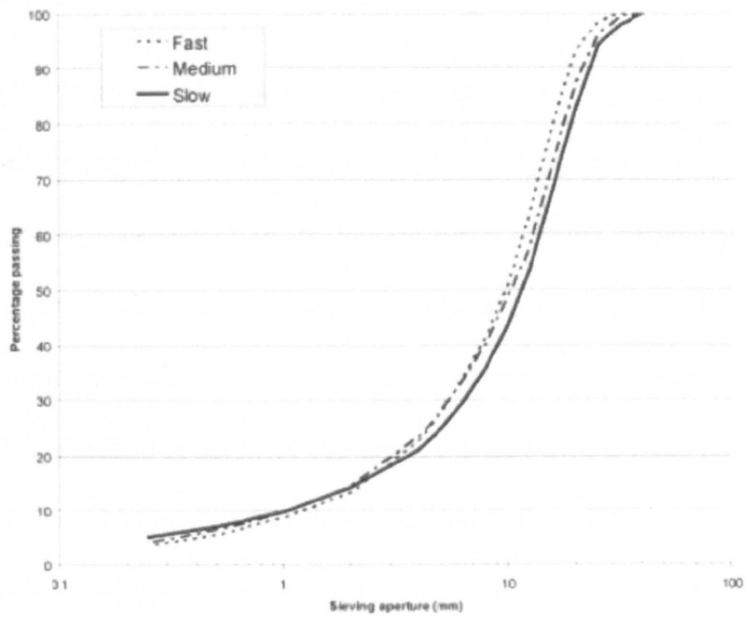

Figure 3.7 The effect of eccentric speed on the product size distribution (Hulthen, 2010).

Stroke

Stroke

The stroke is the eccentric distance the cone moves during half a rotation. However, this is a machine parameter that should not be adjusted or controlled during operation (Hulthen, 2010). The eccentric throw controls the amplitude of the sinusoidal rotations around the pivot points.

3.3 Literature review of crusher rock flow models

3.3.1 Rock flow models within cone crushers

Evertsson (1999) classified the flow of a particle or a volume of material in a cone crusher chamber into three different states of motion::

- Sliding
- Free fall

- Squeezing

Evertsson (1999) proposed a model that defined sliding to mean that particles slides along the mantle surface when it is in contact with the mantle. Free fall is assumed to occur if the local acceleration of the mantle surface in the vertical direction exceeds the acceleration of gravity. Particles are assumed to be squeezed when mantle is moving towards concave. Following every reduction cycle, corresponding to one revolution of eccentric rotation of the cone, the downward rock flow transport will consist of sliding and/or free fall depending on the eccentric rotational speed. The three eccentric speed regions which result due to the different combinations of particle motion states are more fully described below.

Speed region I

At low rotational speeds the motion of the descending rock particles is purely determined by a sliding motion. Only sliding will occur until the mantle starts to return from the OSS to the CSS at which point the particles will be nipped and breakage may occur. This defines the particle motion behaviour within the speed region I. The transport mechanisms experienced within this speed region are shown as Figure 3.8.

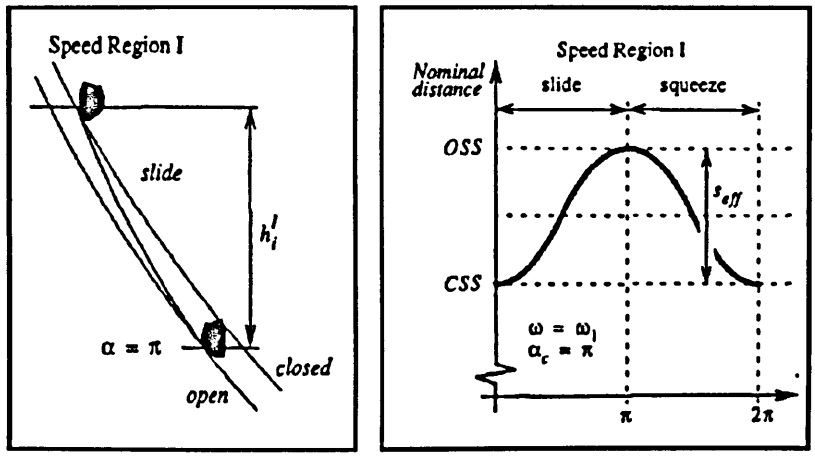

Figure 3.8 Transport mechanisms proposed within the speed region II for the cone crusher flow model (Evertsson, 1999)

Speed region II

As figure 3.9 shows, if the eccentric speed is high enough to give the mantle surface a vertical acceleration exceeding gravity, the particle will experience free fall until the particle catches up with the mantle and will then continue its motion of sliding if the mantle is still moving away from concave (nominal distance changing from CSS to OSS).

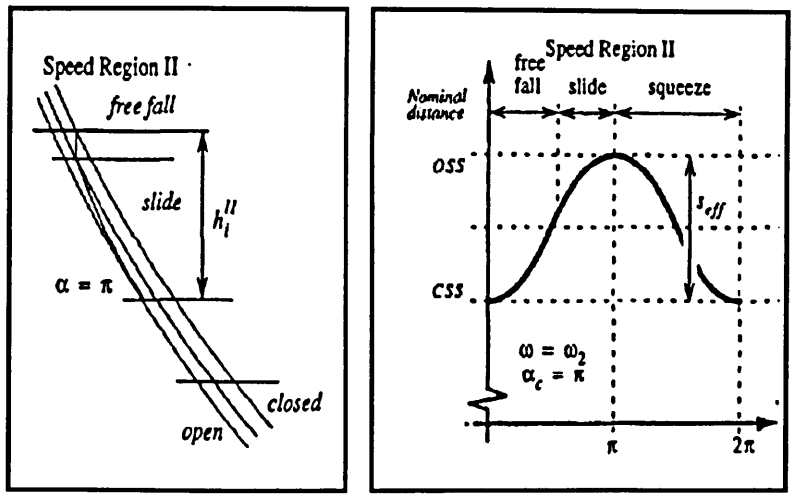

Figure 3.9 Transport mechanisms proposed within the speed region II for the cone crusher flow model (Evertsson, 2000)

Speed region III

If the eccentric speed continues to increase, it approaches the speed region III. In this speed region, the vertical acceleration of the mantle is larger than gravity, such that the particle will firstly experience a free fall motion as experienced n speed region II. However, the difference in this case is that the mantle has already moved towards the concave when the particle catches up with the mantle. Consequently, a particle will experience no sliding during the whole revolution, as shown in figure 3.10.

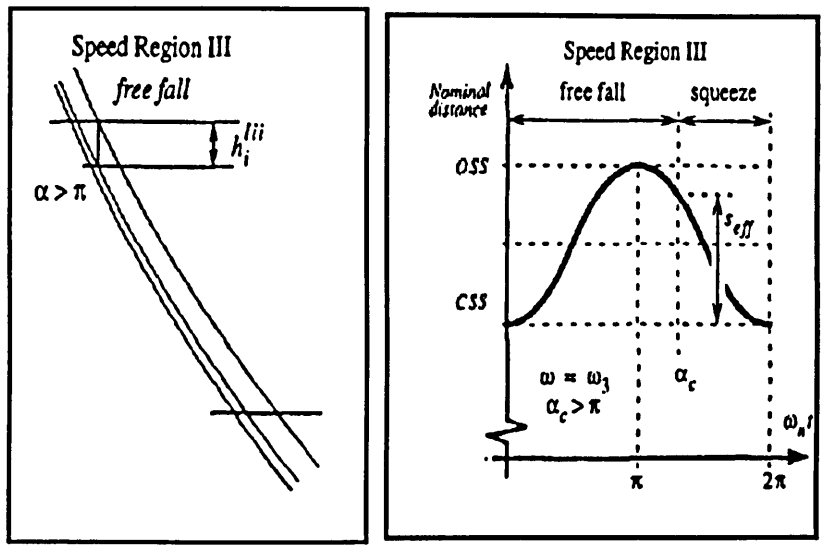

Figure 3.10 Transport mechanisms proposed within speed region III of the cone crusher flow model (Evertsson, 2000)

3.3.2 DEM models of granular material flow

A review of the literature has concluded that to date DEM models have not been employed to study the flow of rock within cone crusher chambers... However, DEM models have been used extensively to study a range of similar materials processing and handling applications, including granular flow in hoppers (Langston et al, 2009; Mack et al, 2011; Li et al, 2009; and Cleary and Sawley, 2002) and soybeans flows down inclined chutes (Zhang and Vu-Quoc, 2000; Vu-Quoc et al, 1999 and Zhang et al, 2004).

Zhang and Vu-Quoc (2000) constructed and solved a series of DEM models to simulate the flow of soybean down an inclined chute and over a rough discharge sheet. They conducted both laboratory experiments and DEM model simulation studies. Figure 3.11 shows a schematic representation of the experimental apparatus used. The total length of the chute is 3.42m and the width is of 0.152m. Glass beads of 3.0mm in

diameter were attached to the bottom discharge surface to make it bumpy. The angle of inclination of the discharge chute could be adjusted to apply different forces with which to drive the material flow. A high-speed video camera was set up to give a perpendicular view through a plexi-glass window which formed one side of the discharge chute surface. The video was able to record the flow of the particles down the chute.

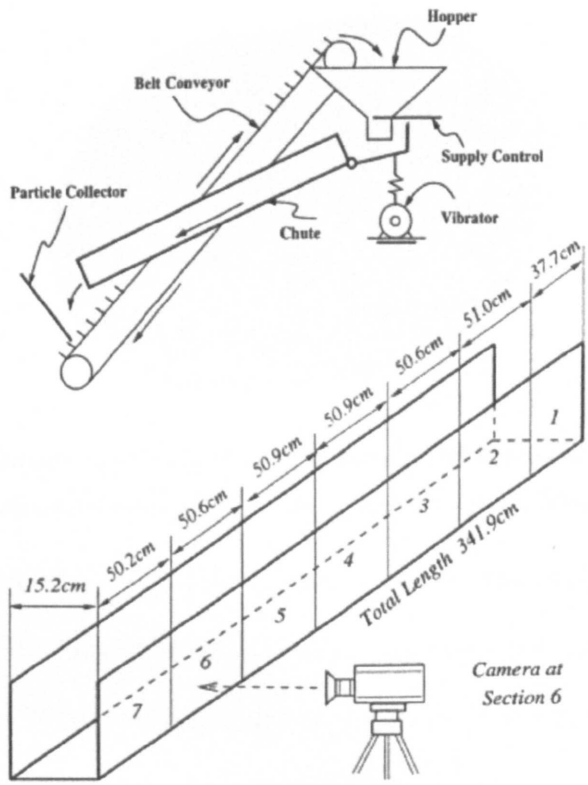

Figure 3.11 The experimental apparatus: overall set up(top), chute and camera position (bottom) (Zhang and Vu-Quoc, 2000).

Ellipsoid shapes were used to represent the soybean within the DEM simulation models. They used agglomerates formed from four spheres of the same diameter to replicate the ellipsoid particulates. The centres of the four balls were positioned on the same horizontal plane (figure 3.12). The radius of the spheres and the distance

between the centres of the spheres was adjusted to replicate the different geometries of individual soybean. The chute simulation model was initially charged with 1200 randomly distributed ellipsoidal particles. On the opening of the discharge gate at the base of the inclined chute, the observed average velocity of the particle flows were computed using the successive positions of individual particles determined from an analysis of successive photographic stills obtained from the fast video recordings..

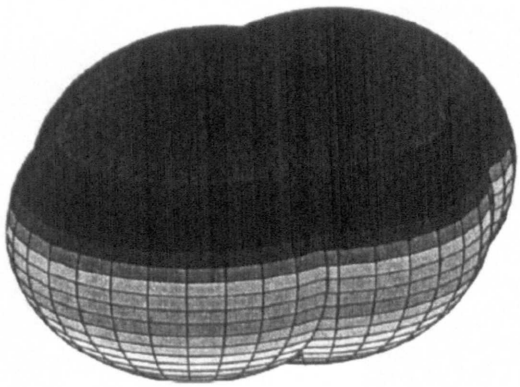

Figure 3.12 Geometric modelling of an ellipsoidal particle for contact detection: A clump of four spheres (Zhang and Vu-Quoc, 2000)

The authors subsequently compared a series of steady state model animation stills obtained from the 3D unsteady-state flow DEM model simulations with experimental steady state stills. They concluded that the computed average velocities of the simulated granular flows were in good agreement with the observed experimental velocities. Moreover, there was good quantitative and qualitative agreement of the velocity profile observed and predicted adjacent to the plexi-glass wall. It is noted that the restitution coefficient was calibrated by a drop test and the stiffness was measured from a series of single soybean compression tests.

Mack et al (2009) subsequently conducted experimental and DEM models studies using spherical particles to investigate the flow of granular materials in a hopper.

Figure 3.13 illustrates photographs of the experimental rigs and a schematic representation of the corresponding DEM models employed in their research.

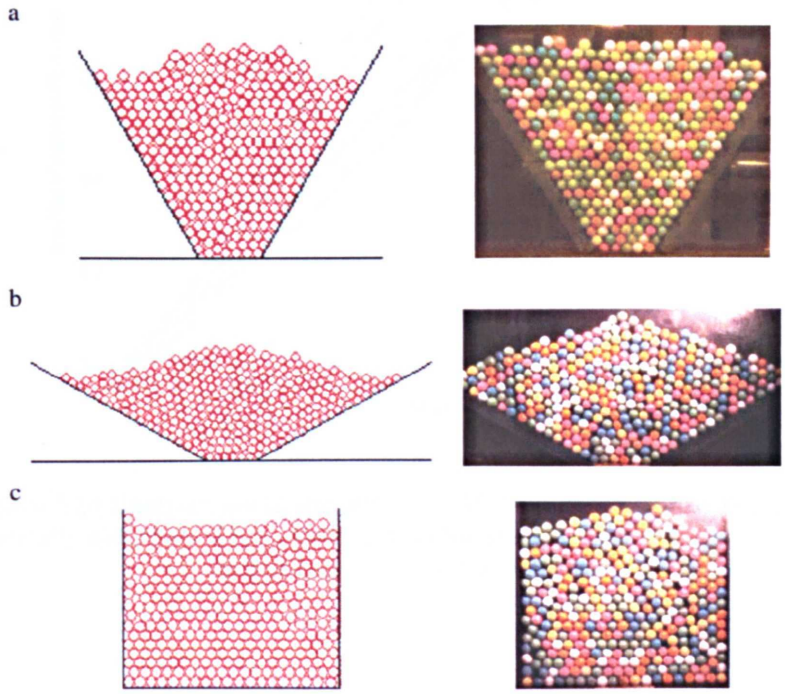

Figure 3.13 Hopper filled with slightly polydisperse spheres, on the left DEM simulation and on the right experiment, for hopper half angle a) 30°, b) 60°, and c) 90° (Mack et al, 2009).

A graphical comparison of the particle discharge rates measured during the experimental studies and predicted by the DEM simulations is shown in figure 3.14. The discharge rates observed in experiments show quite good agreement with those got from the DEM simulation for all three types of hoppers.

There are also quite a few successful examples of using DEM to model granular material flow in mills (Herbst and Potapov, 2004), hoppers (Cleary and Swaley, 2002) and chutes (Zhang et al, 2004). All of these research studies provide evidence that DEM models can replicate granular material flows quite successfully.

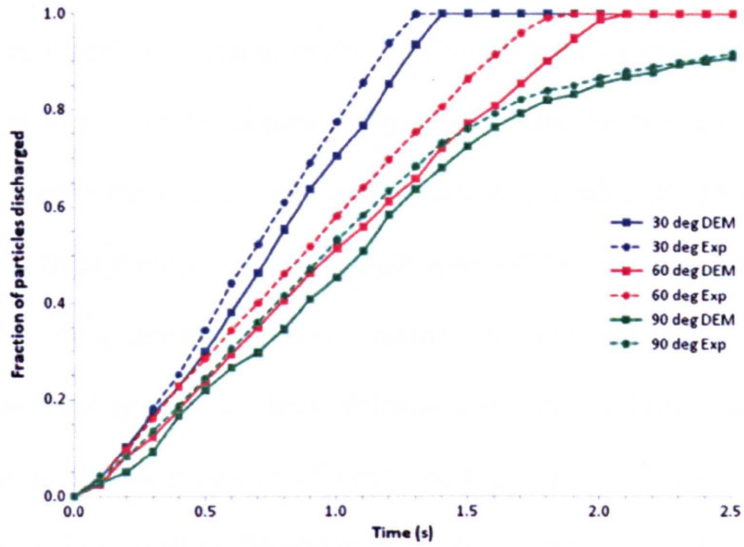

Figure 3.14 Comparison of the predicted DEM simulation and the average experimentally determined time taken for a charge of loaded spheres to discharge an inclined chute (Mack et al, 2009).

3.4 Literature review on rock breakage

3.4.1 Mineral comminution theory

Types of comminution

The mineral rocks extracted from mines and quarries often require to be reduced in size to either liberate a valuable ore or to be shaped and sized to meet a desired specification. Comminution is the process of progressively reducing a mineral until it reaches the size properties required. Once the source ores are removed from their natural beds by mechanical or explosive means, there are two ways to accomplish this size reduction. One is through the compression of the mineral against rigid surfaces, while the other is by impacting the mineral at high speeds against a solid surface (Wills and Napier-Munn, 2006).

Usually, the production of the desired output stream cannot be produced by using just one stage of communition. Rather, minerals normally have to undergo two or more crushing stages to achieve the desired end product. There exists a range of different categories of crusher machines, as practical reduction size ratios that may be achieved normally range from three to six for a single stage (Wills and Napier-Munn, 2006). The types of crushing machine may be classified into two principal forms: primary crushers, secondary/ tertiary crushers. Primary crushers are heavy-duty machines, mainly used to reduce the blast (run of mine) ore down to a size suitable for transport and to feed secondary crushers. Secondary and tertiary crushers are much lighter than the heavy duty and rugged primary crushers. They are used principally to process the products of primary crushers. The different types of crusher machine described in this chapter are listed in table 3.1

Table 3.1 Types of crushers and their application categories (Lindqvist and Evertsson, 2004)

Crusher type	Primary crusher	Secondary/Tertiary Crusher
Jaw	√	x
Gyratory	√	√
Cone	x	√

Principles of mineral comminution

Most minerals are crystalline materials in which the atoms are regularly arranged in a three-dimensional matrix. The configuration of atoms is determined by the size and types of physical and chemical bonds that hold them together. In the crystalline lattice of minerals, these inter-atomic bonds are effective only over small distances and thus may be readily broken if extended by a tensile stress. Such stresses may be generated by tensile or compressive loading (Figure 3.15).

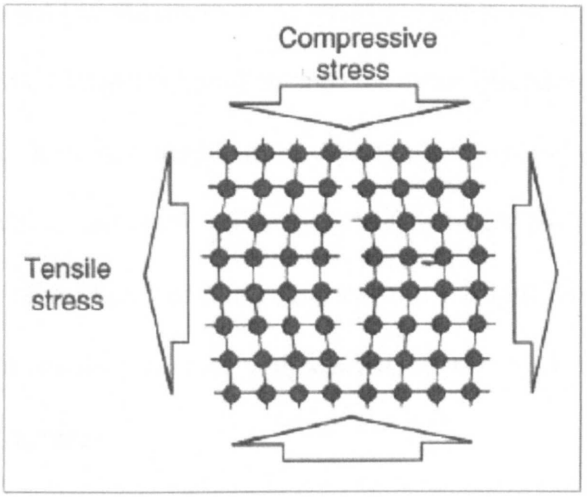

Figure 3.15 Strain of a crystal lattice resulting from the application of tensile or compressive stresses (Wills and Napier-Munn, 2006)

As the rock consists of a variety of minerals dispersed as grains of various sizes, the internal stresses are not evenly distributed even when rocks are uniformly loaded. The distribution of stress depends upon both the mechanical properties of the individual minerals and the presence of cracks or flaws in the matrix (Figure 3.16) (Wills and Napier-Munn, 2006).

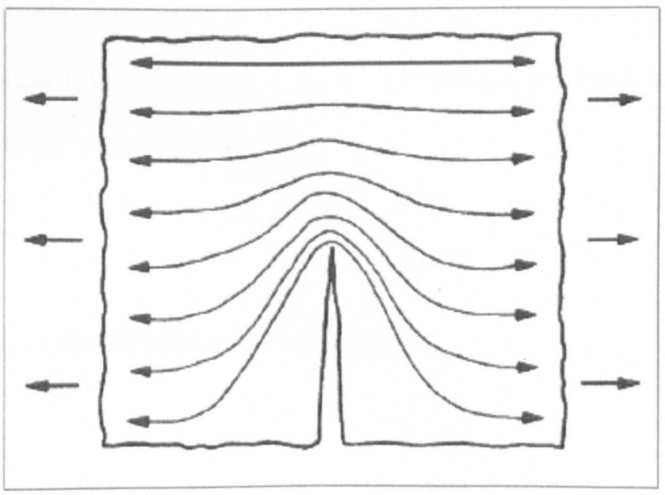

Figure 3.16 Stress concentration at a crack tip (Wills and Napier-Munn, 2006)

Inglis (1913) proposed that the increase in stress at such a site is proportional to the square root of the crack length perpendicular to the stress direction. Therefore, there is a critical value for the crack length at any particular level of stress at which the increased stress level at the crack tip is sufficient to break the atomic bond at that point. The rupture of the bond will increase the crack length, and thus increase the stress concentration, causing a rapid propagation of the crack through the matrix, resulting in brittle fracture.

Comminution Energy

The coalition for Eco-Efficient Comminution (CEEC) (1996) report that the world consumes approximately 4% of the electricity produced to promote comminution, which means intensive energy application, is required for crushing mined material. Therefore, any improvement in improvement in the efficiency in comminution may produce significant cost savings.

The quantity of energy consumed in rock comminution process is related to the feed and product particle sizes. There are a number of theories that have been proposed to evaluate combination energy:

Von Rittinger, (1867):

Constant energy per unit of surface area generated:

$$E = k\left(\frac{1}{x_2} - \frac{1}{x_1}\right)$$ **Equation 3-1**

x_1 = Feed Size x_2=Product Size K=Constant

Kick, (1885):

Constant energy per unit mass for similar relative reduction:

$$E = Kln(\frac{X_1}{X_2})$$ **Equation 3-2**

X_1 = Feed Mass X_2=Product Mass K=Constant

Bond, (1952):

$$E = K(\frac{1}{\sqrt{X_2}} - \frac{1}{\sqrt{X_1}})$$ **Equation 3-3**

X_1 = Feed Size X_2=Product Size K=Constant

Hukki (1961) concluded that the application of no single relationship was adequate to describe the whole comminution process. Figure 3.17 relates energy input expended and particle size achieved in comminution and illustrates over which parameter ranges that the theoretical models described above are relevant.

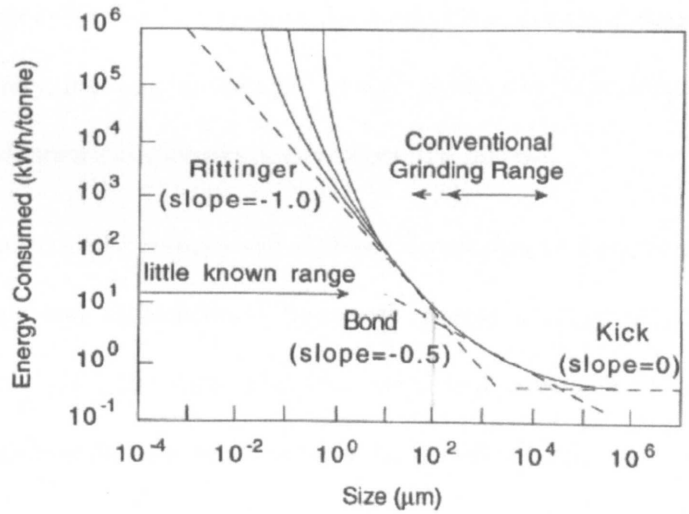

Figure 3.17 A plot of the energy input expended and particle size reduction achieved, as compared against a number of proposed theoretical models.(Hukki, 1961)

It can be seen that the application of Kick's law was more appropriate across primary crushing sizes, Bond's law produces a good fit for rod and ball mill particle treatment

sizes and Von Vittinger's model more applicable to finer grinding processes (Napier-Munn et all, 1996). However, this further confirms that none of the proposed models is entirely satisfactory across the whole comminution product size range. The greatest problem lies in the fact that most of the input energy to a crushing machine is absorbed by the machine itself, whilst only 30-40% (CEEC,2012) of the total energy is available for the processed material breakage.

3.4.2 Tensile strength of rock

It is widely accepted that the failure of a spherical particle under compression is a tensile failure (McDowell & Bolton, 1998). There is a tensile stress distribution induced in the particle and that according to Griffith criterion (Griffith, 1920) failure occurs when the tensile stress, σ,at a critical flaw of a given size, α, when the stress intensity factor $K = Y\sigma\sqrt{\alpha\pi}$ (where Y is a dimensionless number relating to the problem geometry) for the flaw reaches the mode *I* fracture toughness of the material K_{Ic},. Consequently, the 'tensile strength' of rock grains can be indirectly estimated by measuring the diametrical compression between flat platens.

Lee (1992) diametrically compressed individual particles of Leighton Buzzard sand, oolitic limestone and carboniferous limestone, across a range of particle sizes, as shown in figure 3.18. The same particles were then subjected to Brazilian tensile strength to determine the tensile strength of the particles computed from the equation (Jaeger, 1967):

$$\sigma_f = \frac{F_f}{d^2} \qquad \textbf{Equation 3-4}$$

where σ_f is the tensile stress at failure, F_f is the diametrical fracture force applied and d is the average particle size calculated by averaging the smallest and largest dimensions of each particle. McDowell and Bolton (1998) define a general characteristic stress σ as:

$$\sigma = \frac{F}{d^2} \qquad \textbf{Equation 3-5}$$

Where F is the force applied and d is the particle size. Figure 3.19 illustrates a typical result of this type of crushing test of the nominal applied force is plotted against the measured deformation (Lee, 1992). An examination of this plot concludes that there are some initial peaks, which correspond to the bearing failures at contact points, before the maximum peak load is achieved. The bearing failures correspond to the fracture of particle asperities and a rounding of the particle as small surface irregularities break off. The maximum peak load corresponds to the generation of two or more major pieces. Thus, the tensile strength of particle is calculated from this measured maximum load.

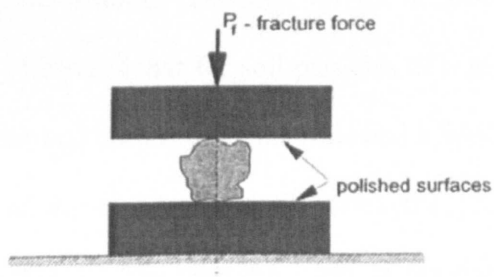

Figure 3.18 Particle tensile strength measurement apparatus (Lee, 1992)

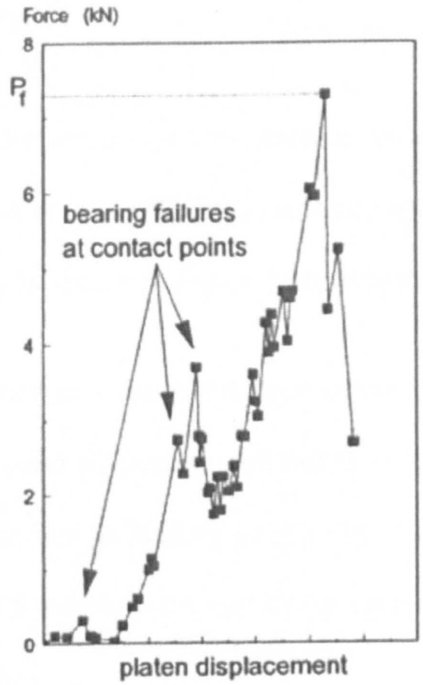

Figure 3.19 Typical load-deflection plot for a typical particle tensile strength test(Lee,1992)

Variability in tensile strength

Weibull (1951) statistical distribution theory may be used to describe the variations measured in the strength of ceramics (Davidge, 1979). McDowell & Amon (2000) and Nakata et al (1999) confirmed that for soil particles of a given size distribution, the distribution of the measured tensile strengths followed a Weibull distribution. Lim et al (2004) showed that the measured tensile strengths of railway ballast also followed a Weibull distribution. The simplest form of Weibull (1951) statistics is based on a 'weakest link' model. This model proposes that if one element in a larger sample of interconnected identical elements fails, then the whole sample will fail. The survival probability $P_s(V_o)$ for an element of volume V_o to survive under a tensile stress σ is given by the following relationship:

$$P_s(V_o) = \exp(-(\frac{\sigma}{\sigma_o})^m)$$ **Equation 3-6**

The stress σ_o is the value of stress for specimens of volume V_o such that 37% of tested specimens survive, and m is the Weibull modulus, which decreases with increasing variability in strength, as shown in Figure 3.20. When $\sigma = 0$, all the samples survive and $P_s(V_o) = 1$. As σ increases, more and more samples fail and $P_s(V_o)$ decreases. For large stresses, $\sigma \to \infty$, and all samples will fail as $P_s(V_o) \to 0$. For a larger sample of volume $V=nV_o$, the survival probability of that sample would be $\{P_s(V_o)\}^n$. Thus the survival probability of a volume V is given by the expression:

$$P_S(V) = \left[exp\left[-\left(\frac{\sigma}{\sigma_o}\right)^m\right]\right]^{\frac{V}{V_o}}$$

$$= exp\left[-\frac{V}{V_o}\left(\frac{\sigma}{\sigma_o}\right)^m\right]$$ **Equation 3-7**

$$= exp\left[-\left(\frac{\sigma}{\sigma_{ov}}\right)^m\right]$$

where σ_{ov} is the stress for specimens of volume V such that 37% of tested specimens survive. It can be seen that σ_{ov} is a strong function of volume V, and is given by the equation:

$$\sigma_{OV} \propto V^{-1/m}$$ **Equation 3-8**

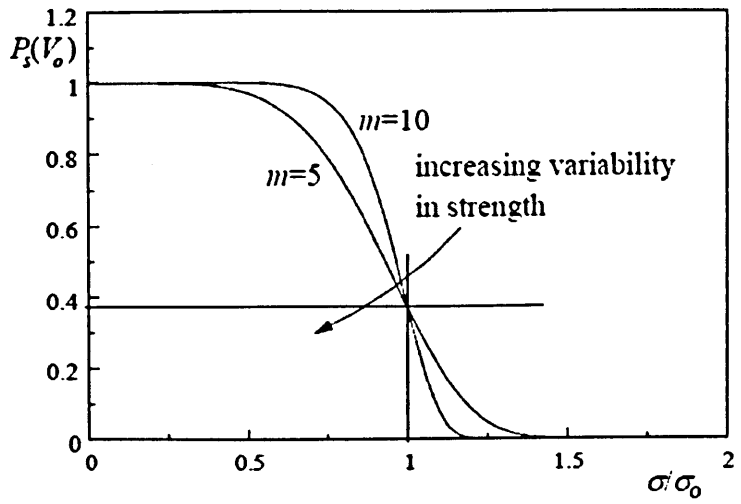

Figure 3.20 A plot of a Weibull distribution of strengths (McDowell, 2002)

Size effect on rock strength

Lee (1992) found that the average tensile strength of a collection of particles to be a function of the particle size *d*. Figure 3.21 shows the mean tensile strength σ_{av} as a function of the average particle size *d*. From an analysis of this data, he concluded that the average tensile strength to the particle size was given by the following relationship:

$$\sigma_{av} \propto d^b$$ **Equation 3-9**

where typical values for the parameter, *b* are -0.357, -0.343 and -0.420 for Leighton Buzzard sand, oolitic limestone and carboniferous limestone, respectively. The size effect on particle strength was also evident in an analysis of the results of the particle crushing tests performed by Billam (1972).

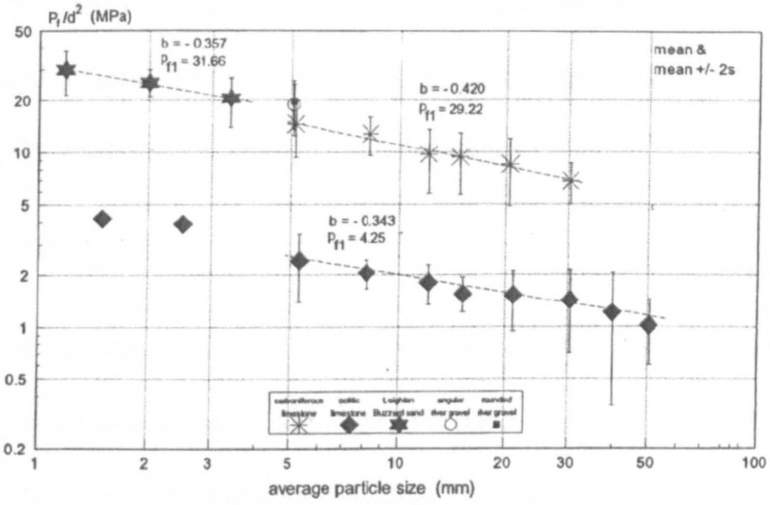

Figure 3.21 Mean tensile strength as a function of particle size (Lee, 1992)

McDowell and Bolton (1998) were able to describe the experimental results obtained by Lee (1992) and Billam (1972) using Weibull statistics. They assumed that the loading geometries of the particles are similar and the distribution of strengths of each of the grain sizes tested followed a Weibull distribution. Thus Equation 3-9 can be recast in the form:

$$\sigma_o \propto d^{-3/m}$$

Equation 3-10

where σ_o is the value of stress for specimens of volume V_o such that 37% of tested specimens survive, and m is the Weibull modulus. It was further confirmed that his equation represents Lee's data for rock grains shown in figure 3.21 when the parameter m takes a value in the range from 5-10.

Following McDowell and Bolton (1998)'s proposition, McDowell and Amon (2000) compressed a wide range of particle sizes of Quiou sand following the experimental method of Lee (1992) (Figure 3.16). A summary of their results are shown in Table 3.2. Although the observed variation in the Weibull modulus across the range of particle sizes is large, the average Weibull modulus determined is approximately

equal to 1.5. They deduced that for a Weibull distribution of strengths, the 37% tensile strength is proportional to the mean tensile strength. They finally describe the relationship between particle strengths and particles sizes as:

$$\sigma_{o,d} \propto \sigma_{av} \propto d^{-3/m}$$ **Equation 3-11**

where $\sigma_{o,d}$ is the stress for particles of size d such that 37% of tested particles survive, σ_{av} is the average stress at failure, d is the particle size at failure and m is the Weibull modulus. It is noted that b in equation 3-9 is equivalent to -3/m here.

Table 3.2 Weilbull modulus and 37% strength for a wide range of particle sizes of Calcareous Quiou sand (McDowell & Amon, 2000))

Nominal size /mm	Average size at failure/mm	Weibull modulus m	37% tensile strength /Mpa
1	0.83	1.32	109.3
2	1.72	1.51	41.4
4	3.87	1.16	4.2
8	7.86	1.65	0.73
16	15.51	1.93	0.61

In Figure 3.22 the 37% tensile strength is plotted as a function of average particle size at failure (McDowell, and Amon, 2000). The data may be described by the following expression:

$$\sigma_{o,d} \propto d^{-1.96}$$ **Equation 3-12**

This equation corresponds to a parameter value m=1.5. Therefore, McDowell & Amon (2000) concluded that the Weibull modulus could be applied to describe the size effect on particle strengths of Quiou sand, gravel and cobble-sized particles if the loading geometries of all the particles are similar.

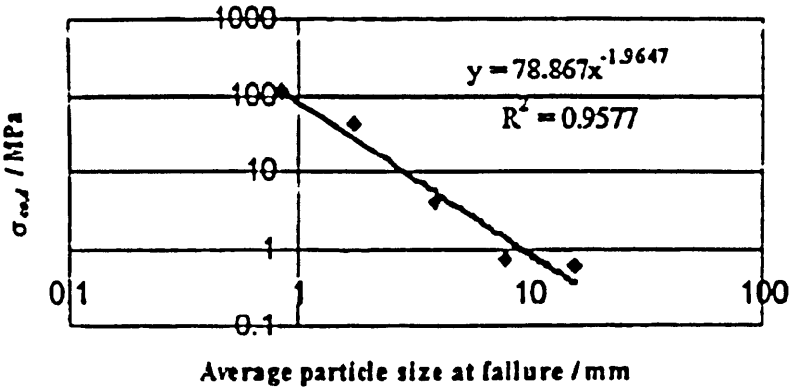

Figure 3.22 37% strength as a function of average particle size at failure (McDowell &Amon, 2000)

3.4.3 Rock breakage modes

There are two commonly used approaches to simulate the size reduction of rock during breakage using DEM:

- Replacing the resultant 'breakage' particles with a number of new and smaller fragments. This is called as population balance model (PBM) proposed by Herbst et al (2003).
- The particle is modelled by an assembly of bonded micro-spheres and the breakage is modelled by the breakage of some of these bonds. This model is often called the bonded particle model (BPM) proposed by Potyondy & Cundall (2004).

PBM

This approach initially invokes a probability of breakage for each size i (or size class i) in the population, p_i, and a distribution of progeny fragments, b_{ij}, from the breakage of size j particles into size i. This process of breakage and redistribution is shown conceptually in figure 3.23.

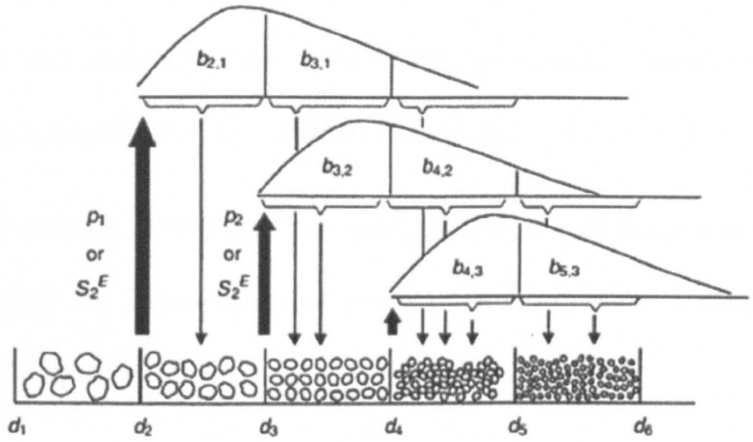

Figure 3.23 Conceptual view of population balance accounting method (Herbst et al, 2003))

This conceptual process may be mathematically written for each size fraction i (d_i to d_{i+1} for $i=1$ to n) as:

$$m_{P,i} = m_{F,i} - p_i m_{F,i} + \sum_{j=1}^{i} b_{ij} p_j m_{F,j}$$

Equation 3-13 (Herbst, 2003)

In compact matrix notation form, as the product size distribution vector (a column vector of length n), m_p may be computed from the feed size vector by a linear transformation involving the set of breakage probabilities and distributions of fragments as following expression:

$$m_P = [I - (I - B)P]m_F$$

Equation 3-14 (Herbst, 2003)

where I is the unitary matrix, P is the selection function (diagonal consisting of elements p_i to p_n) used and B is the breakage function (a lower triangular matrix consisting of a column b_{ij} ($i=j$ to n) for each parent size j).

The most important issue in the application of the PBM to replicate rock breakage is the choice of the selection and breakage modes. The selection function determines

which particles should be broken and the breakage function determines the size distribution and positions of the broken. Various selection functions and breakage modes have been employed by previous researchers.

Astrom & Herrmann (1998) used this approach and showed that it was possible to use DEM to model the fragmentation of grains in two dimensions. They provided two types of breakage criteria:

(1) A threshold value for the pressure on a grain

(2) A threshold value for the largest compressive force at the contacts of a grain.

For the size distribution of fragments, they also investigated two different criteria, and found that the two mechanisms produced essentially the same final particle size distributions.

(1) Simply split in two equal-size fragments. The use of this fragment distribution function can avoid the appearance of huge number of particles in DEM simulation. However, it can induce large and unrealisable local pressures.
(2) Twelve fragments of three different sizes are placed into the area of the broken grain and the rest of the mass is placed just outside in the 'pockets' between the surrounding grains. This criterion decreased the predicted local pressure of new fragments but increased the number of particles.

Lobo-Guerrero & Vallejo (2005) developed a similar two-dimensional model to represent granular crushing. Their breakage probability and redistribution criteria are shown on figure 3.24. A particle under multiple contacts WAS assumed to be equivalent to that obtained under a diametrical compression test and to act in the direction of largest contact force acting on the particle. They used the induced tensile

stress as the governing breakage criterion. In their model, the tensile stress was approximated by the expression presented in Figure 3.24(b), where P_1 is the value of the highest contact force acting on particle, L is the thickness of the particle, and D is the diameter of the particle. In terms of the particle redistribution matrix, the particle was split into a group of eight particles of three different sizes based on their physical experiments as figure 3.24(c) shows. However, this method cannot conserve the mass.

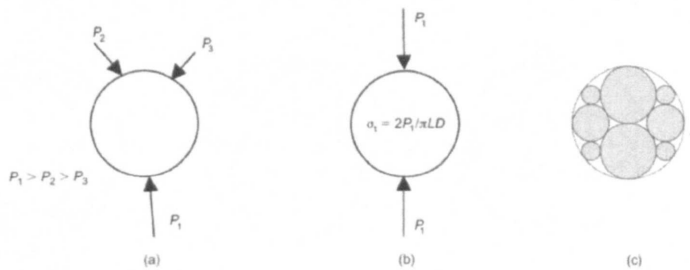

Figure 3.24 Idealisation of the induced tensile stress, and arrangement of the produced fragments (Lobo-Guerrero & Vallejo,2005)

McDowell and De Bono (2013) used a PBM method in their one dimensional normal compression simulation in three dimensions. The Octahedral shear stress induced within each sphere was for the first time used to determine whether fracture should occur. The criterion set was if a particle is subjected to diametrical point loads, equal in three mutually orthogonal directions, then it would not break under this hydrostatic stress ($q=0$). The octahedral stress in a particle is derived from principal stress, and is given by:

$$q = \frac{1}{3}[(\sigma_1 - \sigma_2)^2 + (\sigma_1 - \sigma_3)^2 + (\sigma_3 - \sigma_2)^2]^{1/2} \qquad \textbf{Equation 3-15}$$

Figure 3.25 shows three different particle size redistribution mechanisms used in their research. This mechanism not only conserves mass but also ensures that the progeny

fragments locate inside the boundary of the original particle. The drawback is that the generation of a large undesirable local pressure caused by the overlap of the fragments. In order to dissipate this artificially induced energy, particle breakages are updated (for the whole sample) after a number of computational cycles equivalent to 0.003s (the actual number of cycles during this time interval is inversely proportional to the time step).

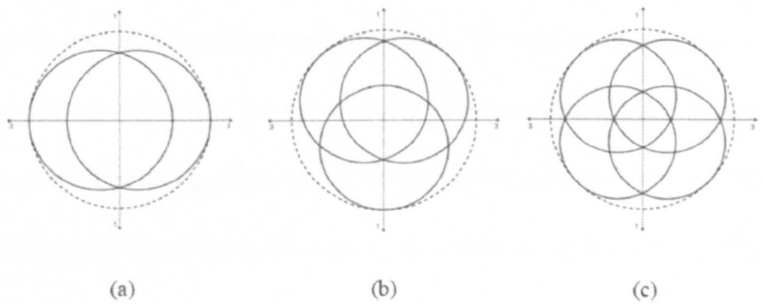

Figure 3.25: Various splitting mechanisms: (a) Equal diametrical splitting; (b) Splitting into three particles; (c) Splitting into four particles.

BPM

Another approach to model rock breakage using DEM is the application of the bonded particle model (BPM). In this model, the rock is represented by an agglomerate which is a dense packing of micro-spherical particles bonded at their contact points. Rock damage is represented as bonds breakage which form and coalesce into macroscopic fractures when a load is applied. In this approach, the packing method of the micro-spheres of the agglomerate is important because it directly determines the fabric structure of the agglomerate.

Agglomerates were intended to represent soil grains initially. Robertson (2000) used contact bonds to bond regularly packed balls of identical size in order to form

approximately spherical agglomerates. Robertson (2000) initially examined three types of regular packing: face centred cubic (FCC), body centred cubic (BCC) and hexagonal close packed (HCP). It was found that the results for HCP were the most consistent and adopted this packing for his simulations. Figure 3.26 shows an individual HCP agglomerate of 527 balls compressed diametrically between two platens (Robertson, 2000). The agglomerate was randomly rotated before the load was applied. A typical result for this test is presented in Figure 3.27, which shows a force-strain curve, and the fractured agglomerate. The agglomerate appears to have a well-defined peak strength due to the sudden failure of the agglomerate However, it is observed that there is an initial gap before the force begins to rise steadily. Robertson (2000) explained this delay as due to an unstable rotation of the particle. McDowell & Harireche (2002a) showed that by allowing the agglomerate to stabilize under the application of gravity, the force will increase from the beginning of the test because the agglomerate is in a stable position when load is applied. The use of frictionless walls in the tests by Robertson (2000) means that slip was allowed to occur at the ball to wall contact at all times. If the walls had been assigned a coefficient of friction, the force should increase slowly or erratically at the early stage of the test and rise rapidly prior to failure. Of course, in this case the failure mechanism and the peak strength obtained would both be different. Nevertheless, stabilizing the agglomerate under gravity is considered to be a more realistic approach. HCP agglomerates have already successfully been used to model the Weibull (1951) distribution of particle strengths.

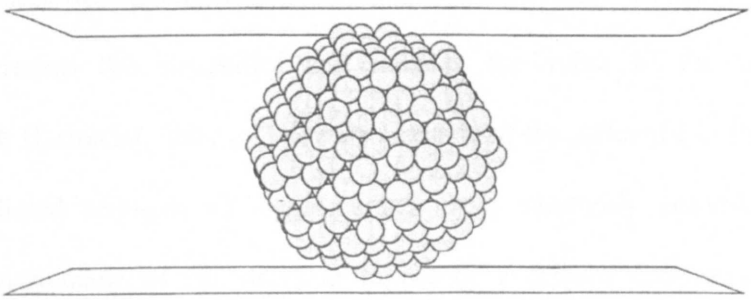

Figure 3.26: Crushing test on agglomerate (Robertson, 2000).

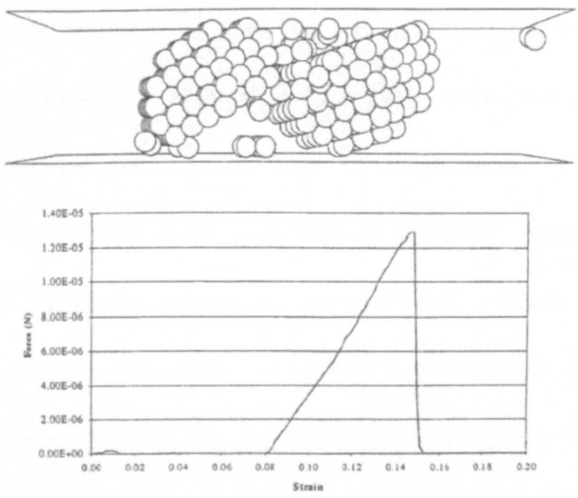

Figure 3.27 Typical result of a crushing test on an agglomerate (Robertson, 2000).

Robertson (2000) showed that it is possible to produce a Weibull (1951) distribution of soil particle strengths by randomly removing some of regularity in the HCP agglomerate. Three types of flaws were introduced by Robertson (2000): removing bonds, reducing some bond strengths and removing balls. He found the Weibull distribution of strengths was best reproduced by randomly removing balls in the agglomerate and the Weibull modulus depended on the range of the number of balls removed. McDowell & Harireche (2002a) also got a Weibull modulus of $m \approx 3$ as the result of the execution of more than 30 tests by randomly removing 0-25% of the

balls in the agglomerates. It was also found that increasing the range of the balls removed increases the variability and reduces the value of the parameter m (McDowell & Harireche, 2002a). They also examined the influence of the size effect on the predicted strength of agglomerates with randomly removed balls. A comparison was made of the stress at failure of a 0.5mm diameter agglomerate comprising initially 135 balls with removing 0-25% and a 1mm diameter agglomerate comprising initially 1477 balls with removing 0-25% balls. It was concluded that the stress at failure of the 1mm diameter agglomerate was higher than that of the 0.5 diameter agglomerate, which conflicts with the actual observed size effect on soil particle strength discussed in section 3.4.2. This discrepancy was explained by McDowell & Harireche (2002a) as due to differences in geometry between agglomerate sizes caused by HCP and random rotation. McDowell & Harireche (2002a) introduced further randomness, achieved by initially removing a certain percentage of balls in the agglomerate, to attempt to produce the correct size effect on average strength. Figure 3.28 shows the Weibull distribution of strength tests for a crushing of the 0.5mm and 1mm diameter agglomerates which gives a correct size effect. In these tests, 30% of the balls were initially removed at random before a further random 0-25%.

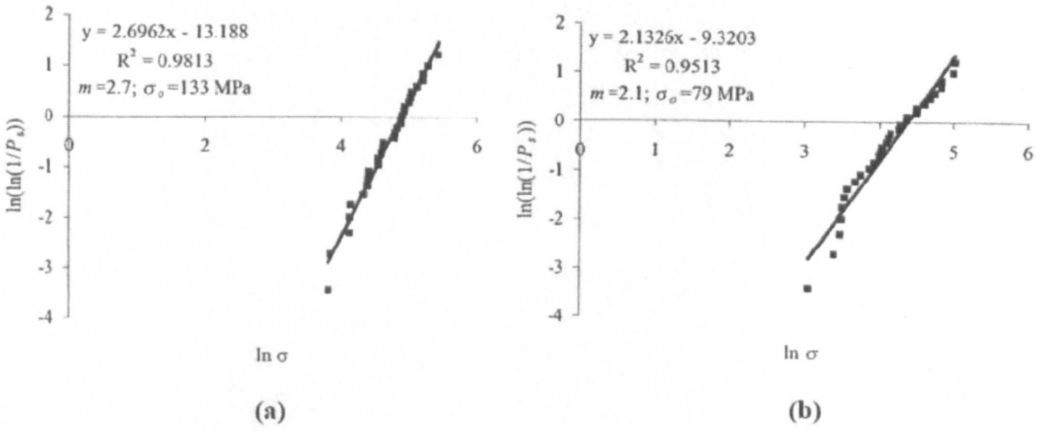

Figure 3.28. Weibull probability plot for (a) 0.5mm (b)1mm agglomerates (McDowell & Harireche, 2002a)

Another popular method is the radius expansion method which was introduced by Lubachevsky & Stillinger (1999) and later modified by Potyondy & Cundall (2004). This type of agglomerate is generated by a four step process. Figure 3.29 shows the procedure for a two dimensional model.

- Particles with radii chosen randomly from a uniform size distribution are randomly generated within a volume bound by planar, frictionless walls.
- The system is allowed to adjust by particle movement under zero friction.
- The radii of all spheres are then increased simultaneously until the system reaches a prescribed confining pressure.
- The radii of 'floating' spheres that have less than three contacts, are iteratively increased to achieve at least four contacts.

This method has also recently been used by Potyondy (2007), Tavarez & Plesha (2007) and Cil & Alshibli (2012).

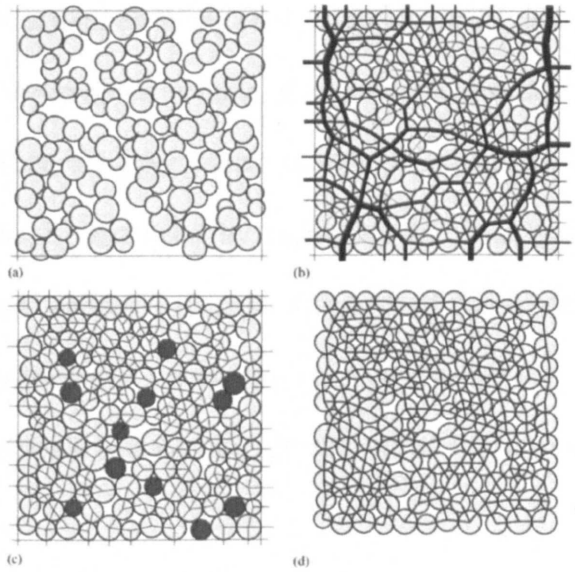

Figure 3.29 (a) particle assembly after initial generation but before rearrangement; (b) contact-force distribution (All forces are compressive, thickness proportional to force magnitude.) after step 2; (c) floating particles (with less than three contacts) and contacts after step 4; (d) Bonds added after step 4. (Potyondy & Cundall , 2004)

The advantage of HCP packing is that it can theoretically provide the densest packing (a porosity of 0.26) of uniformly-sized bonded spheres to simulate a solid particle. This density is achieved without requiring any particle overlap, which would result in locked-in forces. However, the use of HCP provides a regular and anisotropic packing. In contrast, the radius expansion method provides a random packing agglomerate, but one which is not as dense as an HCP agglomerate

3.4.4 Modelling Complex Particle Shape

The basic modelling entity used within the PFC^{3D} code is a sphere, whilst most naturally occurring granular materials including rocks can exhibit an irregular shape. Therefore it is necessary to produce improved models to more accurately replicate the shape of complex particles to obtain quantitatively reliable simulation results using the BPM approach to model particles.

Clustering method was used by Wang et al. (2007) to model pavement materials, This method firstly fills the irregular volume of a real particle with a regular arrangement of small spheres. Then a bigger sphere is selected to replace a group of adjacent spheres. The process is illustrated by figure 3.30(a). The main drawback of this method is the 'bumpy' surface The major drawback of this model is that it can create rough or bumpy surfaces that are not representative of the real surface as shown in figure 3.30b. This rough surface may greatly affect the resistance of the particle within a flow model.

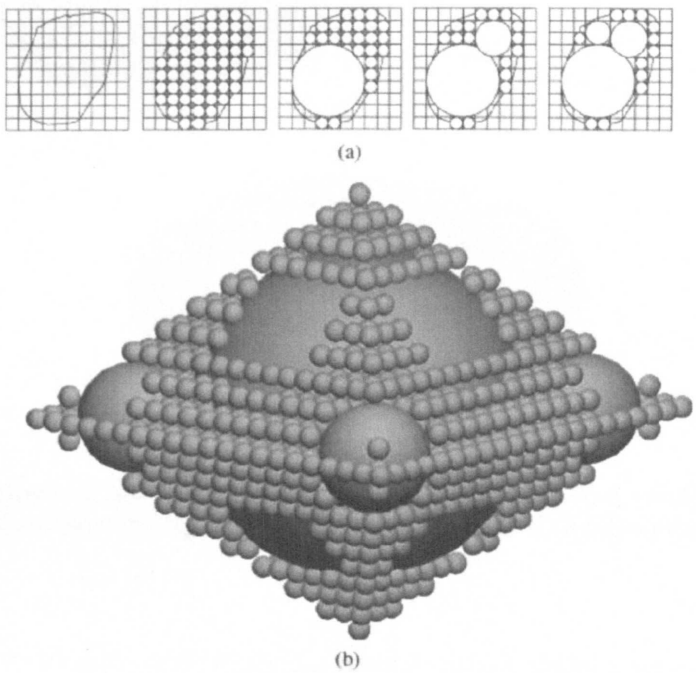

Figure 3.30 Clustering method: (a) method on a two-dimensional irregular shape (b) rough surface on the cluster (Wang, et al. 2007)

Price et al. (2007) propose an sphere fitting method to create the complex particle shape. The method is based upon the principle that one unique sphere can fit four points in space. Firstly, they repeatedly create spheres by choosing four random points on the boundary of the particle until they approximately fill the volume occupied by the real particle, as shown in figure 3.31(a). This initial estimate is subsequently

refined by locally optimising the position of the spheres in relation to the real particle surface. To achieve this, it is necessary to associate all the points on the surface with the closest sphere (Figure 3.31b). The last step is to minimise the distance between each sphere and its group of associated points. It is achieved by slightly moving and/or expanding the sphere (figure 3.31c). This restriction and the optimisation method make the whole process very expensive in terms of calculation time.

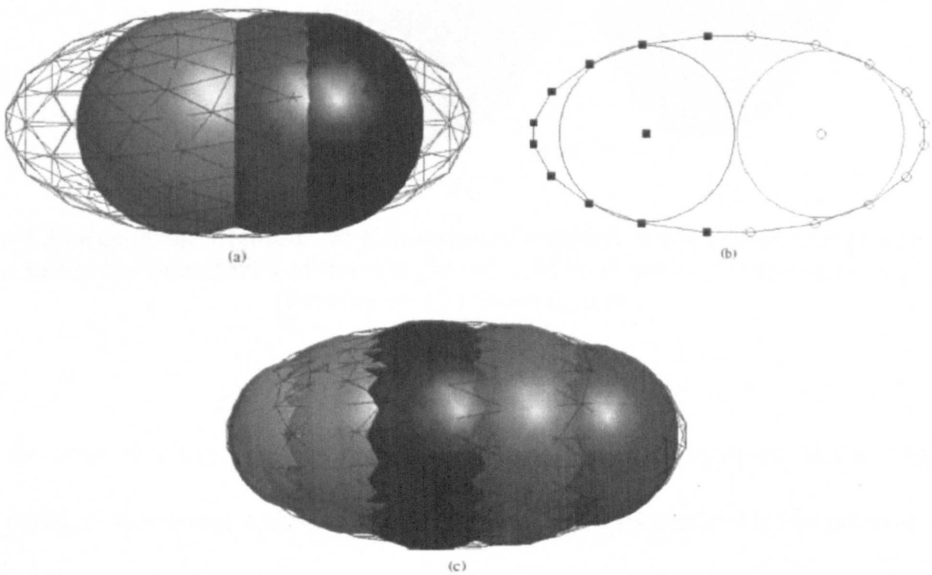

Figure 3.31 Sphere fit method. (a) Fitting of a sphere through four random points on the real particle surface. (b) Sphere and associated points. (c) Final optimised spheres. (Price et al, 2007)

Ferellec and McDowell (2008) propose another novel, simpler and computationally faster method to create complex shapes by assembling spheres together. This method also fills the volume occupied by the real particle with multiply sized spheres. Firstly, the method selects random a point on the surface of the real particle (a 'node'), growing internally a tangent sphere along its normal direction until any point of the sphere contact another node on the boundary of real particle (Figure 3.32a). This process is then repeated for all the nodes on the boundary. The nodes which are quite

close to a created sphere (black circles on figure 3.32a) can be ignored at this step. Indeed, the contribution of a new sphere at a point very close to an existing one would be negligible. Figure 3.32b is a picture of real ballast while figure 3.32c is the simulated model particle.

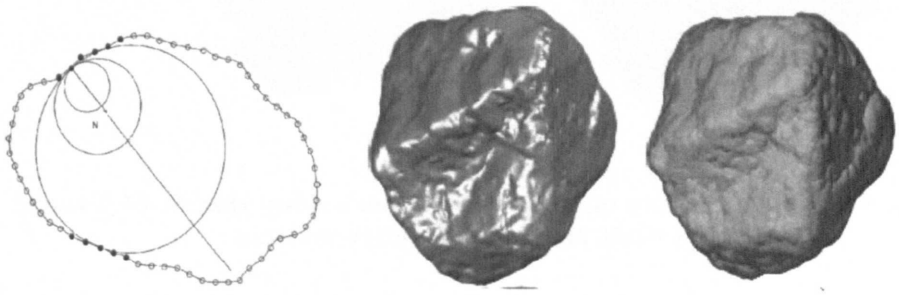

(a) (b) (c)

Figure 3.32 Expansion Method: (a) Expansion of a sphere along the normal at a surface point inside the boundaries of the real particle. (b) Real ballast (c) Simulated ballast (Ferellec and McDowell, 2008)

It can be seen that this method generates a good visual replication of the irregular shape particle. However, a significant disadvantage of this method is the generation of overlapping mass which may result in a non-uniform density. This will lead to incorrect moments of inertia and therefore to rotational resistance. To overcome this problem, Ferellec and McDowell (2010) proposed that the mass of every ball to be the same, thus that the density of each ball is inversely proportional to volume. This improved method seems to work well. Figure 3.33 shows a visual comparison of the modelled density distributions with and without the inclusion of the mass correction.

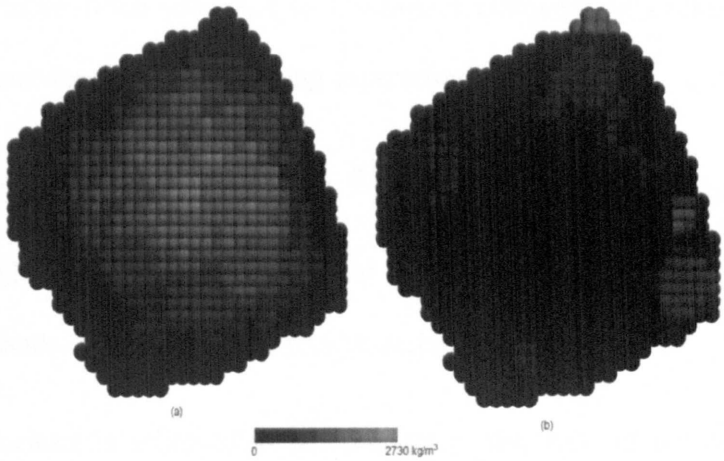

Figure 3.33 Density inside a modelled particle: (a) without mass correction (b) with mass correction (Ferellec and McDowell,2010)

3.5 Modelling of the performance of cone crushers

Since people realized the possibility to simulate and predict cone crusher performance is of great interest for the development of crushers as well as for the design and optimization of crushing plants, they began to research the modelling of rock flow and breakage in a cone crusher. However, most of the previous research studies on cone crusher performance reported in the literature have focussed on the development of mathematical and experimental inverse solution models. Few studies have been published that have employed DEM to investigate crusher performance.

3.5.1 Gauldie's Model

Some of the earliest published research studies to model the performance of cone crusher were conducted by Gauldie (1953, 1954). He published two papers in which he presented a mathematical method to predict the flow of rock material through jaw and cone crushers. In his model, the crusher chamber is divided into several crusher chamber flow zones, each of which correspond to how a volume of material moves

through the crusher when subjected to a series of compression strokes. Mass flow continuity is considered by the following expression:

$$m_i = 2\pi r_i A_i \rho_i = constant\ (i = 1,2,3 \ldots . n)$$ **Equation 3-16**

In expression (2.1), i denotes the number of the zones, r stands for the radius of the zones [m], ρ stands for the density of rock material [kg/m^3].

The total throughput is achieved as the product of the mass of the material in an arbitrary zone multiplied by the eccentric speed of the main shaft.

$$Q_i = m_i$$ **Equation 3-17**

Crusher manufacturers use the Gauldie model either in its original or a modified form. However, there can be severe restrictions on the applicability of the Gauldie model imposed by the assumptions behind the construction of the model. These assumptions are:

1. A material volume slides down the mantle until it is nipped between the mantle and concave.

2. The material is assumed to be porous and behave plastically.

3. The material is assumed to be non-sticky with a coefficient of friction describing the interaction between machine parts and rock.

It is widely accepted that Gauldie's model can only provide a very rough first estimate to the total throughput. It cannot tell either what happened in the chamber such as whether or not the crusher is choke-fed. The principal contribution of the Gauldie model is its definition of the division of the crusher chamber into a number of zones.

This provided a useful model construction which was adopted and developed by future researchers.

3.5.2 Whiten's Model

Whiten (1972) proposed a simple model for the operation of a cone crusher which assumes that particles can either be broken or dropped through the crusher unbroken as the particle feed flows through the crusher chamber. The broken particles then have the same chance of dropping through the crusher or of being broken further. Thus, the cone crusher is simplified into a single breakage zone and a probability of entering or re-entering this breakage zone. Figure 3.34 shows symbolically the parts of this cone crusher model and the internal flows between them.

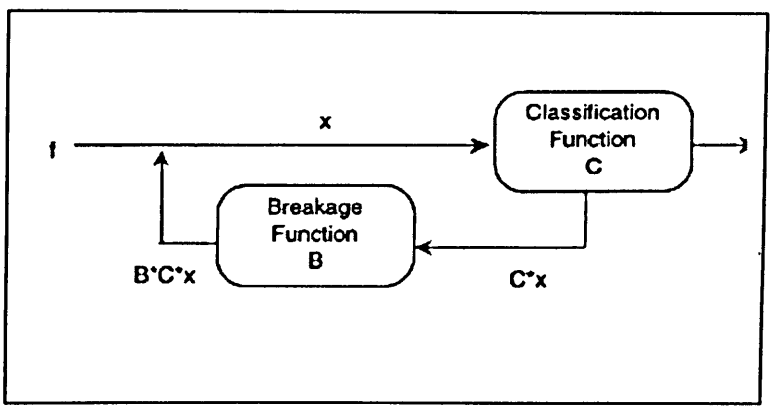

Figure 3.34 Symbolic representation of crusher model (Whiten, 1972)

Whiten (1972) also derived the following two expressions based on the mass balance at the nodes in Figure 3.34:

$$f + BCX = X$$ **Equation 3-18**

And

$$X = CX + P$$

Equation 3-19

Where x is the vector representing the amount in each size fraction entering the crusher, f means the feed size distribution vector, P stands for the product size distribution vector. C is the classification function, a diagonal matrix describing the proportion of particles in each size interval selected to enter the crushing zone. B stands for the breakage distribution function, a lower triangular matrix giving the relative distribution of each size fraction after breakage.

Combining the above equations:

$$P = (I - C) * (I - BC)^{-1} * f \quad \text{(i=Unit matrix)}$$

Equation 3-20

In this model, the selection of particles for breakage in the crusher chamber is dependent on particle size, with the chance of selection for breakage increasing to one for all particles greater than the open size setting (OSS) of the crusher. The classification function C is expressed as:

$$C(s) = 0 \qquad s < k_1$$

Equation 3-21

$$C(s) = 1 - \left(\frac{s - k_2}{k_1 - k_2}\right)^2 \qquad \text{k1} < s < k2$$

Equation 3-22

$$(s) = 1 \qquad s > k_2$$

Equation 3-23

K_1 stands for CSS, K_2 stands for OSS.

Using Whiten's model, the throughput and the size of product may be determined. However, a mean error of 0.5 and a standard deviation of about 3.0 are the typical differences obtained between the predicted model and the observed percentage sizings.

Based on the Whiten model, Napier-Munn et al (1996) proposed a modified cone crusher model which considers the crushing process of cone crusher as a flow sheet that describes a simple repetitive cycle of events. As illustrated in Figure 3.35, new feed material entering the crusher is first 'classified'. Very fine material by-passes breakage and reports directly to product whilst the coarse material reports directly to breakage. Intermediate-sized material reports to breakage with a probability which increases with size. After breakage the classification process is repeated, fines reporting to product and material which is still too coarse reporting to breakage, and so on.

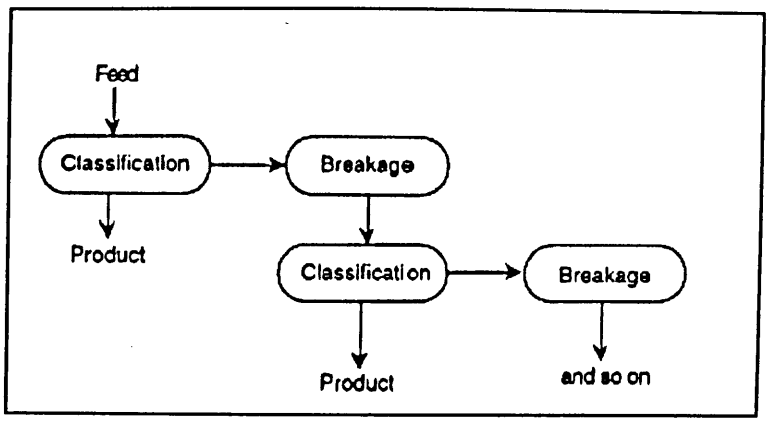

Figure 3.35 Concept of classification and breakage (Napier-Munn et all, 1996)

3.5.3 Evertsson's Model

Based upon the models and results reported in previous research studies Evertsson published three papers (1997, 1998, 1999) in which he presented the staged development of a more comprehensive and accurate mathematical cone crusher model.

In the first paper of the series, Evertsson and Bearman (1997) proposed a rock size reduction theory which is an extension to the Whiten model. The modified Evertsson model defines the crushing process as characterized by three process elements:

- Selection S: the probability of a particle being broken
- Breakage B: the actual size reduction resulting in smaller particles
- Classification C: size separation process occurring between subsequent reduction cycles.

Figure 3.36 shows a flow sheet diagram of the three stages of a single reduction cycle stages.

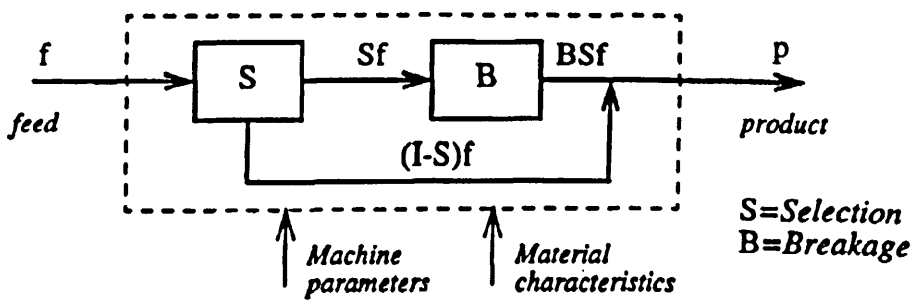

Figure 3.36 Flow sheet model of a single reduction cycle (Evertsson and Bearman, 1997)

This model implicitly assumes that no internal particle size classification occurs within a crusher chamber which is a reasonable assumption for a choke-fed crusher. During a compression stroke of the cone some particles are selected for breakage depending on how and to what level they are stressed. When a particle breaks the sizes of the daughter fragments are controlled by the specific breakage appearance of the material. The particles that have not reached a critical stress level will be left unbroken. However, these particles can also contribute to the generation of fines due to attrition at the contact points.

It can also be clearly seen that the model processes defined by figures 3.36 and 3.34 are almost identical. However, the Whitten model simplifies the operation of the crusher to a single crushing zone and the model parameters fitted to full-scale experimental data. Evertsson adapted the work of Gauldie (1953) to propose a sequential application of the single reduction cycle model to the crushed material as it gradually descends through a series of flow zones defined within the crusher chamber. Figure 3.37 shows a schematic representation of this integrated model.

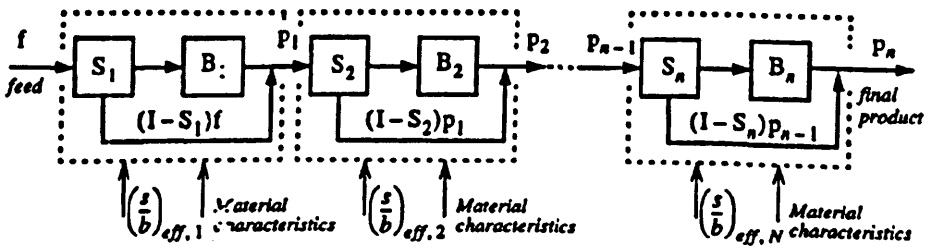

Figure 3.37 Schematic representation of an integrated model of a cone crusher comprising of N sequential crushing events (Evertsson and Bearman, 1997)

The size reduction process in Figure 3.37 can be mathematically described by the following equation:

$$P = \left[\prod_{i=1}^{N}[B_i S_i + (1 - S_i)]\right] f \qquad \text{Equation 3-24}$$

Where P and f represent the product and feed mass flow rates. B_i and S_i are operators corresponding to the breakage and selection events, respectively. N is the total number of crushing events that occur within the modelled crusher.

As the chamber is divided into several zones, there should be different classification functions and breakage functions in terms of different zones. To include the selection and breakage modes, Evertsson (1997) proposed the specification of two new

parameters: the effective bed height, $b_{eff,}$ and the effective stroke, s_{eff}. The selection and breakage functions were determined from the execution of experiments performed using the test cell shown on figure 3.38.

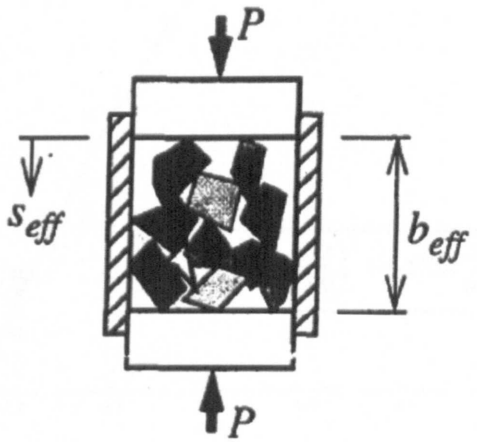

Figure 3.38 The principle of the test equipment with characteristic parameters. (Evertsson and Bearman, 1997)

The test cell was designed to simulate the conditions experienced by a volume of material within a real crushing chamber. The laboratory test corresponds to the part of the machine cycle process, where the cone and mantle liners move towards each other. The material is then locked between the chamber walls where it may only deform elastically and/or break into smaller particles.

Through the results of his test, the classification and breakage function is found to be related to effective compression ratio $(s/b)_{eff.}$ Figure 3.39 and illustrate typical plots of the experimental data and the determined functional relationships.

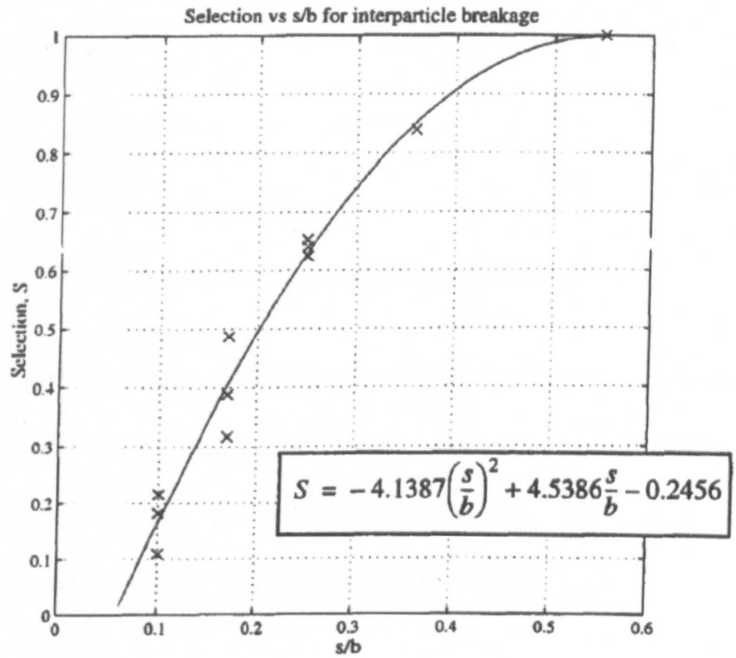

Figure 3.39 Determination of the selection function in terms of the (s/b)eff ratio parameter

(Evertsson and Bearman, 1997)

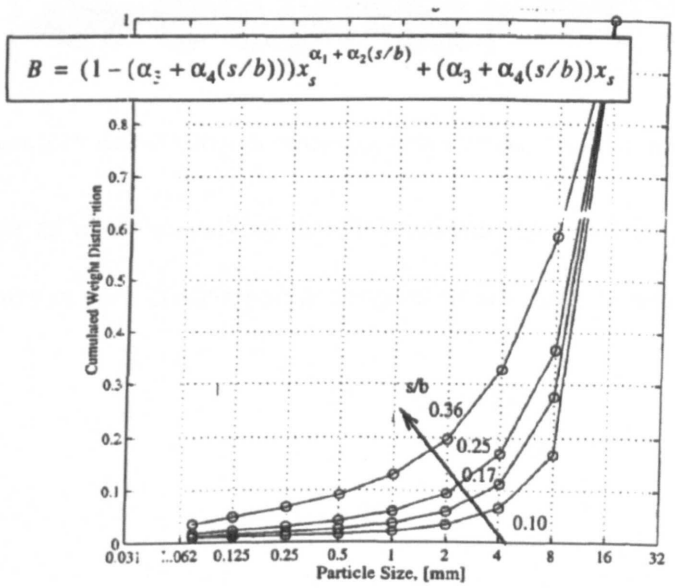

Figure 3.40 Determination of the breakage function in terms of the (s/b)eff and x_S parameters

(Evertsson and Bearman, 1997)

Here X_s is a particle size relative to the initial particle size x_o. x_s is defined as the following expression:

$$X_s = log_2 \left[\frac{X - 0.008}{X_o - 0.008}\right] \qquad \textbf{Equation 3-25}$$

Also, here α_1=21.7759, α_2=-43.4615, α_3= -0.0029, α_4=0.4191

The parameter ratio, $(s/b)_{eff}$, is defined as the effective compression ratio, and is used to compute the pressure and resultant forces. The application of this method can significantly over estimate the material compression and confinement pressure produced within the crusher. It can be illustrated by Figure 3.41

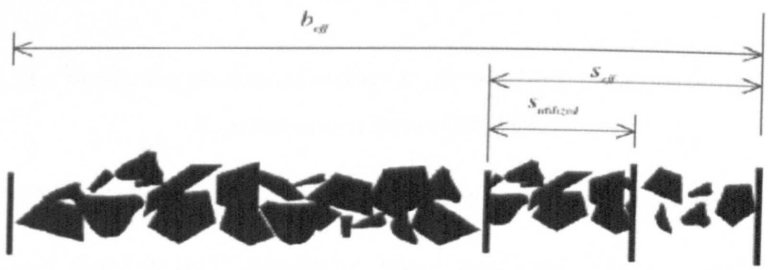

Figure 3.41 Bed of initial thickness b_{eff} with a stroke of s_{eff} (Evertsson, 2003)

A substitution of these classification and breakage functions in the size reduction model generates in each crushing zone the product size distributions shown in Figure 3.42.

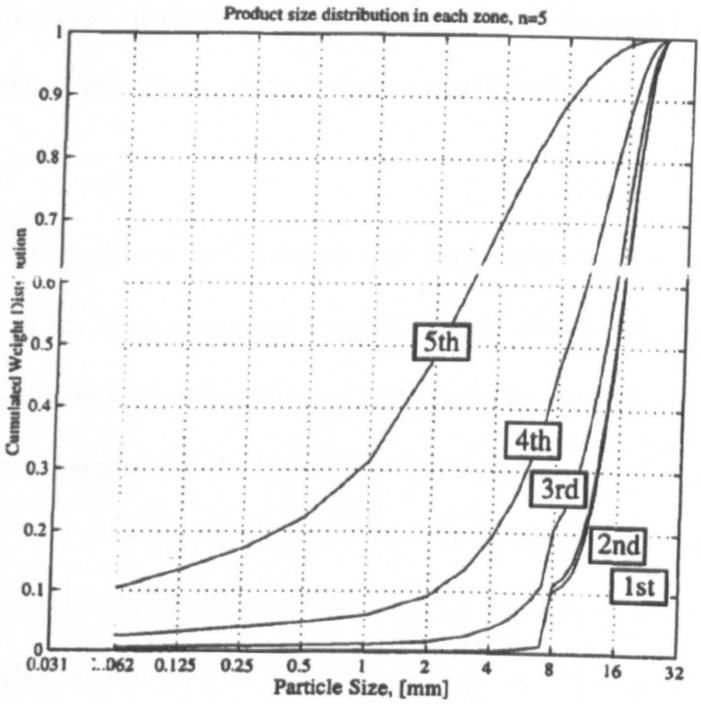

Figure 3.42 The predicted product size distributions within each crushing zone (n=5) (Evertsson and Bearman, 1997)

Evertsson (1997) found that most of the total size reduction takes place during the third, fourth and fifth strokes. However, these predicted models results were not validated against an actual cone crusher performance. The construction of this model also implicitly assumes the material flow through the crusher chamber moves at a constant velocity. However, in reality the velocity of the material flow is variable and will thus make an important contribution to the understanding of how a cone crusher operates.

To address this problem, Evertsson (1998) combined his flow model with a size reduction model. The flow model used is an extension of the Gauldie (1953) model.

Since the crushing process is modelled as a series of sequential crushing stages, the flow model must predict where and how the material is compressed during each size reduction cycle. For a given type of rock material the operators B_i and S_i will depend

on the dimensionless machine parameter $(s/b)_{eff.}$ The flow model should therefore predict the $(s/b)_{eff}$ ratio at the points where a material volume is subjected to size-reduction.

Evertsson (1998) proposed and extension to the Gauldie model that includes the determination of the $(s/b)_{eff}$ parameter within each of the flow zones in the crusher chamber. This requires the delineation of the boundaries for each zone. The $(s/b)_{eff}$ ratios are then calculated for the geometric centre of gravity of each of the zonal cross-sections. The flow model is thus able to accommodate variations to the eccentric speed n and to the nominal stroke rate s_{nom}. In addition, the model is able to compute the effects produced by the specification of different chamber profile geometries.

In conclusion, the development and application of the Evertsson model provides an improved insight into the flow and crushing processes which take place within a cone crusher chamber. However, these models still rely upon limiting number of limiting assumptions that constrain their application. The assumption that the feed material has bulk properties as porous plastic clay may produce erroneous results. The use of an empirically derived rock breakage equation can produce the same breakage results even if the shapes of the initial feed rock stream are divergent. The most important limitation is that the actual behaviour of the rock flow and breakage within the crusher chamber is not explicitly mapped.

3.5.4 DEM modelling of single particle breakage in a jaw crusher

Recently Refahi et al. (2010) proposed a DEM model to represent the breakage behaviour of a single rock particle in a jaw crusher. They used a spherical Limestone

rock particle of a 6cm sieve mesh diameter. The spherical rock specimen was modelled using 30,000 randomly arranged micro-spherical balls with a size distribution across the range of 0.5mm to 1mm. Refahi et al (2010) used both contact and parallel bonds to bind the micro-spheres together. The modelled rock sample is shown on figure 3.43a.

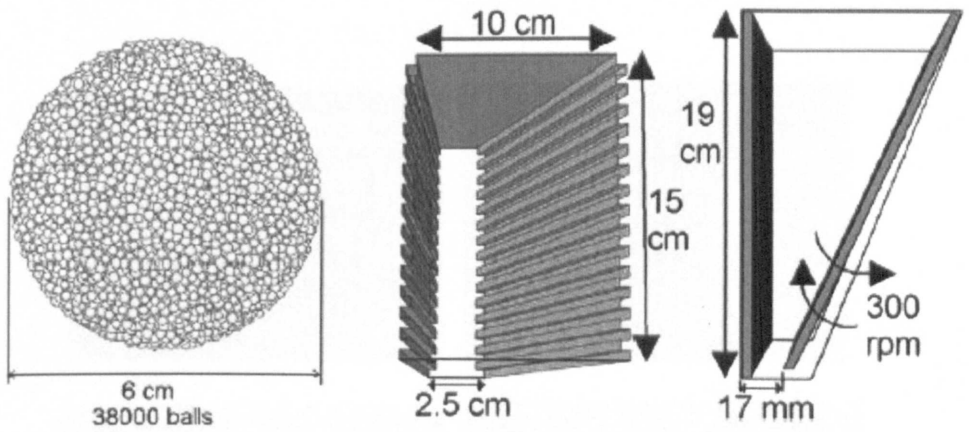

Figure 3.43 (a) Spherical Limestone Sample; PFC3D model of a laboratory jaw crusher in (b) open and (c) closed status

The geometry of the modelled laboratory jaw crusher is shown on figures 3.43(b) and 3.43(c). The position of one of the walls of the jaw crusher is fixed, and the other wall is hinged to the other, leaving an exit portal at the base of the crusher chamber. The hinged wall may open and close between two fixed positions, which define the maximum and minimum volumes of the crushing chamber. As this wall opens and closes, it sequentially confines, traps and crushes the falling material between the two surfaces. The feed entry portal at the top of the crusher chamber is 10cm wide and its maximum and minimum discharge apertures are 250 mm and 17mm, respectively. The rotational speed of the moving jaw is almost 300 rpm.

Figure 3.44 shows the particle breakage process predicted by the DEM model and obtained from the experimental tests. An examination of these figures confirms that the breakage patterns predicted by the numerical models qualitatively replicate those observed in the experiment.. They also found the tensile fracture mechanism will become more dominant than the shear fracture mechanism and the fracture mode of the single spherical rock is tensile in the jaw crusher.

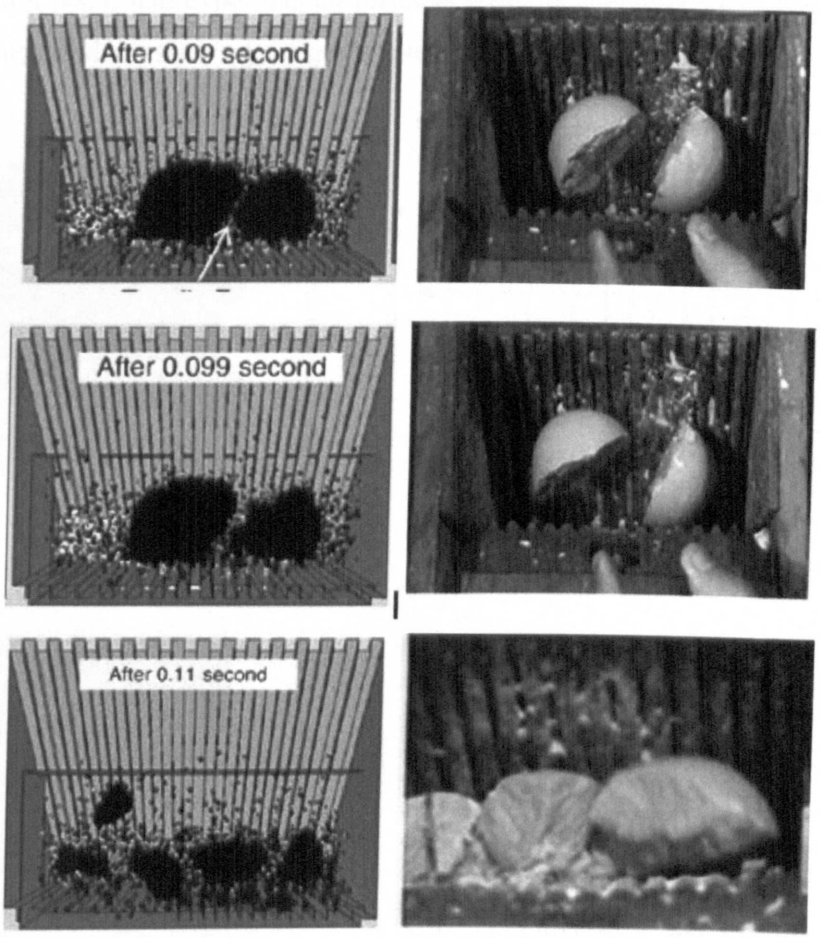

Figure 3.44 A comparison of the breakage patterns predicted by the DEM models and measured by experiment for the spherical limestone particles (Refahi et al. 2010)

Lichter et al (2009) published a paper in which he illustrated his Fast Breakage Model (FBM) modelling cone crusher performance. FBM is combination of DEM and PBM (Population Balance Model). In his model, DEM is only used to model particle flow.

For the rock breakage, he used PBM which can describe rock breakage as a function of the loads on individual rocks.

They modelled two kinds of cone crusher the B90 and HP100. The breakage parameters used are determined from 50mm rock and 25mm sized rock respectively. Figure 3.15 shows the model simulation views and a graphical representation of the actual and the predicted product size distributions. The experimental data was obtained from a series of continuous pilot scale crushing tests conducted at Metso Minerals' crushing facility in Waukesha, USA (Lichter et al, 2009). They compare the simulation result and experimental result in terms of the cumulative passing product size analysis which shows quite good agreement.

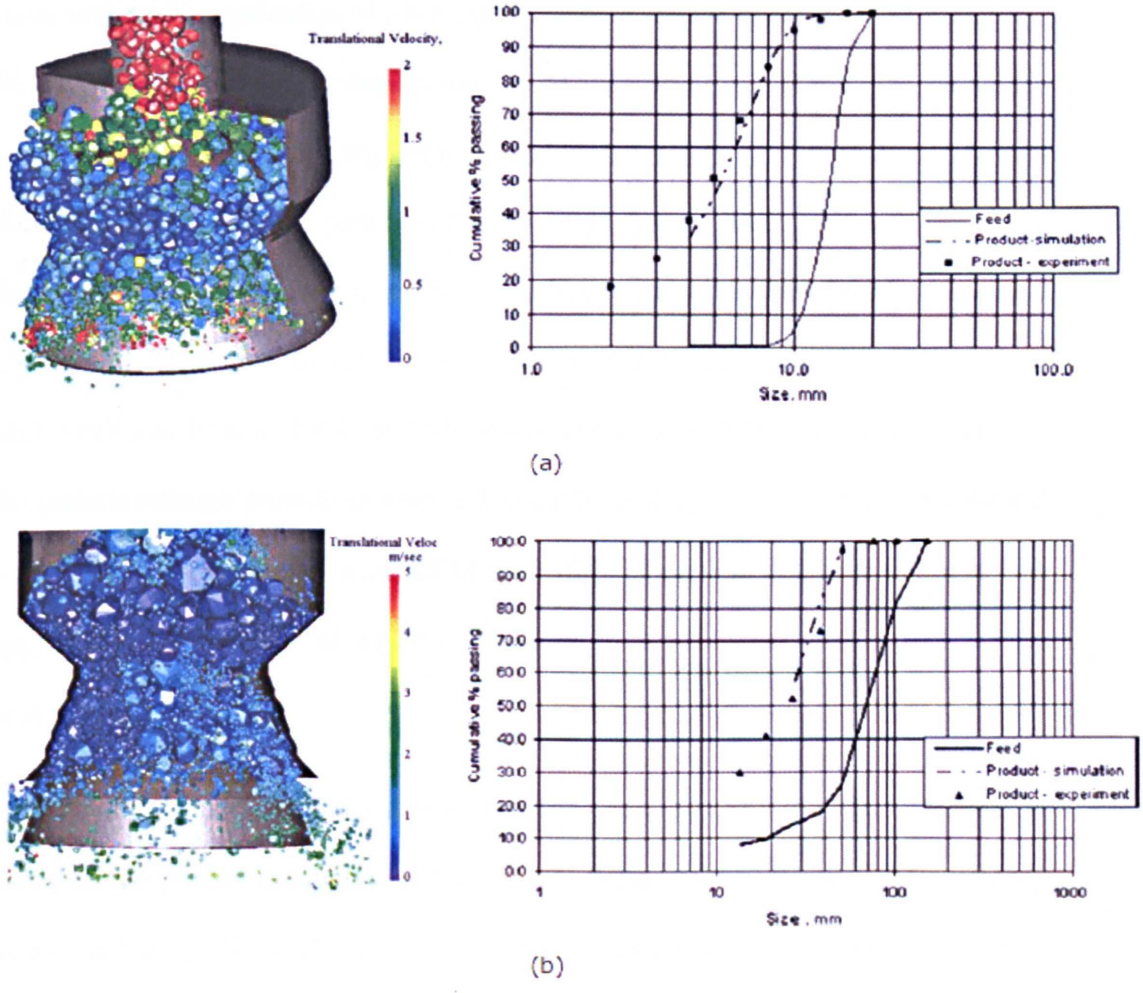

Figure 3.45 Sectional view of DEM simulation and comparision of product size distributions of simulation and experimental (a) B90 (b) HP100 (Lichter et al, 2009)

3.6 Summary

The types of modern crusher machines employed in the mining industry and general working principles of cone crushers were firstly reviewed in this chapter followed by the literature review on the historical research on the mechanical behaviour of granular material flow. The successful applications of DEM on simulating particle flow in a chute/hopper give confidence to model the flow behaviour in the crusher chamber. Zhang and Vu-Quoc's (2000) experimental work on the flow of soybeans in a chute provided some useful ideas for this research to study rock flow behaviour in a chute such as the application of a high speed camera and the plotting velocity profiles. Weibull (1951) statistics has been proved to be appropriate to represent the variability of the tensile strengths in many granular materials for a given size such as ceramics (Davidge, 1979), and soil particles (McDowell & Amon, 2000; Nakata et al, 1999); this finding will be utilized to calibrate the variation of the particle strengths for a given size in the construction of a DEM cone crusher model. Research by Lee (1992), McDowell and Bolton (1998) and McDowell and Amon (2000) on the size effect on the particle strength provide an approach to calibrate the particle strengths of different sizes. The historical research on DEM modelling of particle breakage provides two approaches: PBM and BPM which can be used to construct the cone crusher model using DEM.

The historical mathematical inverse solution cone crusher models, are able to satisfactorily predict product size distributions for a given rock type and feed rock size distribution. These algorithms, validated against experimental data are able to represent the size reduction and flow behaviour produced within a crusher chamber. However, these methods are unable to differentiate the actual staged flow or breakage behaviour as the rock moves through the crusher chamber. It is proposed that the

application of experimentally validated DEM models may be able to improve the understanding of the contributory roles of these two mechanisms. These models may also be used to assess the influence that crusher chamber geometry and rotational speed may have on the performance of cone crusher.

CHAPTER 4

DISCRETE ELEMENT MODELLING OF ROCK FLOW IN A CHUTE

4.1 Introduction

As previously outlined in the Chapter Two, DEM has in recent years been applied to model granular material flow and rock breakage. Previous studies (Zhang & Vu-Quoc, 2000; Li et al., 2004; Li et al., 2009) have demonstrated that DEM models may be used to satisfactorily simulate the flow of granular materials in chutes, hoppers, and belt conveyers This Chapter briefly introduces an extension of the use of these models to replicate the flow of a collection of rock particles observed down a model chute during the execution of a series of experiments in the laboratory. The PFC^{3D} commercial DEM code was used to construct and solve a series of models to replicate these experimental results.

The principal aim of the investigations reported in this chapter is to model the flow behaviour of irregular material in a cone crusher chamber. However, to simplify the model the crusher chamber geometry is idealised as an inclined chute comprising of a fixed rigid base plate, Perspex walls and top plate. As none of the chute walls are permitted to move, it is also assumed that no particle breakage occurs as the material flow descends the chute. Figure 4.1 shows how this laboratory chute rig was

constructed to represent the idealised geometry of a crushing chamber, when the normally eccentrically rotating cone is held in a static position.

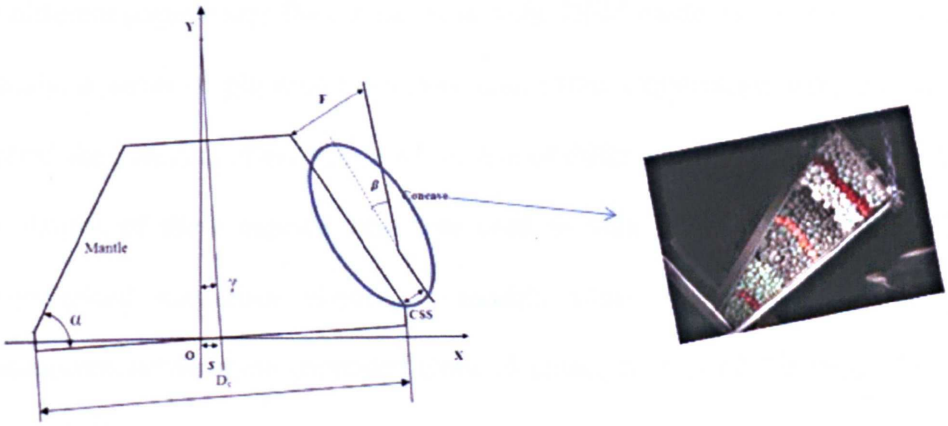

Figure 4.1. The chamber of cone crusher and the chute flow rig

The influence of particle shape can be very significant according to the results of the 2D (Langston et al, 2004)) and 3D (Cleary & Sawley, 2002). DEM modelling studies of granular flows in hoppers confirm the significant influence that the particle shapes can have on the flow behaviours observed. Ferellec & McDowell (2010) also show that the moments of inertia of railway ballast clumps affect the angle of repose. Cleary (2008) demonstrates that as particles become less spherical, the predicted shear resistance of these particles increases as they deform within a loaded Couettte shear cell. To investigate the effects that particle shape can produce as a collection of irregularly shaped particles descend an inclined chute, a series of DEM models were constructed to firstly investigate of the flow of a single-sized collection of regularly (Cleary & Sawley, 2002) shaped particles down an inclined chute. The results of these studies are reported in section 4.2. To study the effects that the gradual reduction in the size of the particles within the rock stream as it flows down the actual crusher

chamber, the model chute was initially loaded with bands of equally sized particles. The particles loaded into each band increased in size from the bottom (discharge portal) to the top (rock feed portal) of the chute. Section 4.3 describes the location of the different particle size flow zones within the DEM model of the crusher chamber. Initially, a series of physical laboratory chute flow experiments were conducted to confirm the practical effectiveness of the use of differently sized particle flow zones. The results of these experiments were used to validate the DEM models. These parameterised numerical simulation models were then used to identify the relationships between the computed chute clearance times, and the chute closed-size setting (CSS) and the bite angle.

4.2 Importance of particle shape in DEM flow models

4.2.1 Experiments procedure

A series of experiments to characterise granular particle flows were conducted using regularly shaped rounded river gravel pebbles (Figure 4.2). The sieve size of the pebbles selected was in the range 19-22.4mm. Figure 4.3 shows a collection of photographs that illustrate the components and construction of the experimental apparatus. The experimental rig was designed to consist of a rectangular open top chute, with a polished metal base and with Perspex side walls, enabling a side elevation view of the descending particle flow stream to be observed. The chute is mounted on a supporting metal frame, and the discharge end of the chute is attached to this frame by a pivot hinge attached to the base of the chute. This arrangement allows the top, feed end of the chute to be raised by a hydraulic lift arm, allowing the chute to be inclined about its fixed pivot point. The chute may be raised from the

horizontal to a fully vertical position. A metal sliding gate mounted within a frame is attached to the discharge located at the bottom of the chute. The feed located at the top of the chute can be sealed by the attachment of a Perspex plate. The chute was normally loaded with river gravel pebbles when it was resting horizontal on the supporting frame. When the chute is inclined the sliding gate at the discharge end of the chute can be opened to allow the confined material to flow out under the action of gravity into a collection bin. As the material flows down the chute its flow behaviour may be recorded by a fast frame video camera of 500 frames per second through the side elevation Perspex walls. The recorded digital still frames of the recorded video footage may then be analyzed to track the relative motion of the rock particles.

Figure 4.2 Experimental material: river gravel pebbles

The components of the experimental rig are listed as follows:

- A black tent which is used to exclude external light.
- 300mm (width) by 600mm (length) 10 mm thick steel chute base
- 300mm(width) by 200mm(height) with 10mm (depth) optical quality Perspex side walls X2
- 600mm(width) by 200mm(height) with 10mm (depth) optical quality Perspex sides X2

- A collection of 1680 rounded shaped river gravel pebbles. The sieve size of the pebbles is ranged from 19mm to 22.4mm and dyed black or white. Twenty pebbles were randomly selected and dyed red.
- A pivot hinge is attached to the bottom of the discharge end of the metal base plate. The hinge is attached to the metal supporting frame.
- A solid supporting frame with adjustable height feet attached to the legs of the frame. This allows the frame and chute to be levelled to the horizontal.
- A chain lifting cradle attached to the base of the feed end of the chute.
- A hydraulic lift arm, attached to the lifting cradle.
- A fast frame video camera
- A spirit level gauge. To ensure that the chute supporting frame is level to the horizontal.
- A protractor gauge used to confirm the angle of inclination of the chute.

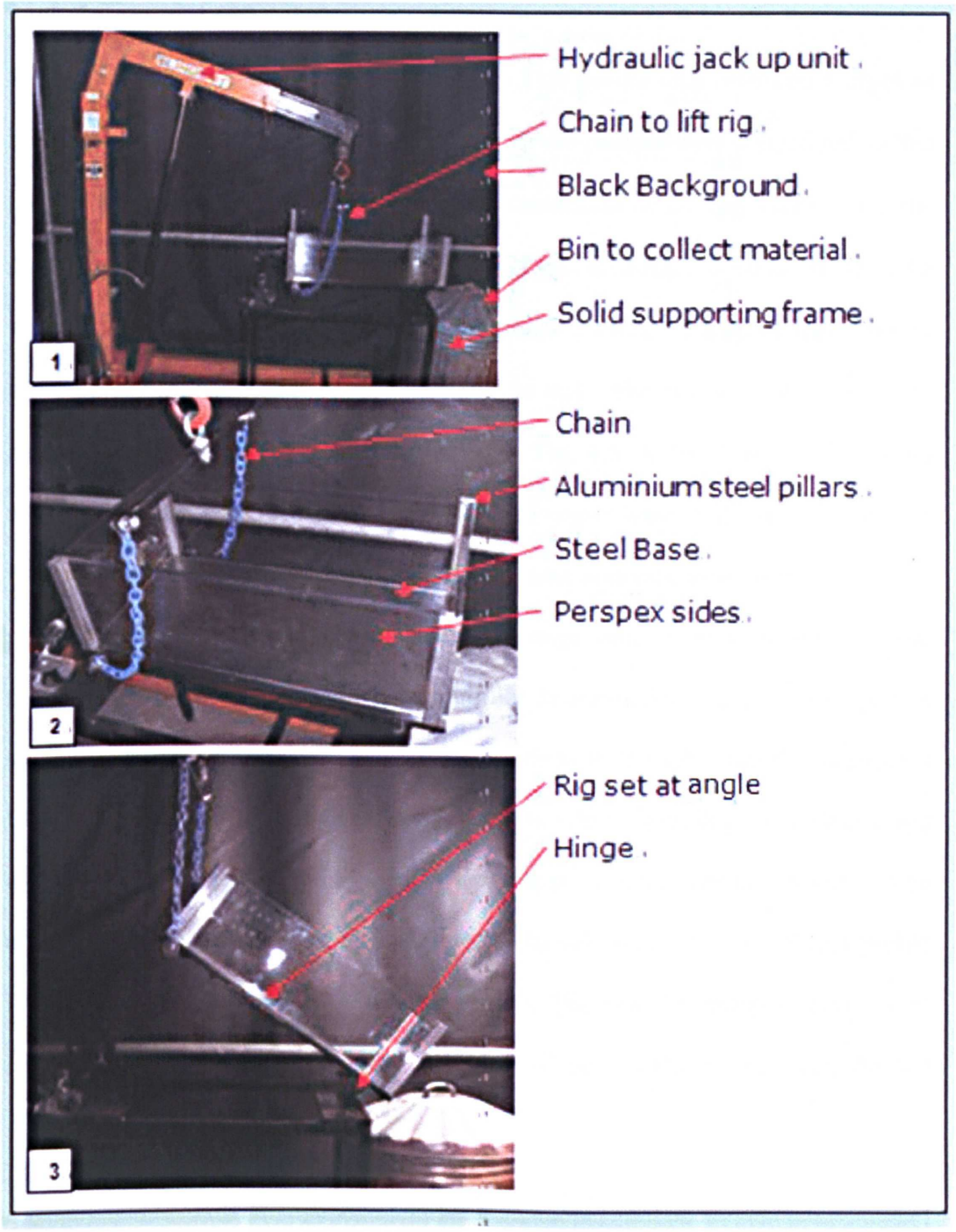

Figure 4.3 The detail the chute rig

An initial set of experiments was performed using the chute loaded with a charge of single sized set pebbles (Figure 4.4). The experiments were performed for chute discharge inclination angles of 27, 30 and 33 degrees. At the preparation for each test,

total charges of 1,680 pebbles were poured into the chute from the feed portal at located at the top right hand end of the chute.This pebble load produced a depth of approximately 80 mm, as shown in Fig. 3; 20 of the pebbles were painted red so that their movements could be tracked from an examination of the fast video stills. The coefficient of friction of the red painted pebbles was confirmed to be the same as the undyed pebbles. Four red pebbles were positioned by hand in each of five columns spaced 100 mm apart next to the Perspex side wall. The positions of the five red marker pebble columns (1–5) are illustrated in Fig. 4.5. A fast frame video camera recorded the discharge flows through one of the Perspex walls. Stills frames extracted from the fast video tape recordings at regular time intervals were used to track the passage of the red marker pebbles and the average velocity profiles of the pebble flows computed. The computed velocity profiles determined for each test were plotted so that they may be compared against the solutions to the subsequently constructed DEM models. Figure 4.5 shows an example of the velocity profile plots of determined after each test. The origin of each velocity profile is the initial position of the column of marker pebbles whose movements it tracks. The yellow curve is the velocity profile for the column of red pebbles at each marker. The velocity profiles curves were computed using the measured average velocities of these marker pebbles over the first 100 mm horizontal displacement.

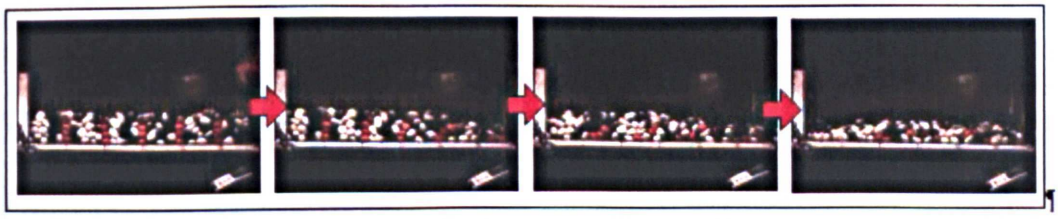

Figure 4.4 Single sized pebbles flow of chute model

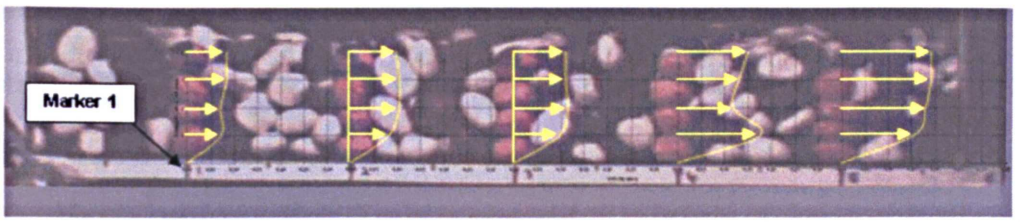

Figure 4.5 The generation procedure of velocity profiles

The travel of the experimental material flows were only computed over the first 100 mm out of travel due to the following two reasons:

- After 100mm of travel the depth of the pebble flow changes such that the paths of the marker pebbles deviate significantly from a track parallel to the chute base, thus increasing the complexity of the velocity calculation,
- Realistically, within the crusher chamber the pebbles will have experienced an expansion and compression cycle, changing the flow volume available, and hence the flow field of the marker pebbles.

4.2.2 DEM simulation procedure

The contact model used in this model is the linear contact model, which is defined by normal and shear stiffness of the two contacting entities. The contact force is obtained from the magnitude of the overlap at each contact via a constitutive law, and the accelerations, velocities and displacements of the modelled pebbles computed by an application of Newton's second law via the use of an explicit time-stepping scheme (the details of these numerical calculation methods were introduced in section 2.5.1). A slip model (see section 2.6.2) is also added to the ball-ball or ball-wall contacts.

It is well known that particle rotation plays a dominant role in particle flow. Rolling resistance will be significantly different for different particle shapes. Some authors have introduced artificial rolling resistance at contacts in DEM using spheres to try to

account for the effect of particle shape (e.g. Iwashita & Oda (1998)). However, this method is used simply if only spheres are available and does not correctly model the particle mechanics. In this research, particle shape is accounted for directly, so the extra rolling resistance due to the particles being non-spherical is automatically accounted for and is much more representative of the real granular material. The pebbles were modelled using spheres and, alternatively, ellipsoid four-ball clumps, shown in Fig. 4.6. The four overlapping spheres form a clump that is only deformable at its boundary and in which internal contacts are ignored; clump logic is explained section 2.7. The four spheres in the chosen clump have equal radii and have their centres lying on a single plane. The simulation process followed is detailed by the following steps :

- The volume of the empty chute was filled with the same number of particle spheres or clumps generated inside a higher chute, but with the same length and width with the experimental chute, allowing the particles to freely flow and randomly distribute and to finally come to rest within the chute as shown in Fig. 4.7a.
- When the loaded particles came to rest within the chute, the particles whose centres lie closest to the 20 red marker pebbles in the laboratory experiments were thus marked for the execution of the numerical simulations (Fig.4.7b).
- In addition to the normal vertical gravity force, an additional horizontal gravity force was applied to the DEM models to include the effects produced by the inclination of the chute from the horizontal in the laboratory experiments (Fig. 4.7c). The introduction of this separate stage in the formation of the numerical model is to decrease the computational time.

- As in the experiment the chute is loaded in a horizontal position and then gradually raised to a given angle of inclination, during this process the positions of the pebbles may slightly displace. To permit the slight displacement of the particles experienced on the inclination of the chute, the numerical solution is initiated to complete a total of 5,000 incremental time-step cycles (time-steps) prior to the application of the horizontal gravity component.
- Remove the retaining wall at the discharge end of the inclined chute, and compute the velocities of the red marker pebbles and the clearance time taken for all the pebbles to clear the chute.

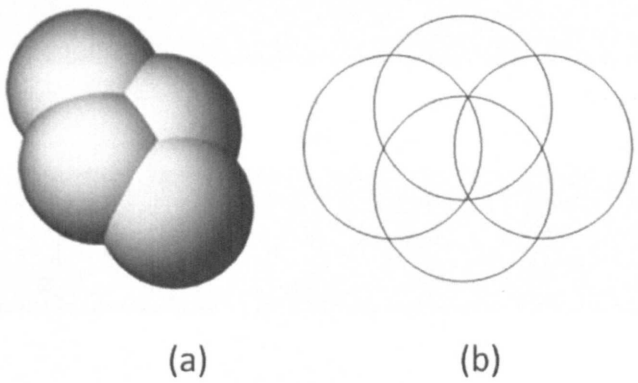

Figure 4.6 (a)The shape of ellipsoid particle (b) A view cross-sectional view of the ellipsoid clump

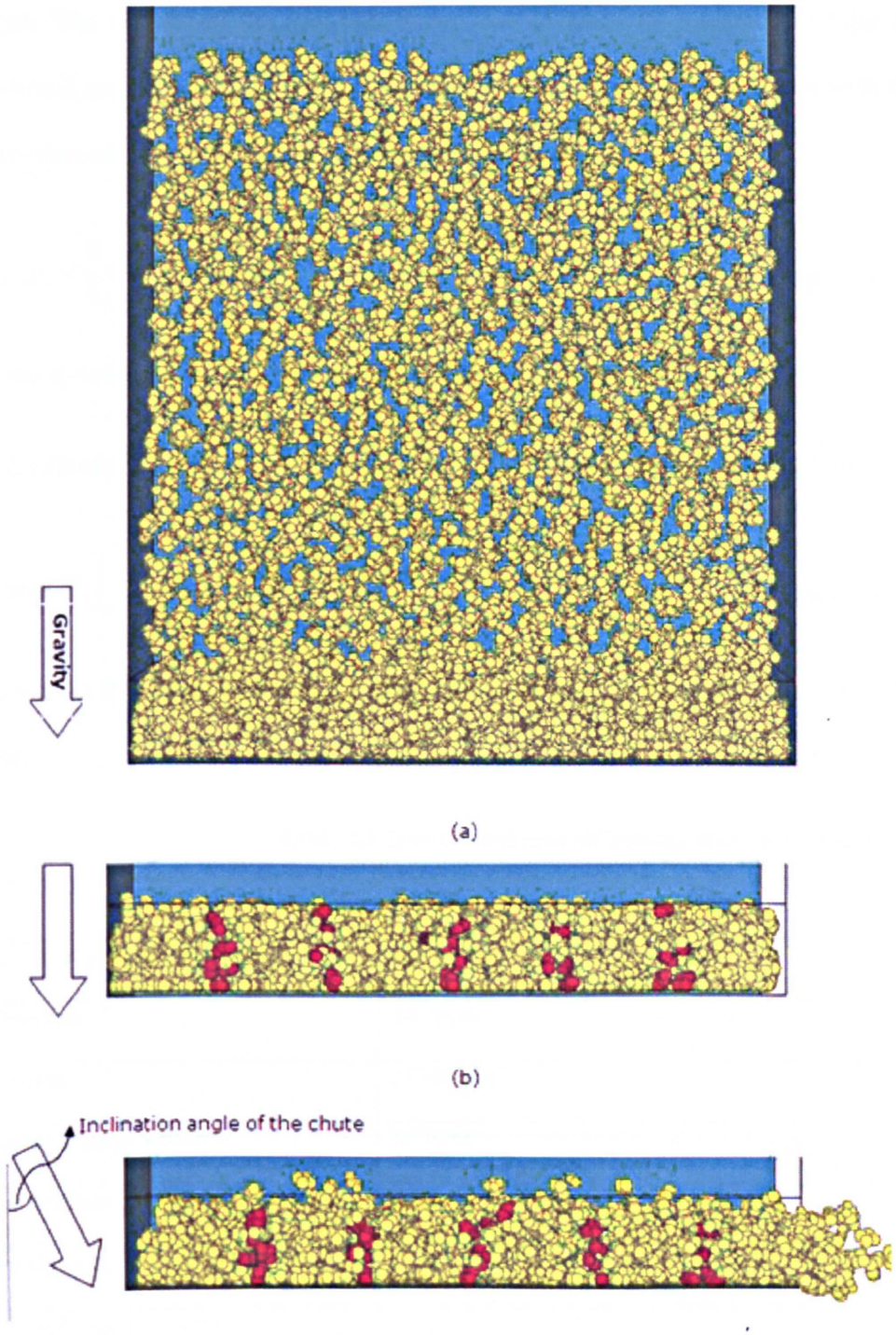

Figure 4.7 The simulation procedure of homogenous flow

4.2.3 Particle parameter decision

Table 4.1 shows the input parameters for the particles. The diameters of the spheres within the clump and the spheres were determined by equating their volume to the volume of a typical pebble used in the experiments, determined by displacement of

water. The volume of the four-ball clump was obtained by integration of the cross-sectional area (see Figure 4.6b) multiplied by an infinitesimal thickness with depth. The cross-sectional area (Figure 4.6b) was calculated as:

$$A_{cross} = \frac{5}{3}\pi {r_c}^2 + \frac{3\sqrt{3}}{2}{r_c}^2 \qquad \textbf{Equation 4-1}$$

where r_c is the radius of a single sphere of the cross-sectional view.

The volume of the clump was obtained by the integration of the cross-sectional area:

$$V_{clump} = \int_0^{2r} (\frac{5}{3}\pi + \frac{3\sqrt{3}}{2})(r^2 - x^2)dx = (\frac{20\pi}{9} + 2\sqrt{3})r^3 \qquad \textbf{Equation 4-2}$$

where r is the radius of a single sphere of the clump, x is the depth of cross-sectional area.

Table 4.1 Input parameter of homogenous flow model

	clump	sphere
Number of particles:	1680	
Diameter:	14.7mm	20mm
Density:	2730kg/m^3	
Normal/Shear stiffness:	10^{9}N/m	
Particle/particle friction coefficient	0.37	
wall/particle friction coefficient	0.50	
Critical damping ratio:	0.11	

This clump volume was then used to determine the diameter of the spheres required to form the clump. The application of a simple inverse solution method to solve a DEM model to replicate the results of experimental pebble heap tests, provides estimates to

both the static angles of repose and to the particle–to-particle friction coefficient for irregularly shaped particles used in the DEM pebble chute flow models (Ferellec & McDowell, 2010). The heap test is a static angle of repose test. The solution algorithm is as follows:

- A given number of single sized river pebbles were initially poured onto a level table, and permitted to flow until the granular material formed into a static heap. The experiment was repeated twenty times, to measure the angle of repose of each static heap and to then compute the average angle of repose of the twenty experiments (Fig. 4.8(a)
- A DEM model to replicate the experimental heap tests (Fig.4.8(b)) was constructed using a four-spherical ball clumps to represent the single sized pebbles. The numerical models were solved by incrementally changing the friction coefficient for the clumps numerical models until the predicted angle of repose matched the average value determined from the experiments. The coefficient of friction for the level table surface beneath the static heap was determined to be 0.605 which is measured by lifting the bottom wall until a single pebble starting to flow on it.
- A plot of the predicted heap angle against the modelled pebble friction was produced is shown in figure 4.8(c).
- The pebble friction coefficient that produces a DEM model heap angle value equal to the average value measured from the experiments was determined.

The average angle of repose computed from the twenty experiments executed was 26.03 degrees with a standard deviation of 0.6. Fig. 4.8(c) details the determination of the corresponding particle–particle friction coefficient as 0.37. This value is lower

than the coefficient of friction for the level table beneath the heap. In addition, from an examination of the parameter values presented in Table 4.1, the values of the chute wall coefficients exceed those of the particles. Since the models used by the PFC^{3D} code use the lower of the coefficients of friction for two contacting entities, the ball–to-wall coefficient of friction employed in the solution of the DEM models was 0.37.

(a)

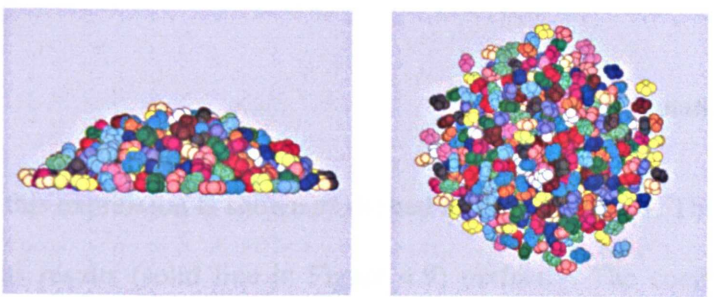

(b)

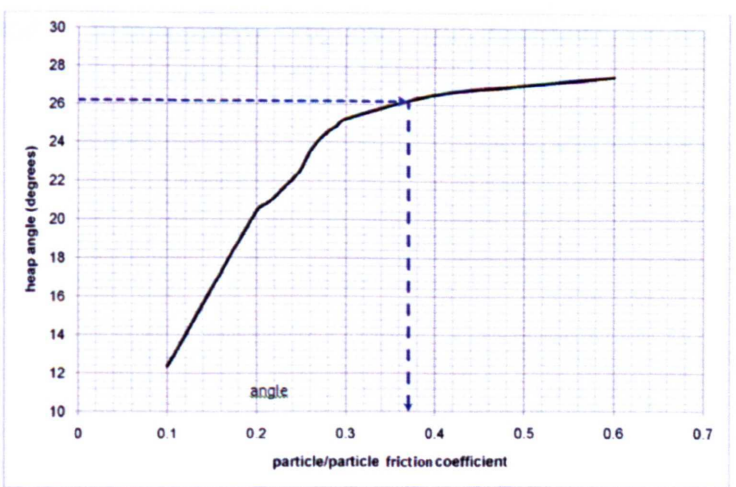

(c)

Figure 4.8 . **(a) Experimental heap test. (b) DEM simulation of the heap test. (c) Relationship between the angle of repose and particle coefficient of friction in the DEM simulation**

An important factor in the modelling of dynamic flow is damping. In the chosen program, a viscous damping system (detail introduced in section 2.5.1) is used to model the coefficient of restitution by adding normal and shear dashpots at each contact. The coefficient of restitution e can be measured by dropping a particle vertically onto a horizontal wall, and is given by:

$$\varepsilon = \sqrt{\frac{h}{H}} \text{ or } \varepsilon = \frac{v\_a}{v\_b} \qquad \textbf{Equation 4-3}$$

where h is the rebound height and H denotes drop height. The quantity v_a is the speed of the particle after impact and v_b is the speed of the particle before impact. The coefficient of restitution is related to the critical damping ratio b according to (Schwager & Poschel, 2007):

$$\varepsilon = -\frac{\beta\pi}{\sqrt{1-\beta^2}} \qquad \textbf{Equation 4-4}$$

A graphical plot of this expression is shown as dashed line in Figure 4.9. This fits the simulation drop tests results (solid line in Figure 4.9) perfectly. The coefficient of restitution for the pebbles was determined in the laboratory to be 0.72 as an average value from a total of 20 consecutive drop tests. This determines the critical damping ratio to be 0.11.

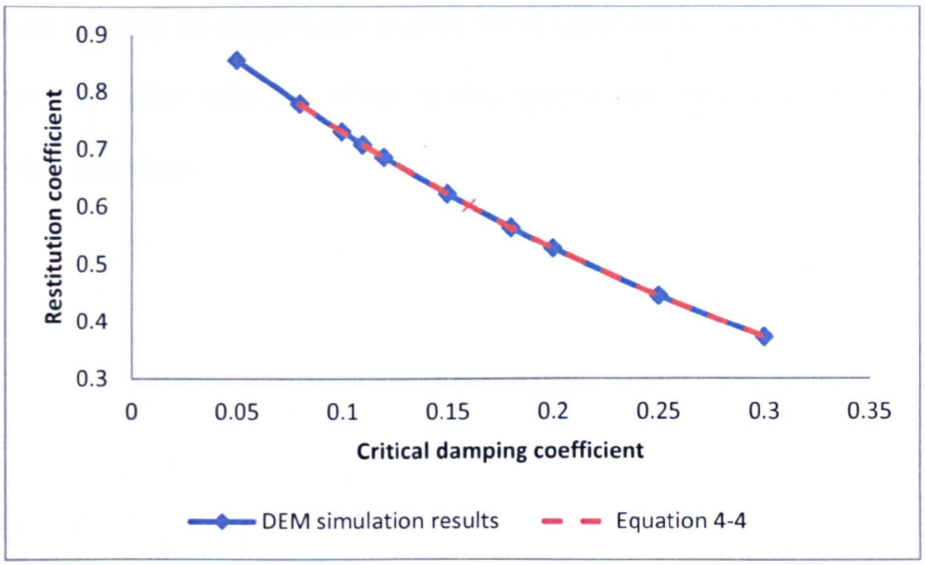

Figure 4.9 A plot of the computed relationship between the critical viscous damping ratio and the restitution coefficient

4.2.4 Results

A series of DEM model simulations were subsequently performed to represent chute inclination discharge flows set at 27, 30 and 33 to the horizontal. The velocity profiles obtained from the experiments and the DEM simulations are shown in Figure 4.10(a)–(c). It is clear that the velocity profiles of the clumps match those of the real pebbles much better than those of the spheres. In general, the spheres flow faster than the clumps and pebbles. For the pebbles located from mark 1 to mark 4, the spheres flow nearly twice as fast as the clumps and real particles. The average difference between the clump velocity profile and experimental velocity profile is only 0.03 m/s, whereas this value is 0.1 m/s for the spheres. The best agreement seems to occur at an inclination of around 30 degrees, with the clumps, in general, slightly slower at 27degrees and slightly faster at 33degrees. Figure 4.11 shows the relationship between clearance time and the inclination angle of the chute. The clearance time is simply the time taken for all pebbles to flow out of the chute. Clearly, there is good

agreement between the experiments and the DEM simulations using four-ball clumps. However, the higher velocities of the tracked spheres are consistent with the much lower clearance times.

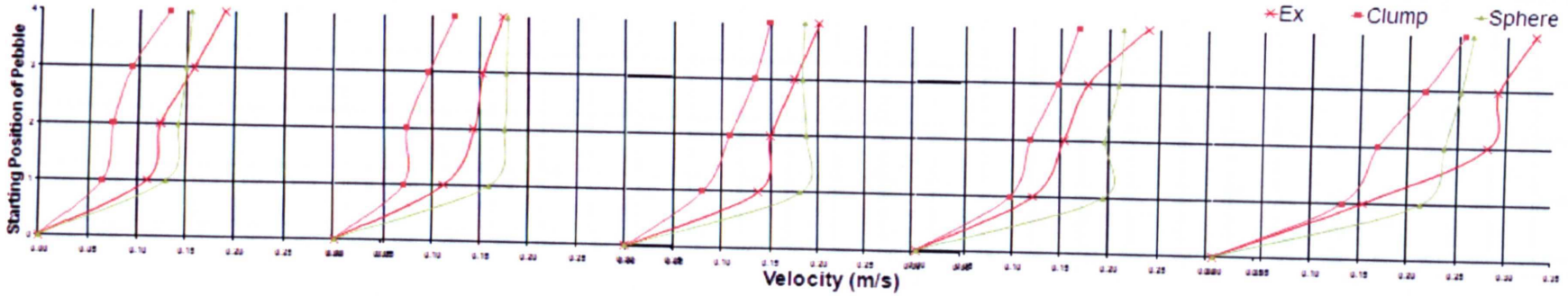
Ex
Clump
Sphere
Starting Position of Pebble
Velocity (m/s)

(a)

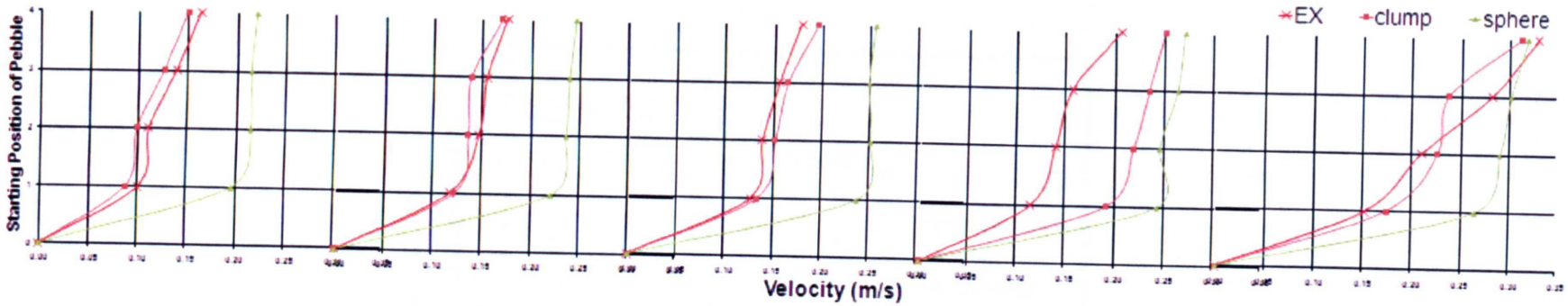
EX
clump
sphere
Starting Position of Pebble
Velocity (m/s)

(b)

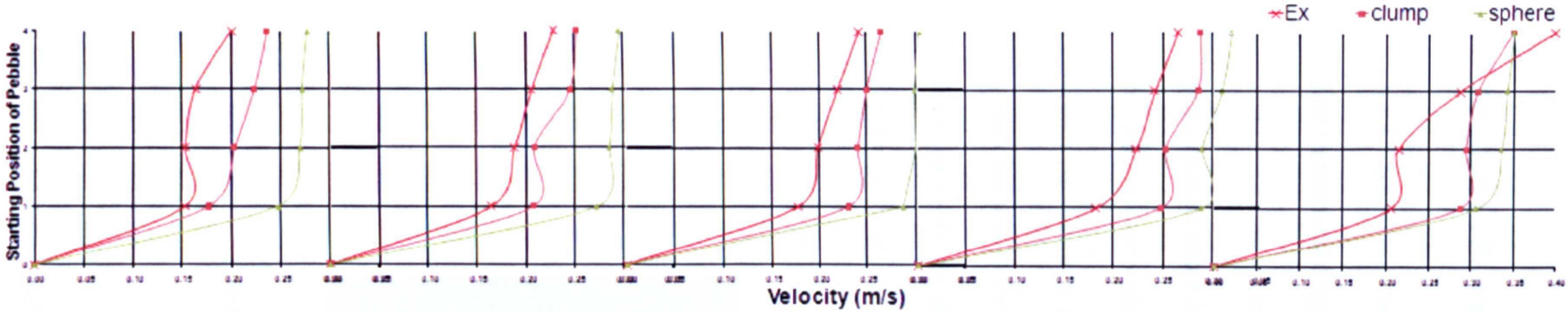

(c)

Figure 4.10 velocity profile of homogenous flow of DEM chute model: (a) 27 degrees (b) 30 degrees (c) 33 degrees

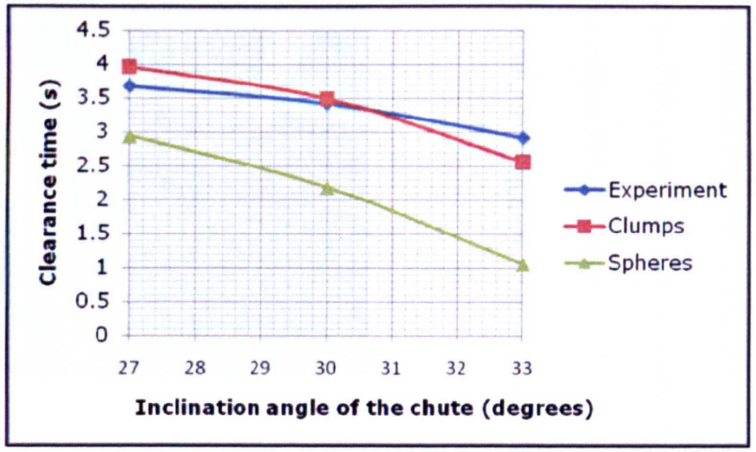

Figure 4.11 Clearance time versus the inclination angle of the chute

4.3 Zones flow model

4.3.1 Experiments procedure

The experimental rig used to conduct this set of experiments is essentially the same as that detailed in section 4.2, and shown in Figure 4.2. However, the geometry of the experimental chute is modified to more realistically represent a cone crusher chamber by adding a top plate. Figure 4.12 shows the experimental apparatus. The chute, which consists of a steel bottom and transparent Perspex sides, can be raised around pivots located at both ends of the chute. The chute may be inclined at an angle of between 0-90° to the horizontal about either hinged pivot point. The material is discharged from the chute by the removal of a sliding gate located in a frame mounted at the discharge end of the chute.

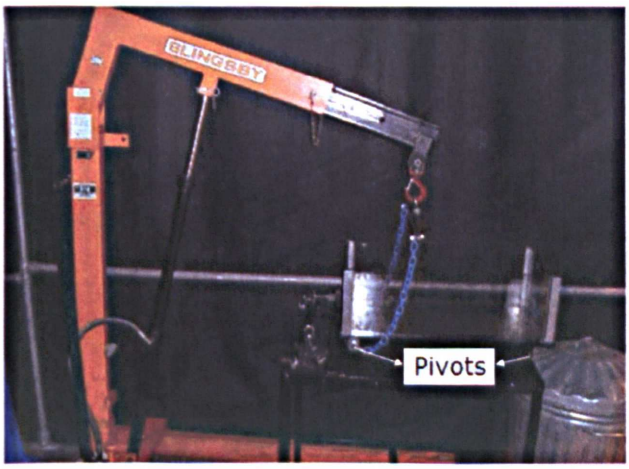

Figure 4.12 Experimental rig for zones flow experiments

Figure 4.13(a)-(b) shows the geometry of a real cone crusher chamber and the simulated flow chute. The fixed height of the top plate above the base plate at the discharge end of the chute represents the close size setting (CSS) of a real cone

crusher- and defines the smallest distance between the outer concave wall and the mantle. The bite angle β denotes the angle made by the top plate to the base plate of the chute. This represents the angle between the concave wall and the mantle in the real cone crusher. The base plate of the chute was 600mm long and 300mm wide. The depth of the CSS can be adjusted to a height of between 40 to 50mm, whilst the bite angle, β, can be set at 18, 20 or 22°. For the laboratory experiments performed, the inclination angle of the chute was set at 45° to the horizontal, to more closely replicate the real geometry of a typical cone crusher chamber.

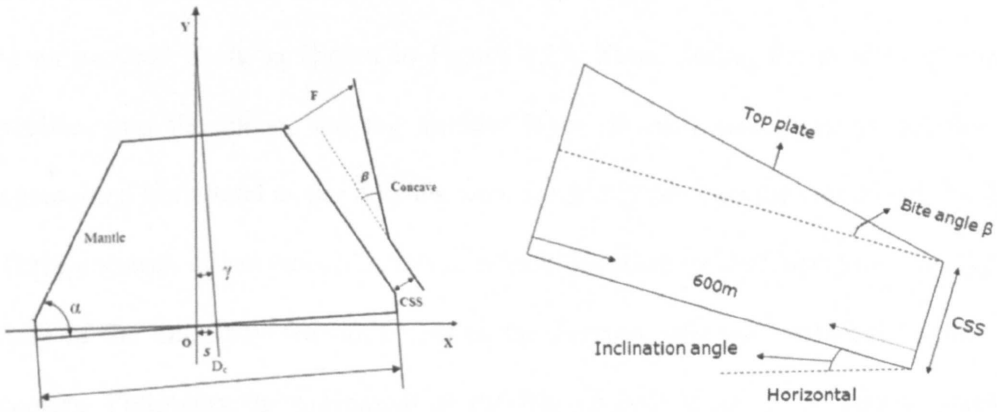

(a) (b)

Figure 4.13 Real cone crusher chamber (a) and the laboratory chute (b) showing the bite angle and closed-size setting (CSS).

Figure 4.14 shows the zones of the placement of the different single sized particle loads used to simulate the size reduction in the material due to crushing as it flows down the cone crusher chamber. To represent this process, the size of the material placed into each of the zones reduces from zones numbered one to nine. To solely characterize the flows produced by such graded particle streams, a series of experiments were performed whereby the experimental chute was divided into three

equidistant zones that were initially filled with pebbles in three different size classes. The sieve sizes for the three chosen size fractions of pebbles were 19-22.4mm, 16-19mm and 12.4-16mm. To enable visual identification of the movement of the different pebble size fractions during chute discharge, the resultant side elevation views of the flows were recorded through the Perspex wall using a high speed fast frame video camera. The three size fractions in descending size order were painted white, black and green, respectively. The pebbles could not be deposited correctly in the chute with the base horizontal as the top surface was not horizontal so pebbles would roll down to the lower end of the chute. The pebbles were therefore deposited in an inclined chute as shown in Figure 4.15. Thus, during the process of loading pebbles into the chute, the top surface layer of each size class of pebbles was maintained horizontal as the pebbles were randomly put into the chute layer by layer. Three columns of red painted same sized pebbles were located along the mid layer of each of the three size fractions next to the Perspex side wall adjacent to the video camera. Following the placement of the final pebble layer in the largest sized top pebble zone, the feed plate was attached and fixed. The base plate of the chute was then returned to the horizontal, before being inclined to an angle of 45° to the horizontal. Figure 4.16 shows the chute before the discharge plate is raised to release the flow of pebbles. The motion of these marker pebbles was tracked from an analysis of the stills frames extracted from the fast video camera recordings. The recording speed of fast video camera recordings was 500 frames per second, the frame stills were recorded onto the hard disk of a laptop computer to allow subsequent digital analysis. Figure 4.17 shows an example of the plots of velocity profiles determined from an analysis of the motion of the marker pebbles from the video stills of the chute flow experiments performed. The origin to each of the plotted velocity profiles is at

the intersection of the chute base plate and the bottom of the red marker pebble columns. The computed velocity profiles for each column of red pebbles are plotted. The curves represent the computed average velocities for the columns of red marker pebbles for the first 100 mm of recorded displacement (see section 4.2.1).

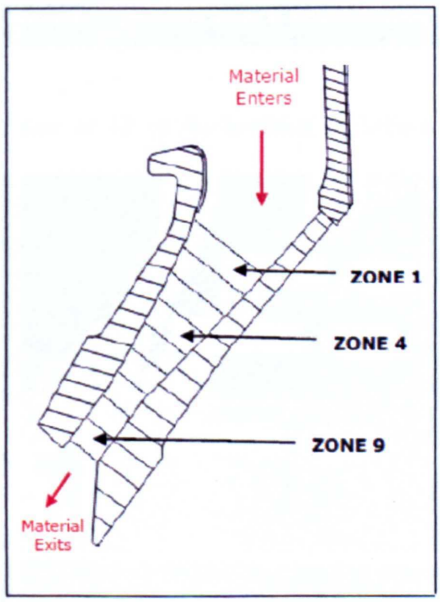

Figure 4.14 Zones flow in the crusher chamber

Figure 4.15 Method of deposition of pebbles in the laboratory

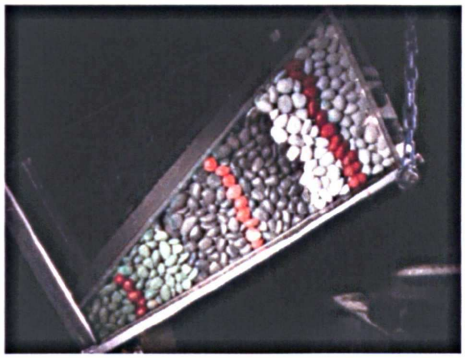

Figure 4.16 Chute with base at 45° to the horizontal, before releasing the trap door

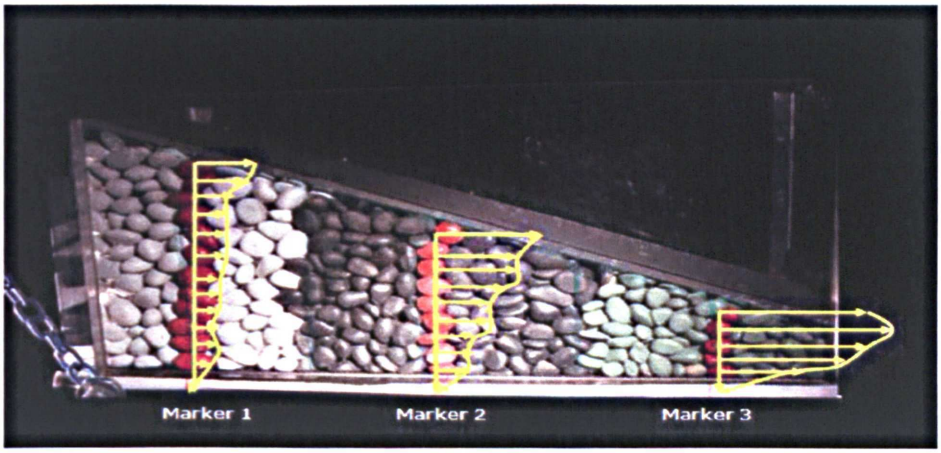

Figure 4.17 Example of determination of velocity profiles

4.3.2 DEM simulation procedure

A series of DEM models were subsequently constructed and solved to replicate the results of the experimental studies described above. The contact and shape of the clump models used in these simulations is the same as those described in section 4.2. The values of the physical particle and chute parameters decision were the same as those described in section 4.2.3. and listed in Table 4.2.. Clump particle models were formed to represent the three size fractions of pebbles used in the experiments. The The equivalent diameters of each clump size was determined by equating its volume to the average volume of the pebble size class fractions used in laboratory

experiments. The interparticle friction was chosen so as to achieve the same angle of repose in the DEM simulation as in the laboratory for the real pebbles by using a simple slump test (section 4.2.3). The energy dissipation at contacts was modelled by the viscous damping model, and characterised by the critical damping ratio. The critical damping ratio was calibrated by comparing the results of the computed model simulation drop tests with corresponding observed laboratory drop tests (section 2.5.1). A single coefficient of restitution was assumed for ball-wall impact and ball-to-ball impact due to the difficulty in measuring the latter in the laboratory.

Figure 4.18(a)-(c) shows the procedure used to generate particle samples. Clump particle models of three size fractions were randomly generated in the three zones by the use of temporary model walls positioned horizontally across a vertically mounted tall chute (Figure 4.18(a)) . The particles were then allowed to free-fall under gravity and come to rest at the bottom of the chute. An additional gravity force component was applied to represent the force generated by an inclination of the chute in the laboratory experiments (Figure 4.18(b)). When the simulated particles reach a stable equilibrium, the temporary walls at the interfaces of the particle zones and the clump particles that intersect the top feed plate are removed. The clump particles whose centres are closest to the centres of columns of red marker pebbles in experiments, are selected as the corresponding marker clumps in the DEM simulations. An additional gravity force is then applied at the same inclination angle (45°) to the horizontal of the base plate of the chute in the laboratory experiments (Figure 4.18(c)). In order to establish the effect of clump deposition and therefore orientation in the DEM modelling of the flow of the pebbles, simulations were also performed with clumps deposited under vertical gravity with the base horizontal, as shown in Figure 4.18(d).

The simulations was repeated three times (three different randomly created clump particle samples), and the average values of these computed results were compared against the average of the measured experimental results.

Table 4.2 Input parameters for zones flow model

	Large clump	Medium clump	Small clump
Diameter (single sphere, mm)	14.7	12.8	10.4
Mass (g)	12.3	9.7	7.4
Normal/shear stiffness (N/m)	10^9	10^9	10^9
Particle/particle friction coefficient	0.37	0.37	0.37
Side wall/particle friction coefficient	0.605	0.605	0.605
Bottom wall/particle friction coefficient	0.493	0.493	0.493
Critical damping ratio	0.11	0.11	0.11

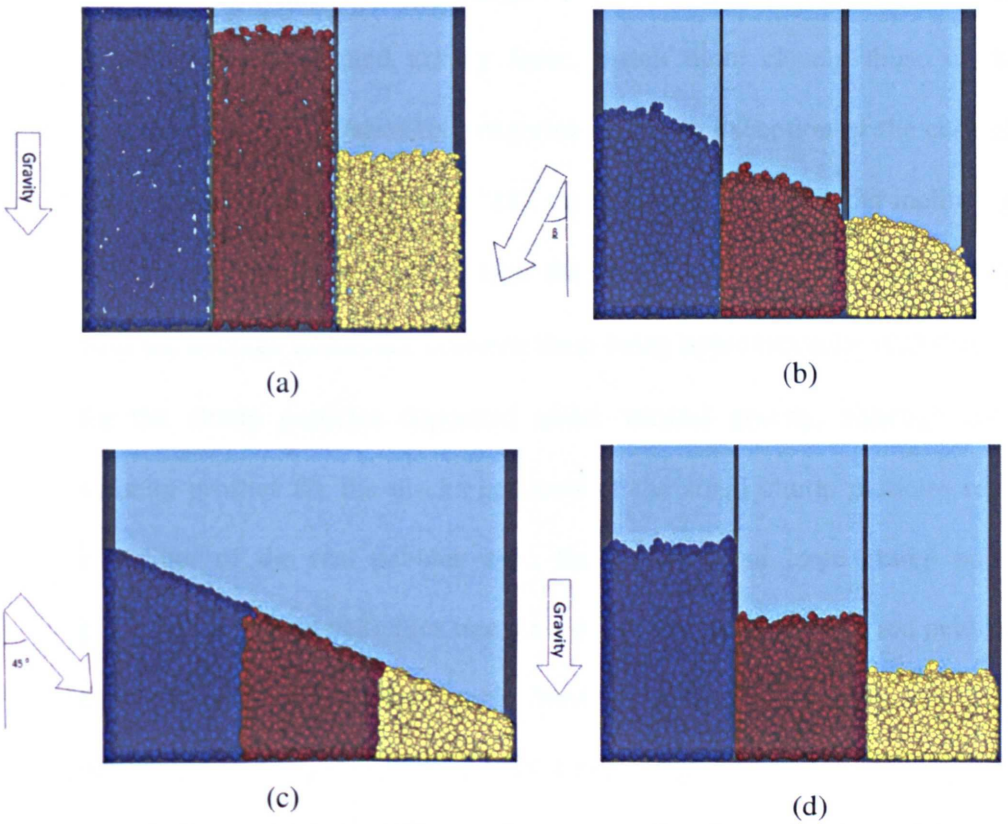

Figure 4.18 Sample generation: (a) clumps generated in a tall chute, (b) clumps deposited by inclined gravity, (c) artificial walls and extra clumps deleted and gravity applied at 45°, and (d) clumps deposited by vertical gravity.

4.3.3 Results

Clump deposition and model validation

When gravity is applied to the modelled particles from different directions, this may produce a range of different orientations of the generated particle samples in the chute, which in turn may have an effect on the subsequent simulated discharge flows. Figure 4.19(a)-(c) presents a comparison of the velocity profiles of the red marker pebbles obtained both from the laboratory experiments and from the solution of the parallel DEM models for a discharge CSS of 50mm and bite angles, β, set at 18° 20° and 22°, respectively. An analysis of the data presented on Figures 4.18 concludes that

the velocity profiles of the discharge flows of the clump particles deposited under the influence of an inclined gravity force, match more closely those of the pebbles measured during the laboratory experiments. With exception of the case of the large clump particles at a bite angle of 18°, the clumps deposited under inclined gravity are observed to flow only slightly faster than the pebbles in the laboratory experiments, with the average difference between them being approximately ±0.005m/s. However, for the clump particles deposited under vertical gravity, although the predicted velocity profiles for the discharge flows of the small clump particles replicated the behaviour of the real pebbles well, the medium and large clump particles were predicted to flow at velocities in excess of twice the real same sized pebbles recorded during the laboratory experiments. These results strongly suggest that: (1) the initial orientation of the particles may play a significant role in the accuracy of the DEM particle flow models. and (2) that the use of inclined gravity model during the loading of the particles into the chute is important to replicate pebble packing orientations produced by the laboratory deposition method.

Good agreement of clearance time versus bite angle was also obtained as Figure 4.20 shows for the CSS of 50mm. When the CSS was decreased to 40mm, similar particle interlock and jamming occurred in both the model simulations and the experiments whenever the bite angle was 18°, 20° or 22°. Figure 4.21 shows a comparison of the side view of the aggregate interlock obtained in the laboratory test and the simulation for a bite angle of 22° and CSS=40mm.

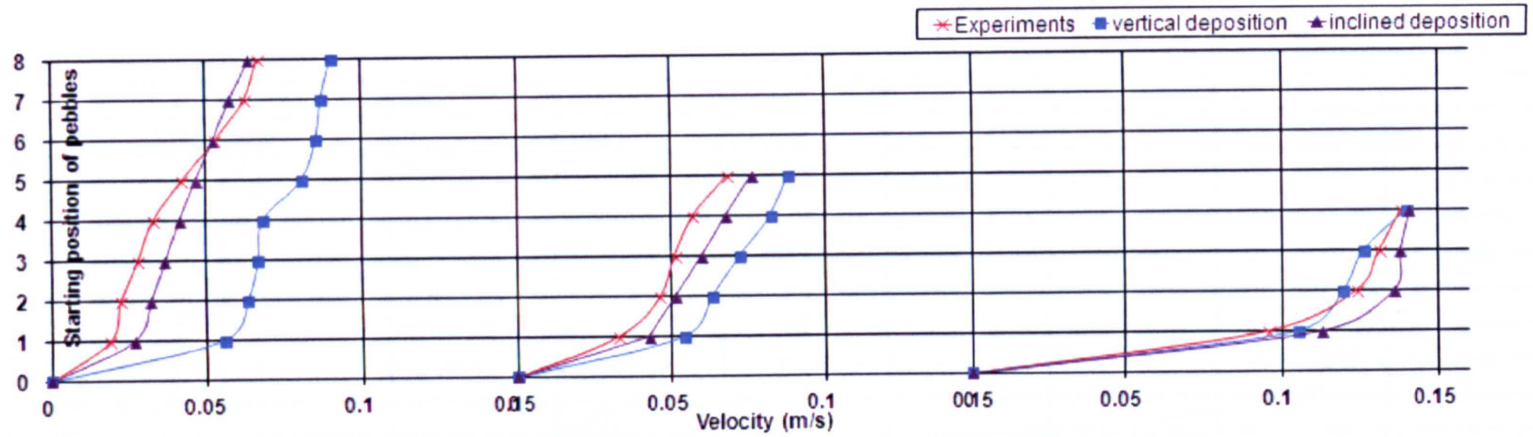
Experiments
vertical deposition
inclined deposition
Starting position of pebbles
Velocity (m/s)
0
1
2
3
4
5
6
7
8
0.05
0.1
0.15

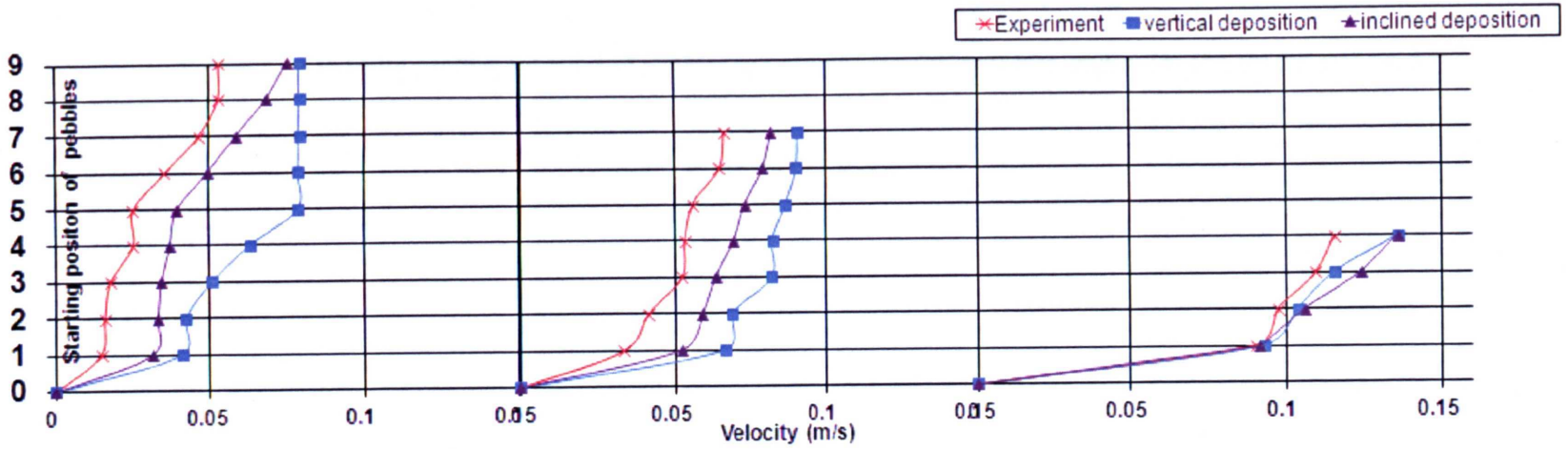
Experiment
vertical deposition
inclined deposition
Starting positon of pebbles
Velocity (m/s)
0
1
2
3
4
5
6
7
8
9
0.05
0.1
0.15

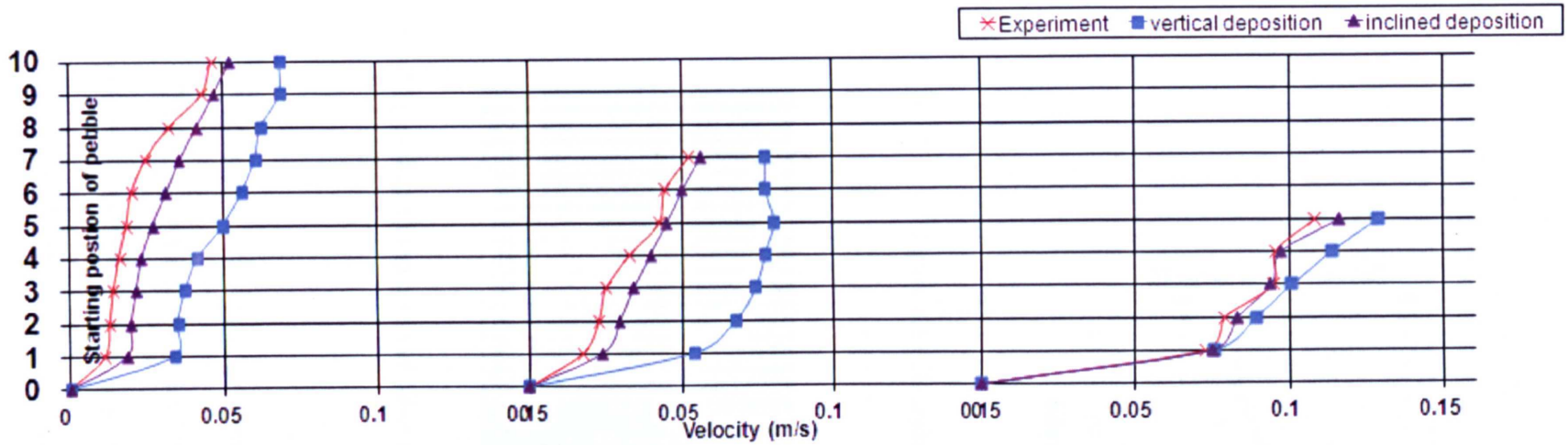

Figure 4.19 Velocity profiles for marked pebbles and clumps for different bite angles: (a) 18°, (b) 20° and (c) 22°

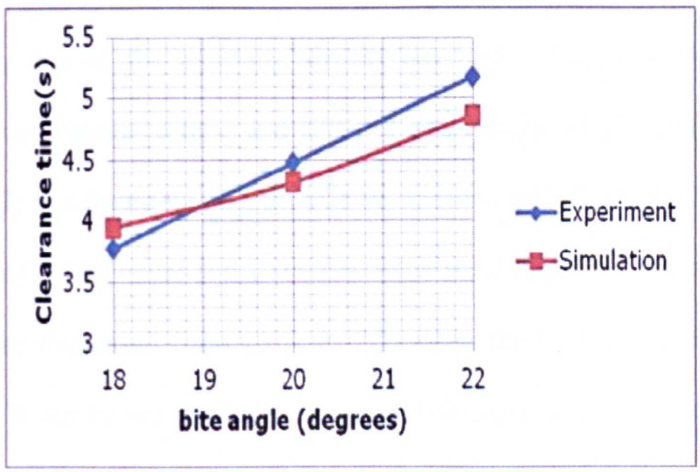

Figure 4.20 Clearance time versus bite angle for CSS=50mm

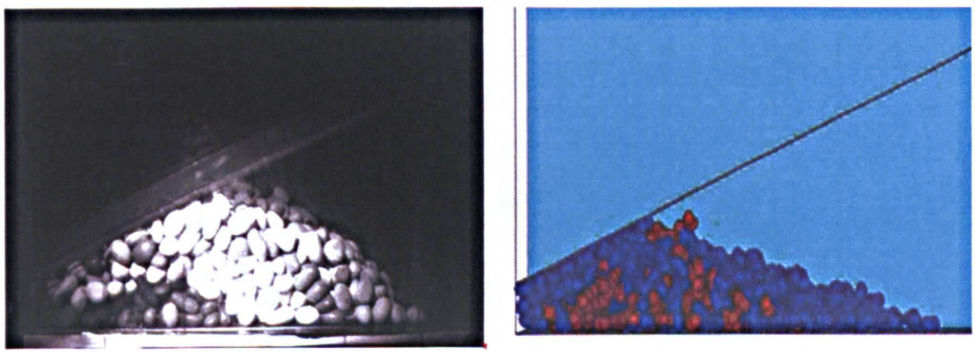

Figure 4.21 Comparison of laboratory experiment and simulation with CSS=40mm and bite angle 22°.

The influence of the chute geometry on the aggregate flows

The DEM model has been used to investigate the relationship between clearance time, bite angle and CSS. This cannot be investigated easily in the lab as the maximum CSS of the rig is 50mm and the maximum bite angle is 22°. Figure 4.22 shows the relationship between clearance time and bite angle for a CSS of 50mm and bite angles

in the range 0-30°. The clearance time increases dramatically with an increasing bite angle. It seems that the clearance time will tend to very large values if the bite angle is increased further, due to the extreme particle interlock. Figure 4.23 shows the relationship between clearance time and CSS for a bite angle of 22° and CSS in the range 30-90mm. It was found that 42mm was the minimum CSS which allows all the pebbles to flow out of the chute and a smaller value would lead to extreme interlock. The clearance time decreased from 13.2s to 2.5s when the CSS was increased from 42mm to 90mm. It can be seen that the clearance time approaches a minimum value 2.5s for CSS larger than 60mm. It can be concluded that for a constant bite angle, there is a minimum CSS which allows particles to flow and maximum CSS beyond which the clearance time has reached its minimum possible value.

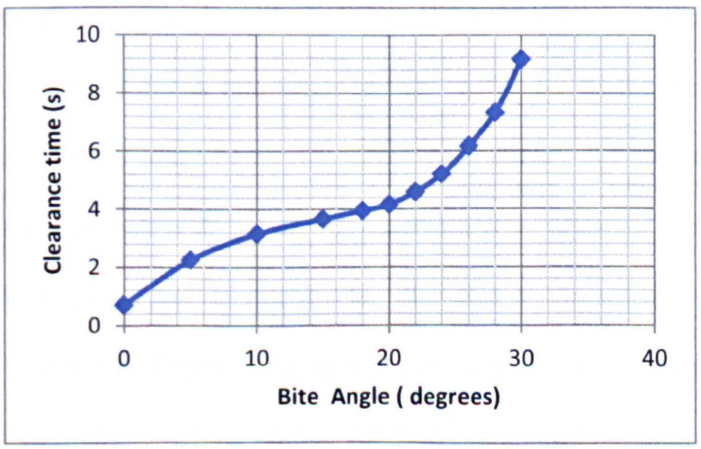

Figure 4.22 . A plot of the DEM model predicted clearance times against chute bite angle for a fixed CSS of 50mm

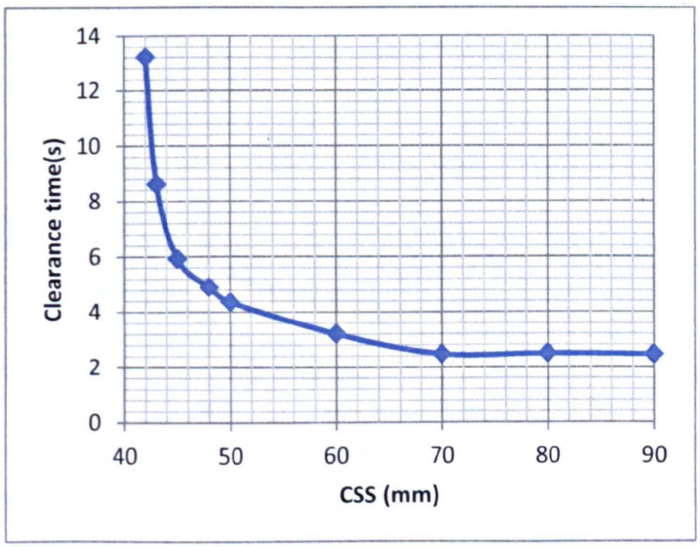

Figure 4.23 Clearance time vs CSS for a bite angle of 22°

To investigate the relationship between the particle size and critical CSS values for flow and minimum clearance time, samples with uniform sized clumps, but different size for each sample, have been studied. Figure 4.23 shows the relationship between clearance time and CSS for a bite angle of 22° and CSS in the range 30-90mm. Clearly the critical CSS values become larger with increasing size of the clumps. Therefore a clump equivalent diameter was determined by equating the volume of the clump to that of a sphere and calculating the diameter of the sphere. The clearance time was then plotted in Figure 4.23 as a function of the CSS normalized by the pebble equivalent diameter and a unique relationship obtained. It can therefore be concluded from Figure 4.24 that the for a bite angle of 22°, the pebbles start to flow for a CSS to equivalent diameter ratio greater than 2.2, and cannot achieve a faster clearance time beyond a CSS to diameter ratio of 4.

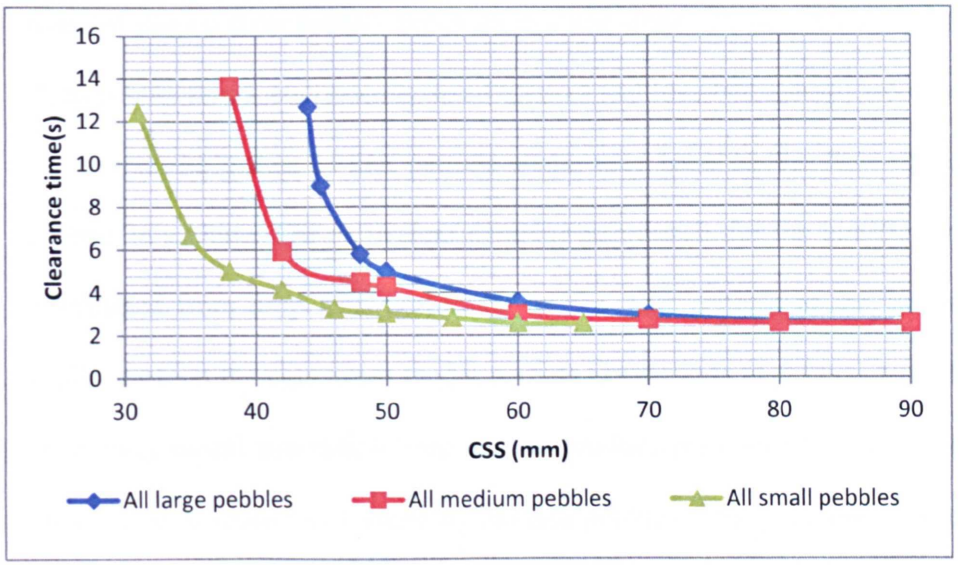

Figure 4.24 Clearance time vs CSS for different pebble sizes for bite angle 22°.

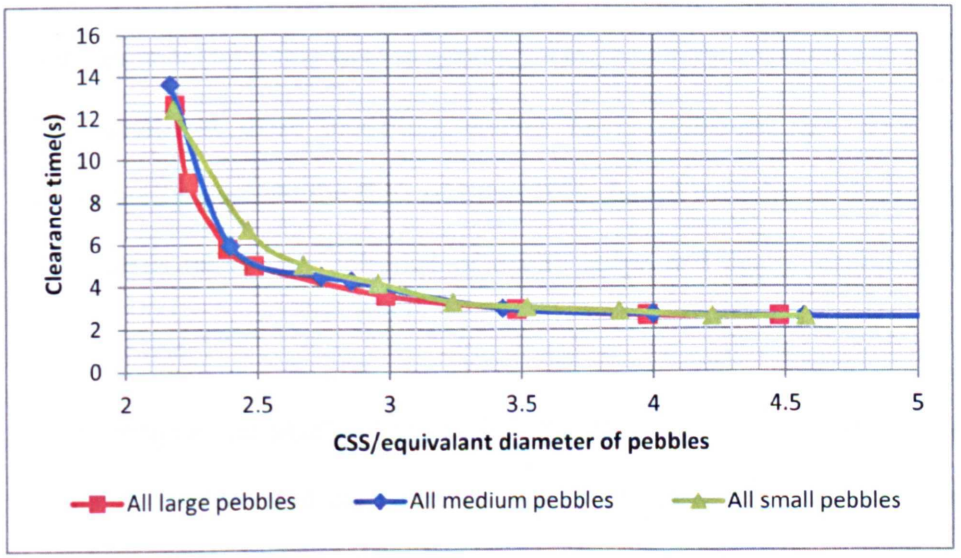

Figure 4.25 Clearance time vs CSS normalized by pebble equivalent diameter.

4.4 Summary

The idealised flow of rocks in a cone crusher in the absence of material breakage has been investigated by performing a series of laboratory experiments of the flow of rounded shaped river pebbles down an inclined chute. To simulate the flow of single sized pebble flows, equivalently sized spheres and four-ball clumps were generated to

rounded shaped river pebbles down an inclined chute. To simulate the flow of single sized pebble flows, equivalently sized spheres and four-ball clumps were generated to investigate the influence that particle shape may have on the flow of single sized pebbles in a chute. The equivalent damping parameters for the particle models were determined from drop tests performed on the river pebbles in the laboratory. In a similar fashion the equivalent model particle coefficients of friction were determined by solving model simulation heap tests to produce parameter values that deliver the same angle of repose as formed by the real pebbles. The computed model solutions for spheres produce poor agreement with the pebble experiments. However, the simulation of the chute flow models using the clumps delivered both velocity profiles and clearance times that were in good agreement with the experimental pebble studies. The results of these modelling studies have confirmed that it is possible to satisfactorily simulate the flow of irregularly shaped particles in three dimensions if due care is taken over selection of clump shape and determination of the correct particle parameters.

To investigate the idealised material flows experienced within a real cone crusher chamber, experimental and computational chute flow models were constructed to replicate the flow of a sequence of single sized model particle zones down the chute. The sizes of the particles within each zone reduce the further the initial position of the zone is down the length of the discharge chute. The descending flow zones attempt to simulate the particle flows created by the crushing processes in a real cone crushing machine. Pebbles of different colours were used for the different sizes and marker pebbles painted so that velocity profiles could be plotted. DEM simulations were used to show that the method of deposition is important, and that velocity profiles for the pebbles in the laboratory can be correctly predicted. The validated model was then

used to examine clearance time as a function of bite angle and closed-size setting (CSS) in addition to the particle size. The simulations show that for a given bite angle, there is a minimum value of CSS normalised by particle size below which flow does not occur, and a maximum value beyond which the clearance time does not reduce. For a bite angle of 22°, the pebbles start to flow for a CSS to particle size ratio greater than 2.2, and cannot achieve a faster clearance time beyond a CSS to particle diameter ratio of 4.

The content contained in this chapter has been published as:

McDowell, G.R., Li, H. and Lowndes, I. (2011) The importance of particle shape in discrete element modelling of particle flow in a chute. *Geotechnique Letters* 1, No. 3, 59-64.

Li, H., McDowell, G.R. and Lowndes, I. (2012) A laboratory investigation and discrete element modelling of rock flow in a chute. *Powder Technology* 229, 199-205.

CHAPTER 5 DISCRETE ELEMENT MODELLING OF ROCK BREAKAGE

5.1 Introduction

This chapter describes the execution, analysis and discussion of the results obtained from the physical experimental and DEM model simulation studies performed to characterise the type of rock breakage events that occur in a cone crusher chamber. There are two common approaches proposed to model particle breakage using DEM: the population balance method (PBM) approach and the bounded particle model (BPM) approach (introduced in section 3.4.3). In the application of the PBM approach, a critical tensile strength σ (Equation 3-5) is used as the breakage criteria to govern particle breakage. For the use of the BPM model, it is also necessary to determine the tensile strength of the modelled rock from laboratory tests to validate the breakage behaviour of the corresponding DEM agglomerate models. The single particle crushing test determines the tensile strength of rock particles by compressing individual particles between two parallel flat platens to induce tensile stresses within the sample. A series of diametrical compression tests of Glensanda ballast particles were performed in the laboratory. The tensile strengths of the ballast particles and the size distribution of the progeny fragments post breakage were analyzed. These results were subsequently used to calibrate the PBM models used to simulate rock breakage in a cone crusher chamber model. This chapter also presents an overview of the formulation and solution of DEM agglomerate models used to simulate the breakage

of a crushed rock particle. A novel algorithm to generate a dense random packing agglomerate is proposed. This type of agglomerate produces a dense and isotropic model rock matrix. This type of agglomerate was subsequently used in the BPM cone crusher model.

5.2 Experiments procedure

A Zwick experimental compression rig similar to that described by Lim (2004) was employed to apply a variable compressive load to the rock samples tested. A photograph of the test cell is shown in Figure 5.1. The rig is instrumented to measure the rate of deformation against the applied load. The main assumption in this test is that the failure of ballast particles is caused by the generation of a continuous stress field within a homogeneous and isotropic particle. It is also assumed that all of the tested rock particles are geometrically similar, and that the contact area of the ballast particle with the confining platens is small (ideally, spherical particle shapes would minimise this contact area). Shipway and Hutchings (1993) found that as the contact areas reduce, the proportion of the sphere radius under tension increases. Consequently, under these conditions a bulk rather than surface fracture is more likely to occur. However, in practice, due to the often irregular shape of real ballast particles it is difficult to minimise the ballast particle contact area. Thus, a collection of quasi-spherical Glensanda rock ballast particles were selected for these tests to minimise the contact area and keep consistent particle geometries. It is also noted that a large contact area would occur if the particle was compressed between 'soft' platens that deform plastically. Thus, the platens were made of case-hardened mild steel to minimise the contact area.

Thirty (McDowell, 2001) quasi-spherical particles of Glensanda ballast particles of three sieve size fractions: 14-28mm, 30-37.5mm and 40-60mm were selected. The particles were washed and dried in a drying oven, before being compressed between the two flat platens. The selected rock particles were individually checked to identify any irregular shape to confirm that the contact areas were small and were located at approximately the centres of the particles. Particles failing this selection criteria were rejected. However, it was accepted that it would be difficult to minimise the contact area on the bottom platen as the particle needs to maintain a stable footing when a compression load is applied across the platens. Consequently, only the top contact area could be effectively minimised. In addition, any particles likely to fail under the application of a bending moment were identified and rejected. For example, if a particle is identified to have two or more contact points with the bottom platen (i.e. the particle geometry contains an arch at the bottom), bending moment may potentially be generated that may promote particle fracture.

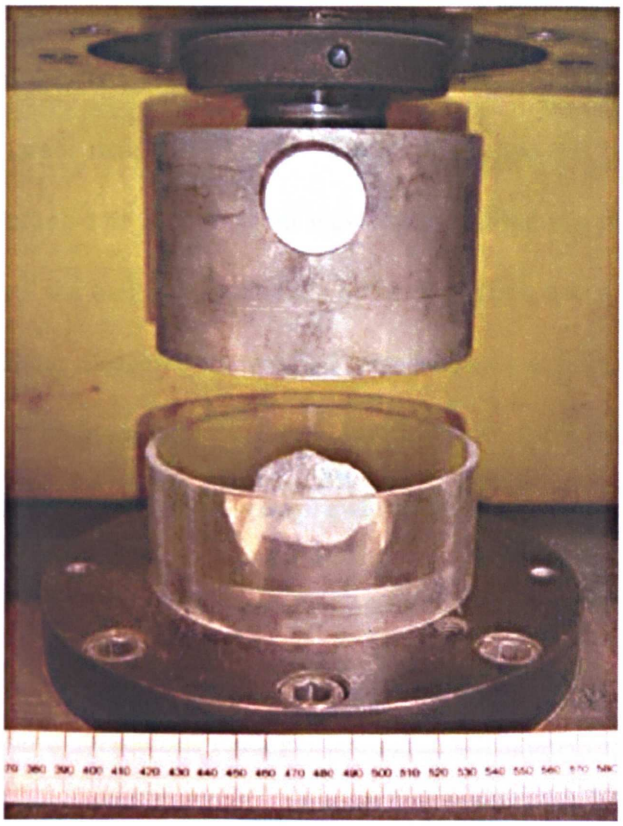

(a)

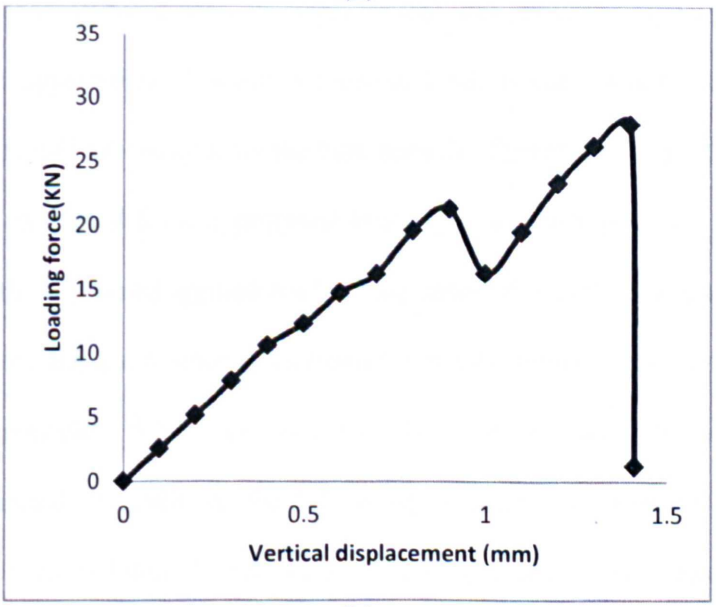

(b)

Figure 5.1 (a)A photograph of the Zwick experimental testing rig used to apply diametrical compression tests to selected rock samples. (b) Typical loading force-displacement curve at loading rate of 1mm/s

Figure 5.1a shows a photograph of the two flat 140 mm diameter, case-hardened mild steel platens attached to the Zwick testing machine. A hollow Perspex cylinder, which is slightly larger than two platens, is used to confine the broken rock fragments. A constant loading rate of 1mm/min was applied to the top plate of the Zwick testing machine until the ballast particle fails by breaking into two or more pieces. The Zwick testing machine measures the applied force and has a gauge attached to the machine which allows displacement to be read visually from a gauge. The force was measured to an accuracy of ±50N and the displacement was read to an accuracy of ±0.05mm.

The loading rate was set at a constant 1mm/min as Lim (2004) had previously found that at high loading velocities, broken fragments could not fall away from the bulk particle under a continuous load, generating an artificially high tensile strength as two or more daughter particles were being compressed instead of the original single parent. Typical loading force-vertical displacement was shown in figure5.1b. Nevertheless, even the application of a low 1mm/min loading rate cannot guarantee that broken fragments will fall away from the bulk particle. Therefore, the particle tested had to be visually examined for any potential breakages, at every occasion there was a sudden drop in the measured applied load. In the cases of uncertainty, the procedure adopted was to stop the test to enable a detailed visual examination of the exposed surfaces of the test particle. Where no intact broken fragments were observed the test process was resumed. In addition, the following criterion was adopted to determine as to whether particle failure had occurred following a drop in the measured load: a drop in load corresponded to particle failure. If the total volume of any broken fragments accounted for more than 1/3 of the original particle volume, then the particle was deemed to have failed. The corresponding peak load was used to compute the tensile strength for the tested rock sample.

5.3 Analysis and discussion of the experimental results

5.3.1 Measured distribution of particle strengths

Section 3.4.2 presented a review of the methods that may be used to measure the tensile stress at failure for a particle. It was established that the tensile strength of a particle subjected to a diametrical compression under a low loading rate, is determined from the evaluation of the following expression:

$$\sigma = \frac{F}{d^2} \qquad \textbf{Equation 5-1}$$

where, F, is the measured failure (peak) force and, d, is the distance between to platens at failure. The tensile stresses measures for each set of tests were ranked in ascending order to compute the survival probability for each tensile stress at failure. Following Davidge (1979), the survival probability is computed using the mean rank position equation:

$$P_s = 1 - i/(N+1) \qquad \textbf{Equation 5-2}$$

where i is the ith ranked sample from a total of N samples. Thus, given the test results for 30 same sized particles, the lowest value of σ gives a particle survival probability of 30/31, and the tensile strength of the strongest particle gives a particle survival probability of 1/31.

Weibull (1951) statistics was used to quantify the ballast tensile strength and determine the variation in the strengths measured from each batch of particle tests. Consequently, the survival probability of particles of size d under a tensile stress σ is given by:

$$P_s(d) = \exp(-(\frac{\sigma}{\sigma_o})^m)$$ **Equation 5-3**

where m is the Weibull modulus and σ_o is the tensile stress such that 37% of the particles survive, commonly termed the '37% tensile strength' of the sample. The Weibull modulus determines the coefficient of variation, which reduces with as the variability in strength increases (see section 3.4.2). Equation 5-3 may be recast in the form:

$$ln\left[ln\left(\frac{1}{P_s(d)}\right)\right] = m\, ln(\frac{\sigma}{\sigma_o})$$ **Equation 5-4**

The Weibull modulus m and the 37% tensile strength for each set of tests may be graphically determined from a Weibull survival probability plot, which is a plot of $ln(ln(1/p_s))$ against $ln\sigma$. The Weibull modulus m corresponds to the slope of the line of best fit, and the value of $\sigma_o$is the value of σ when $ln(l\,n\left(\frac{1}{p_s}\right) = 0$. The Weibull probability of plots for the three tested size fractions of ballast particles are plotted in Figures 5.2-5.5.

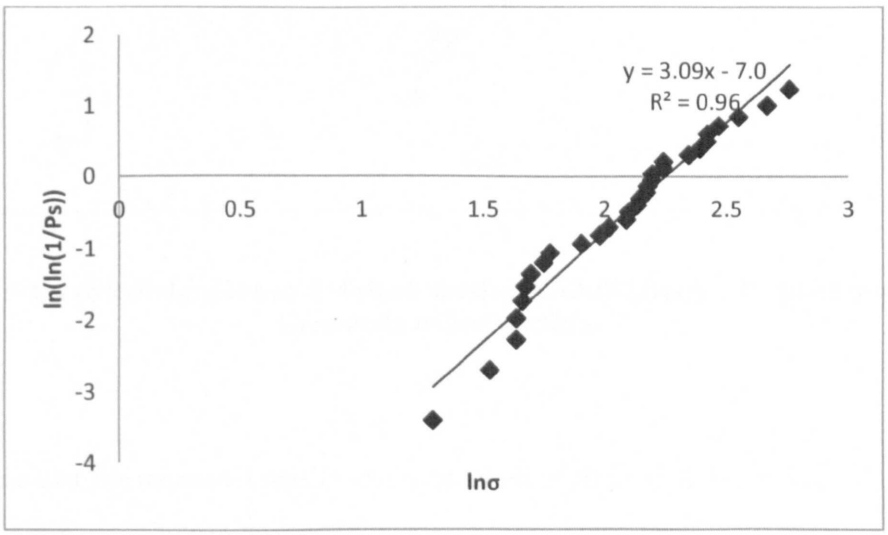

Figure 5.2 A plot of the computed Weibull survival probabilities for the 40-60 mm sized Glensanda ballast particles

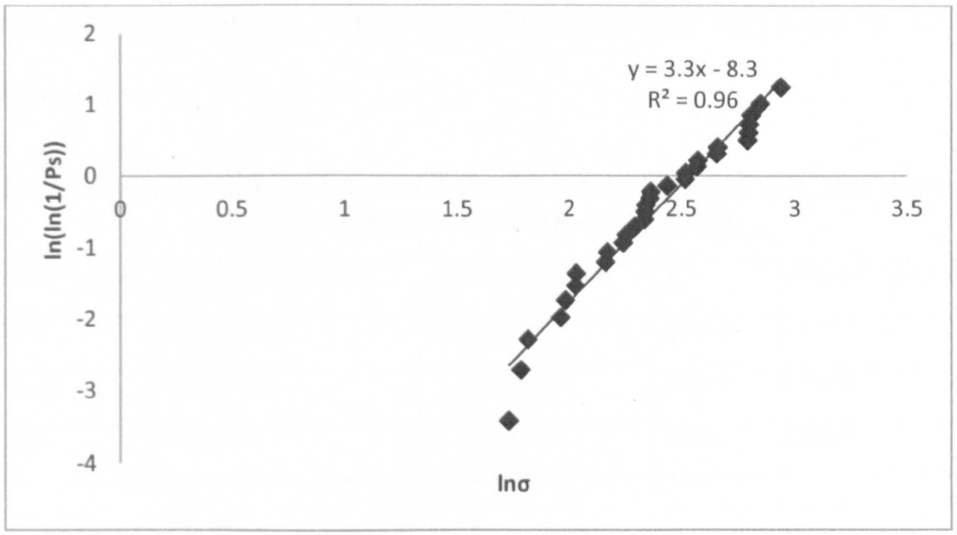

Figure 5.3 A plot of the computed Weibull survival probabilities for the 30-37.5 mm sized Glensanda ballast particles

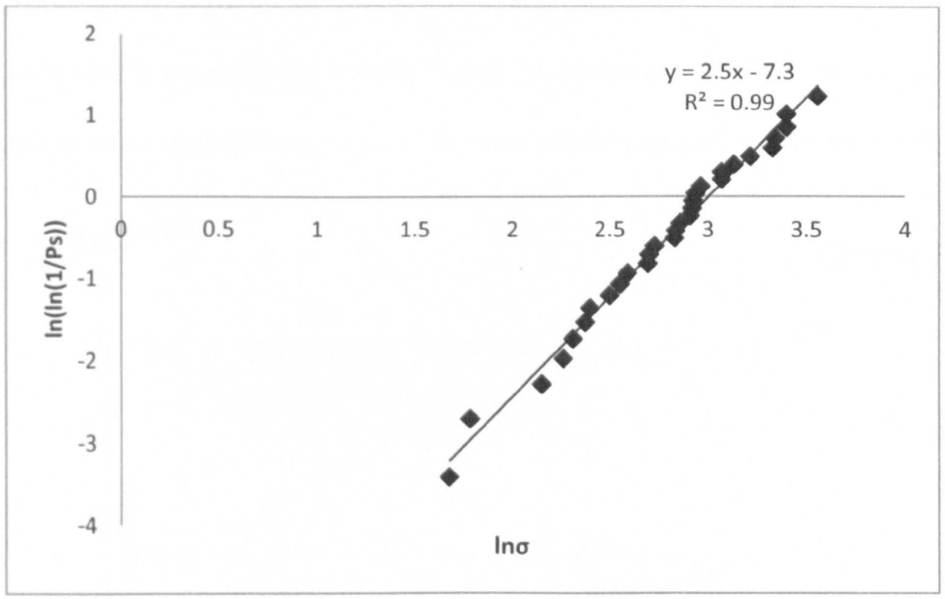

Figure 5.4 A plot of the computed Weibull survival probabilities for the 14-28 mm sized Glensanda ballast particles

It is clear that the measured tensile strengths of all of three tested size fractions of the ballast exhibit a Weibull distribution Table 5.1 shows summary of the measured experimental data for all three size fractions: the 37% tensile strength (σ_o), the

average tensile strength (σ_f), correlation coefficient of linear fit(R^2), and the Weibull modulus (m).

Table 5.1 Summary of the averages of the measured experimental data obtained from the sets of single sized particle crushing tests

Particle size fraction	37% tensile strength σ_o	Average strength σ_f	R^2	Weibull Modulus m
14-28mm	20.12MPa	20.02MPa	0.9608	3.0895
30-37.5mm	12.61MPa	11.26MPa	0.9644	3.2859
40-60mm	9.49MPa	8.47MPa	0.9882	2.4398

5.3.2 Size effect on particle strength

An examination of the experimental data sets presented in Table 5.1 concludes that the smaller ballast particles are stronger than larger particles which are consistent with the Lee's (1992) experimental results. Figure 5.6 shows a plot of the average particle strength as a function the particle size. The data can be expressed as the equation:

$$\sigma_{av} = 480.03d^{-1.1}$$ **Equation 5-5**

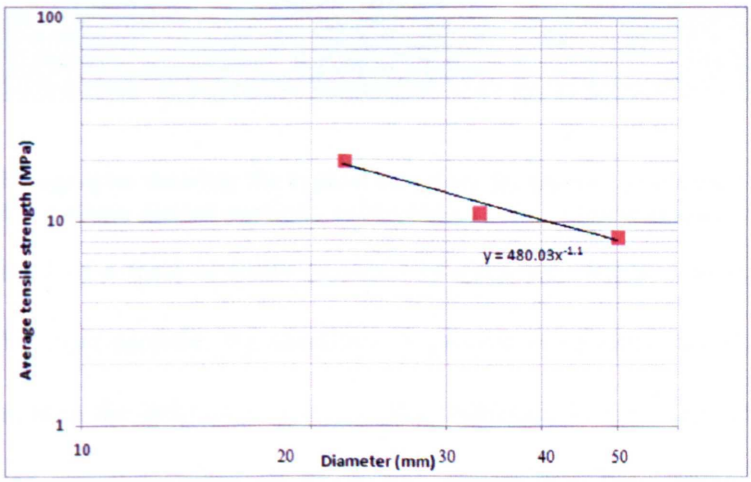

Figure 5.5 Average tensile strength against average particle size at failure

The size effect factor b in Equation 3-9 corresponds to -1.1 here. The average Weibull modulus m_{av} of three size fractions of particles is 2.9 so that the size factor b approximately equals $-m_{av}/3$. This compares favourably with Equation 3-10 proposed by McDowell and Bolton (1998).

5.3.3 Size distribution of fragments

To select an appropriate breakage function for the construction of a PBM model to simulate the breakage behaviour experienced in a cone crusher chamber model, the size distribution of the daughter fragments resulting from the failure of the single parent particles were analysed. Figure 5.6 shows the typical fragments generated following the failure of the single particles. As may be observed, the failed particles typically formed 2 or 3 larger sized progeny particles accompanied by a few smaller sized particles and some fines.

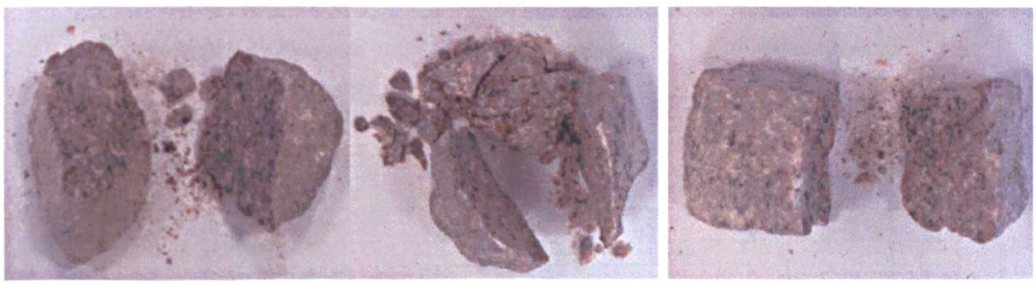

Figure 5.6 Photographs showing the typical daughter fragments produced following the failure of the single parent particles subjected to a diametrical compression test

Twenty particles of a total of thirty particles of each size fraction were sieved. For each original parent particle, the daughter fragments were sized according to their sieve size and then the individual size fractions individually weighed. The minimum sieve size used was 8mm, thus all fragments smaller than 8mm were classified as fines. The results of this size classification analyses are graphically presented on figures 5.7-5.9.

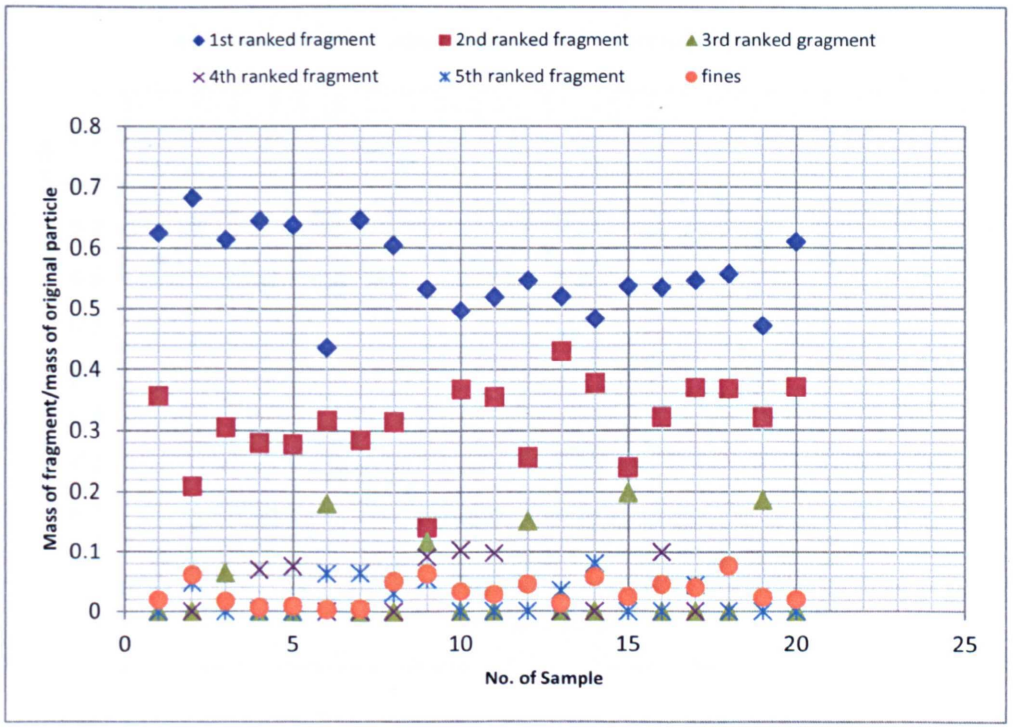

Figure 5.7 A graphical presentation of the size and mass classification data obtained from analyses performed on the fragments produced on the failure of the 40-60 mm particles subjected to a diametrical compression test

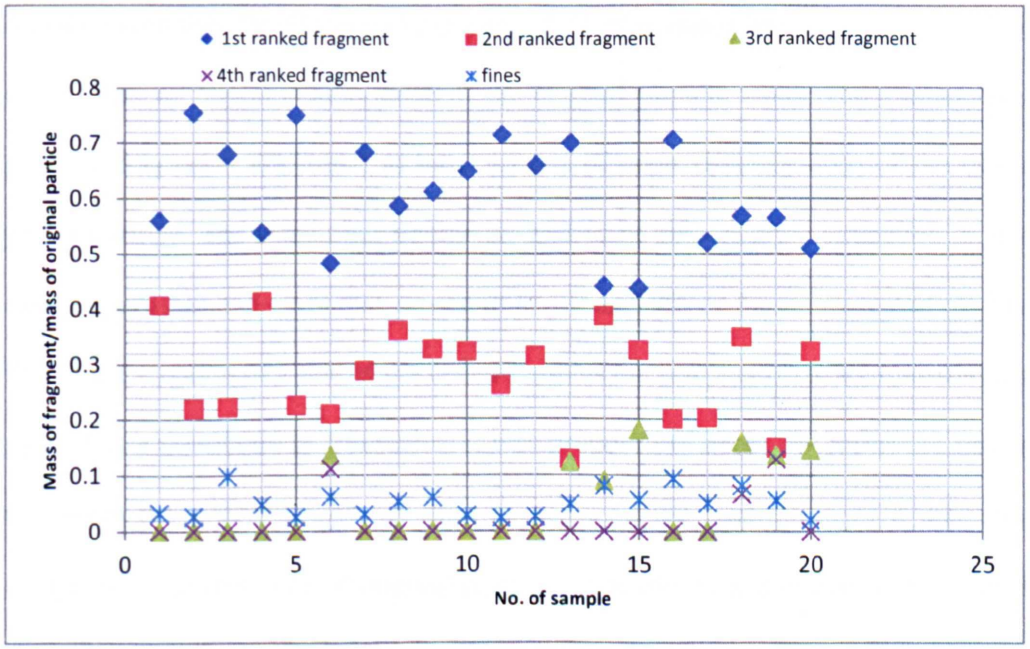

Figure 5.8 A graphical presentation of the size and mass classification data obtained from analyses performed on the fragments produced on the failure of the 30-37.5 mm sized particles subjected to a diametrical compression test

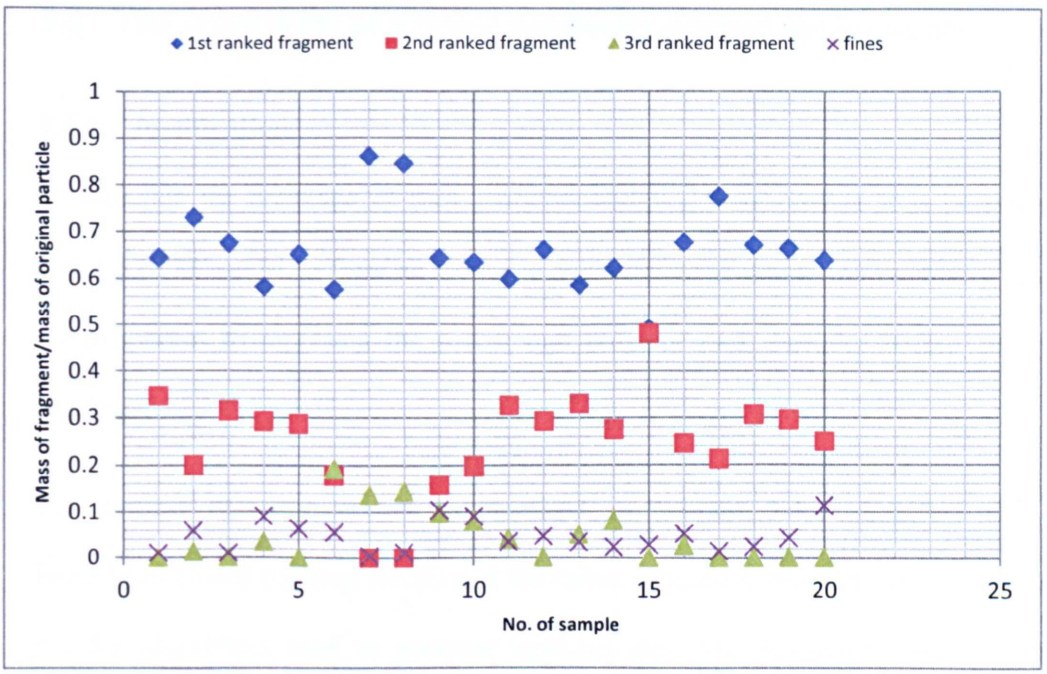

Figure 5.9 A graphical presentation of the size and mass classification data obtained from analyses performed on the rock fragments produced on the failure of the 14-28 mm particles subjected to a diametrical compression test

It can be seen that for all the size fractions, the largest daughter fragments can in most cases takes up approximately 60% of the original particle mass. The second largest progeny fragments are found to have a mass of approximately 30% of the original parent particle. The remaining fragments tend to be formed by a collection of much smaller particles and fines that represent less than 10% of the original particle mass. With the exception of a few of the tested samples the progeny particles followed these general size distributions. Therefore, it was proposed to adopt the following protocol to govern the generation of daughter particles on the application of a diametrical compression to each size of original particle: once the critical tensile strength of this size of particle is exceeded, the particle will always divide into two major particles which will be 60% and 30% of the original particle mass, with the remaining mass (10%) reporting as crushed fines (< 8mm).

5.4 The generation of a dense randomly packed agglomerate

5.4.1 Justification

To simulate the breakage of rock particles within a cone crusher it is proposed to adopt a BPM model to form an isotropic agglomerate of dense and randomly packed micro-spheres to represent the parent and progeny rock particles before and after breakage.

The critical literature review summarised in Section 3.4.2 identified that the Hexagonal closed packing (HCP) and the radius expansion methods are the two most popular algorithms used to generate agglomerates. The hexagonal closed packing (HCP) agglomerate (Fig 5.10a-b) has been chosen by many researchers, to investigate the fracture of soil grains (Robertson and Bolton, 2001), sand particles (Cheng, Nakata and Bolton, 2003; McDowell and Harireche, 2002a; 2002b) and ballast (Lim and McDowell, 2007; Lim et al, 2004). In Figure 5.10, the A-B-A-B layering sequence for hexagonal closed packing is propagating in the y-direction, shown as Figure 5.10(b). The HCP agglomerate is useful because it can provide the theoretically densest packing (a porosity of 0.26) for uniformly sized spheres bonded to simulate a solid particle. This density is achieved without requiring any particle overlap, which would result in locked-in forces inside the bonded agglomerate. In addition, the HCP method produces a regular and anisotropic packing, (shown in Figure 5.10a-b). If the HCP agglomerate is rotated through 90° in the x-y plane (Figure 5.10a) during diametrical compression, the contact chains between the two crushing plates will change as shown in Fig 5.10b-c. As the force chains will, in general mirror the contact orientations, the force chains will also change. Figure 5.11 shows the effect of rotation angle on the tensile strength of a spherical HCP

agglomerate. The rotation angle is as shown in figure 5.10(a). The diameter of each agglomerate is 42 mm and other input micro parameters of the agglomerate are listed in Table 5.2. A physical description of each parameter can be found in Chapter 2. The maximum tensile strength of 18.1MPa is more than twice the minimum tensile strength 8.1MPa as the rotation angle is increased from 0 to 90 degrees.

The radius expansion method introduced by Lubachevsky and Stillinger (1999) is another conventional method of forming a random packing agglomerate. This method was introduced in section 3.4.3. This type of agglomerate has been used to investigate the behaviour of materials such as sand particles (Cil and Alshibli, 2012) and rocks (Potyondy & Cundall, 2004). However, as the agglomerate is too porous, progressive fracture of small parts of the agglomerate can occur, which produces a significant load reduction and multiple peaks in some simulations (Cil and Alshibli, 2012), as opposed to well defined bulk fracture into 2 or 3 fragments with a single peak in the load-deflection curve. In addition, large internal voids become external voids when crushing occurs and Lim & McDowell (2007) showed that for uniform micro-spheres bonded to make an agglomerate, a minimum number of 500 micro-spheres were required to eliminate co-ordination number effects due to a large proportion of surface particles.

A novel algorithm is proposed to generate a dense, isotropic rock particle model with negligible initial overlap by inserting particles to fill the voids in the agglomerate. The concept of space filling using spheres of different sizes has been used by Schopfer et. al. (2009) to study confined triaxial extension and compression tests. They generated samples with different particle packing methods, characterised by differing particle size distributions and porosities. They iteratively inserted particles in the existing voids

to achieve four contacts. The contribution here is to solve the problem analytically and determine for each void, where each new sphere should be created and its size, such that smaller and smaller particles are inserted in the remaining voids, to achieve a dense packing.

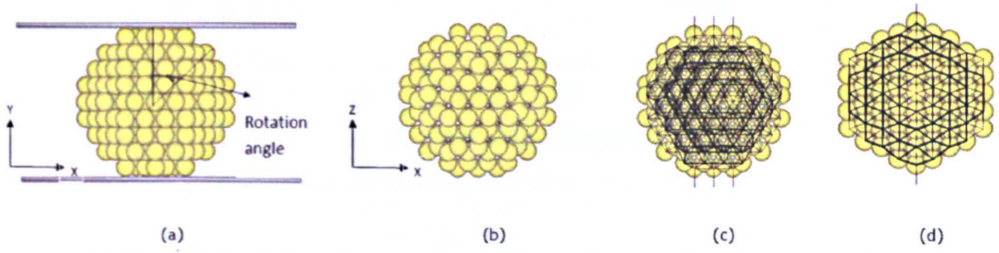

Figure 5.10 (a) the orientation of 3D hexagonal closed packing agglomerate under diametrical compression between two parallel platens, (b) orientation of the 3D hexagonal closed packing agglomerate projected in the x-z plane (c) distribution of the model contacts for a rotation angle of 0° in the x-y plane and (d) distribution of the model contacts for a rotation angle of 90° in the x-y plane

Table 5.2 Input parameter of the agglomerate in DEM diametral compression tests

Parameter	values
Diameter of agglomerate	42mm or 50mm
wall stiffness	$1*10^9$ N/m
wall velocity	0.008m/s
ball radius	0.0025m
ball density	2700 kg/m^3
friction coefficient	0.5
Shear Modulus	70GPa
Poisson's ratio	0.2
parallel bond radius multiplier	1
parallel bond normal stiffness	$5*10^{12}$ N/m
parallel bond shear stiffness	$2*10^{12}$ N/m
normal/shear bond strength	60MPa

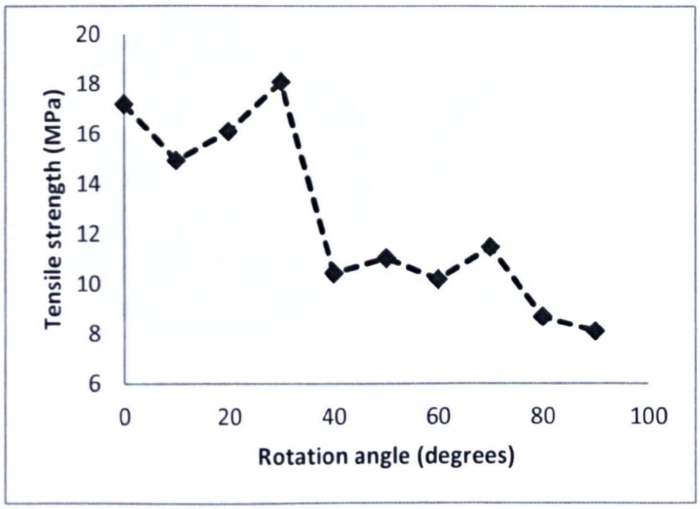

Figure 5.11 The effect of that the rotation angle in the x-y plane has on the computed tensile strength for the spherical HCP agglomerate.

5.4.2 Modelling of an agglomerate

The contact model used in this study is the Hertzian contact model, described in section 2.5.2. The objective of the proposed method is to place spheres of varying sizes in the voids of a sample formed from a relatively loose random packing of uniformly sized spheres. To create the relatively loose random packing, a specific number of spheres with uniform radius r_{max} are generated within a spherical wall and then a servo-controlled velocity is applied to the spherical wall until the spheres touch one another and the wall (Figure 5.12a-5.12b), which means expanding or contracting the spherical wall to achieve a target pressure. The target pressure here was set as 100KPa. An increasing target pressure will resulted in larger initial overlaps between the spheres.

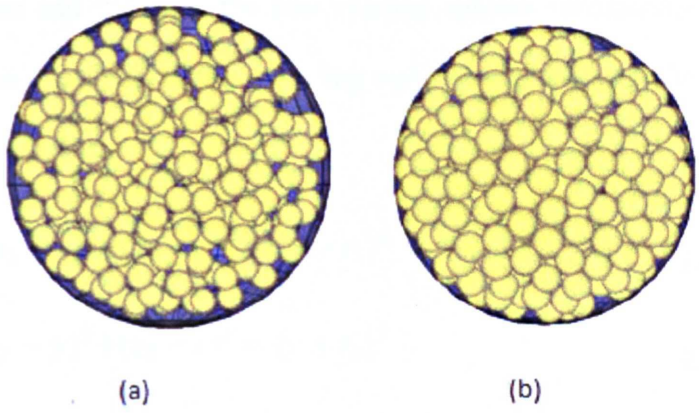

Figure 5.12 A figure showing animation stills that illustrate the generation of a dense packing achieved by a reduction in the boundary wall diameter, which represents an increase in the target pressure.

Fill procedure

Ideally, the introduction of each new smaller micro-sphere into the voids should make contact with its four neighbouring spheres, as shown in figure 5.13. The following procedure was introduced to identify the four neighbouring spheres

- Randomly select a sphere as the first sphere;
- Find all the spheres whose centres lie inside the sphere domain with centre at O and radius equal to *d*. O is the centre of the first ball and d is twice the diameter of the initial uniformly-sized spheres;
- Select any three balls as a group from the spheres found in previous step; calculate the volume of the tetrahedron created by the centres of these three spheres and the first sphere. The group which gives a minimum volume for the tetrahedron is selected as the neighbouring three spheres of the first ball;
- Repeat until every ball has three neighbouring spheres.

As the positions and radius of the four existing spheres surrounding the void are known, it is possible to solve the following equations to calculate the position and radius of the added ball.

$$(x_1 - x)^2 + (y_1 - y)^2 + (z_1 - z)^2 = (r + r_1)^2 \quad \textbf{Equation 5-6}$$

$$(x_2 - x)^2 + (y_2 - y)^2 + (z_2 - z)^2 = (r + r_2)^2 \quad \textbf{Equation 5-7}$$

$$(x_3 - x)^2 + (y_3 - y)^2 + (z_3 - z)^2 = (r + r_3)^2 \quad \textbf{Equation 5-8}$$

$$(x_4 - x)^2 + (y_4 - y)^2 + (z_4 - z)^2 = (r + r_4)^2 \quad \textbf{Equation 5-9}$$

where x, y, z and r denote the co-ordinates of the centre and radius of the new ball, and those with subscripts 1,2,3 and 4 represent the co-ordinates of the centres and radii of the four existing spheres. Three equations in x, y ,z and r can be derived by subtracting equation (5-6) from equations (5-7)-(5-9). These three equations can be written in matrix form in equation (5-10):

$$\begin{bmatrix} 2(x_2 - x_1) & 2(y_2 - y_1) & 2(z_2 - z_1) \\ 2(x_3 - x_1) & 2(y_3 - y_1) & 2(z_3 - z_1) \\ 2(x_4 - x_1) & 2(y_4 - y_1) & 2(z_4 - z_1) \end{bmatrix} \begin{bmatrix} x \\ y \\ z \end{bmatrix}$$

$$= \begin{bmatrix} 2r(r_1 - r_2) + (x_2^2 + y_2^2 + z_2^2 - r_2^2) - (x_1^2 + y_1^2 + z_1^2 - r_1^2) \\ 2r(r_1 - r_3) + (x_3^2 + y_3^2 + z_3^2 - r_3^2) - (x_1^2 + y_1^2 + z_1^2 - r_1^2) \\ 2r(r_1 - r_4) + (x_4^2 + y_4^2 + z_4^2 - r_4^2) - (x_1^2 + y_1^2 + z_1^2 - r_1^2) \end{bmatrix} \quad \textbf{Equation 5-10}$$

The above matrices may be solved using a suitably adapted Matlab™ code. The derived (x,y,z) co-ordinates of the new micro-sphere to be added may be written in terms of a function of its radius r. The three equations can then be substituted into equation (5-6), and an equation in r obtained and solved (except for the case when the packing void.

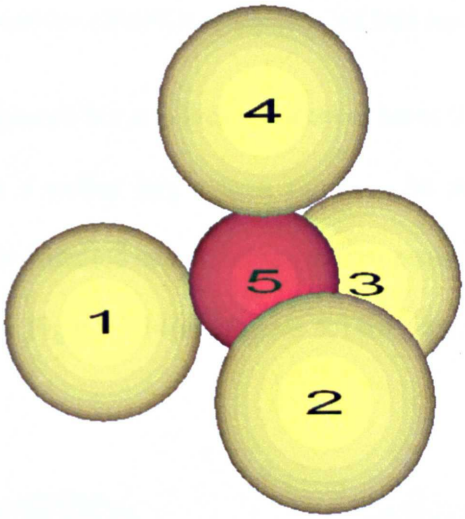

Figure 5.13 The location of the new ball to occupy the tetrahedral space between four existing micro-spheres forming the agglomerate packing.

New micro-spheres filter

Two necessary conditions need to be met by the newly added micro-spheres:

- Each new ball must be larger than the defined minimum size of radius $r_{min.}$
- No overlap can occur with any other existing surrounding spheres

If the derived new ball does not meet the first condition, it is rejected. If both conditions are satisfied, then the ball is generated as located. For each new ball meeting condition 1 but not condition 2, a new ball is formed at the calculated position but with a radius, r_{min}. This ball has less than three contacts at this stage. Therefore it is then expanded according to the following procedure:

- Enlarge the radius of this ball in increments of 0.1% (this can be set to be smaller to get a smaller initial overlap) and then release it with the condition that all other spheres were fixed.

- Repeat this procedure until the newly located ball has at least three contacts.

This method is then repeated for any four adjacent spheres to create new spheres until no more spheres with a radius larger than r_{min} may be added. Once this point is reached the process is terminated as the dense random packing agglomerate is deemed complete. as shown by Figure 5.14(a). Figure 5.14(b) shows only the newly added micro-spheres.

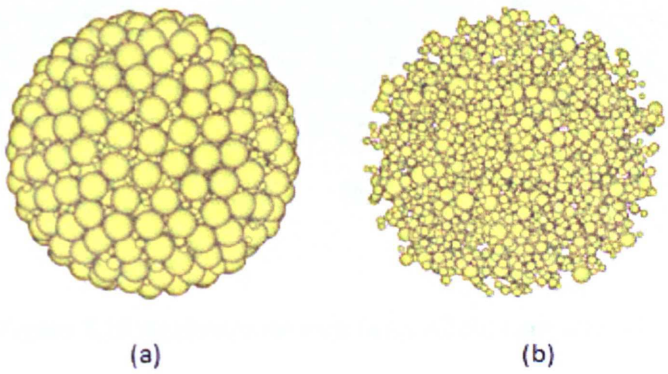

Figure 5.14 (a) Final form of a generated dense randomly packed agglomerate of a sphere, and (b) a view of only the new micro-spheres subsequently generated and added to the dismissingly sized voids in packing until the packing becomes sufficiently dense. .

5.4.3 Effect of agglomerate packing density

The packing density is governed by the ratio r_0 of the radii of the largest and smallest spheres, r_{max} and r_{min} respectively:

$$r_o = \frac{r_{max}}{r_{min}} \qquad \textbf{Equation 5-11}$$

Thus, the agglomerate is an assembly of uniform spheres when r_0=1. The radius ratio r_0 determines the number of small spheres in the agglomerate. Figure 5.15a-c shows a plan view of the agglomerate with r_0 equal to 2, 3 and 4, respectively. Figure 5.16 shows the porosity and coordination number (average number of contacts per ball) of

the agglomerate as a function of the radius ratio. It can be seen that the coordination number approaches six as r_o increases to a value of 4. The porosity clearly reduces as r_o increases; for the agglomerate with r_o=4, the porosity has decreased to 0.31 compared to a porosity of 0.45 for the monodisperse agglomerate.

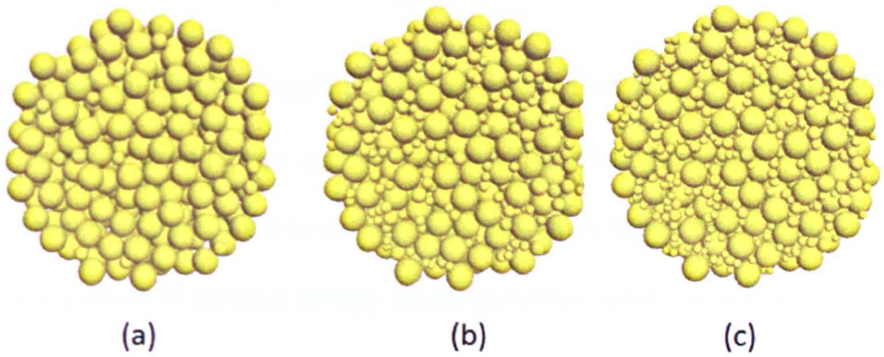

Figure 5.15 Agglomerate with (a) r_o =2 (b) r_o=3 (c) r_o=4.

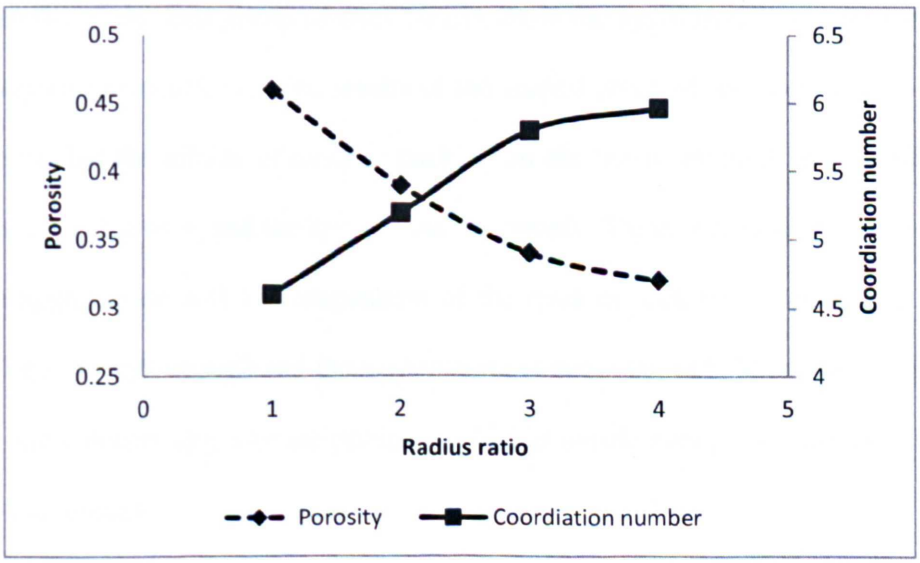

Figure 5.16 A comparative plot of the computed porosity and coordination numbers for a range of radius ratio values, r_o

To investigate the effect of packing density on the tensile strength of the agglomerate, two groups of diametrical compression tests were conducted:

1) The same agglomerate with a random orientation: 20 tests at random orientations for each agglomerate with each radius ratio of 2, 3 and 4, to investigate the effect of packing density on the isotropy of the agglomerate.

2) Twenty tests on different agglomerates for each value of r_o: that is to say that for r_o=2, for example, 20 different agglomerates (a different random number seed is used to generate each sample) were tested, and this procedure repeated for each value of r_o – to study the effect of packing density on the statistical variation in strength.

The micro parameters for each agglomerate are all the same, with a diameter of 50mm and other input parameters as listed in Table 5.2. The mean values of tensile strength, standard deviation and coefficients of variation for the 20 tests are listed in Table 5.3. The results of the first group of tests clearly show the agglomerate is more isotropic for a higher radius ratio r_o. The results of the second group of test presented in Table 5.3 show that the effects of random packing on the tensile strength are smaller, the greater the value of r_o and the less porous the sample. These results show the strength of the agglomerate will be independent of the random packing or orientation if the value of r_o is high enough and the agglomerate is dense enough. Moreover, both tests show that a denser agglomerate produces a higher tensile strength for the same set of micro parameters.

Table 5.3 Effect of radius ratio r_0 on agglomerate tensile strength

	radius ratio r_o	mean /MPa	standard deviation/MPa	coefficient of variation
Test 1: effect of orientation	4	9.42	0.44	0.05
	3	7.69	1.02	0.13
	2	3.95	0.82	0.21
	radius ratio r_o	mean/Mpa	standard deviation/MPa	coefficient of variation
Test 2: effect of packing	4	9.36	0.49	0.05
	3	7.90	0.94	0.12
	2	3.99	1.09	0.27

The packing density also affects the fracture pattern. Figure 5.17 shows a typical fracture of the agglomerate for each radius ratio and corresponding load-displacement relationship. The lines plotted on the agglomerate represent the intact bonds after breakage. For a loose agglomerate of r_o=2, the typical fracture is a multiple asperity fracture and multiple peaks occur in the load-displacement curve before the final fracture of the agglomerate (in some agglomerates fast bulk fracture does occur). The probability of this type of multiple asperity fracture is reduced by increasing the packing density of the agglomerate by increasing the radius ratio r_o. A clearer and more realistic fast bulk fracture is seen as r_o increases, which compares well with laboratory tests performed on rocks (Hiramatsu and Oka, 1966). For r_o=4, there is only one significant load reduction observed on the simulated load-displacement curve that is more representative of real rock breakage (Lee, 1992).

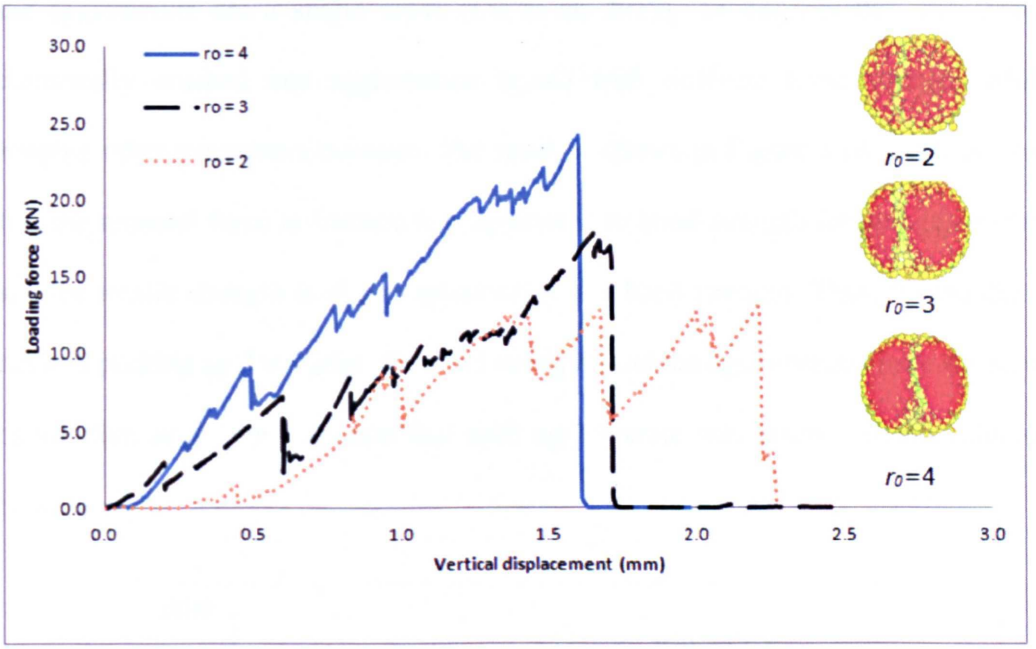

Figure 5.17 The effect of radius ratio on load-displacement relationship and fracture pattern.

The content contained in the section 5.1-5.3 has been published in *Géotechnique Letters:*

Li, H., McDowell, G.R. and Lowndes, I. (2013) Discrete element modelling of rock breakage using dense random packing agglomerates. *Géotechnique Letters 3*, No. July-September (2013): 98-102.

5.4.4 Modelling tensile strength variation

Table 5.3 shows that, for a dense random packing agglomerate of significantly high density, there is minor effect on the strength of agglomerate by changing the loading orientation. Therefore one would expect the strength of the agglomerate to be proportional to the bond strength under the condition that the bond strengths inside

the agglomerate are a single value (Cil et al, 2013). To confirm this, the author diametrally crushed one agglomerate (r_o=4) with different bond strength while keeping other parameters constant. The result is shown in Figure 5.18 and it is clear that the nominal force at fracture is proportional to bond strength for an agglomerate and the tensile strength is also proportional to the bond strength. Thus, for the dense random packing agglomerates, the bond strengths and the agglomerates have the same distribution under the condition that each agglomerate was given a single value of bond strength.

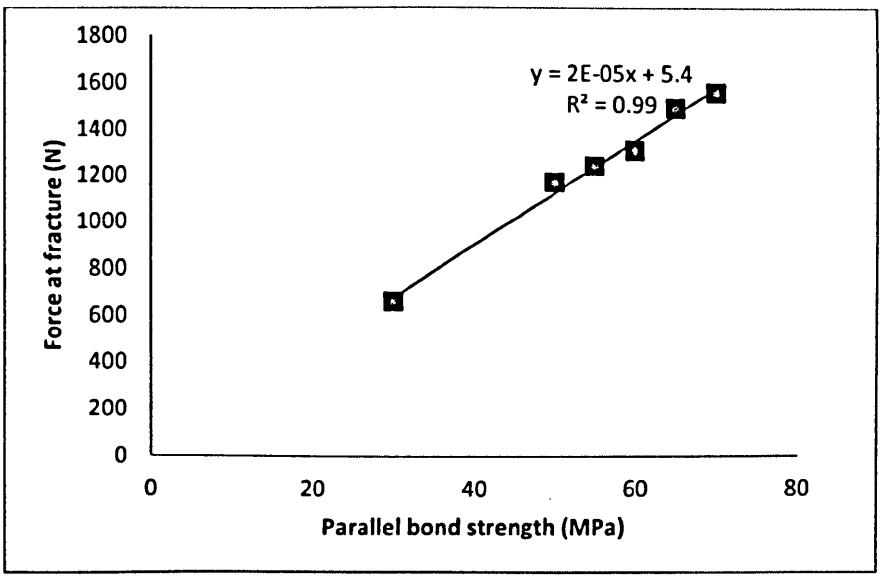

Figure 5.18 A plot of the computed force at fracture as a function of parallel bond strength

Therefore, the modelling of the variation in particle strengths can be achieved by simply giving each agglomerate a single value of bond strength which is taken from the relevant distribution of the experimental results. For example, to model the experimental result of 40-60mm particles, the experimental result of the tensile strength follows a Weibull distribution with 37% survival value 9.48MPa and Weibull

modulus 3.09. Therefore the bond strengths of 30 agglomerates were taken from a Weibull distribution with modulus 3.09. The 37% bond strength value B_o was determined so as to achieve the same 37% survive tensile strength of the agglomerate (σ_0) as that in experiments. The calibration procedure was as follows:

- The Young's modulus was chosen with a Poisson ratio of 0.2, to give an initial elastic response which matched the experiments.
- The agglomerate was given a random bond strength, assuming a Weibull modulus equal to that for the Weibull distribution of particle strengths in the experiments.
- This agglomerate was rushed to obtain its strength σ.
- The bond strength was then scaled by $(\frac{\sigma}{\sigma_0})$ to obtain the assumed 37% bond strength B_o.
- The agglomerates were then assumed to have a bond strength given by a Weibull distribution with the chosen m and a 37% bond strength B_o.

Table 5.2 shows the input parameters of agglomerates. Figure 5.19 shows the Weibull probability distribution of experimental results and DEM simulation results. It is concluded that these results exhibit good agreement.

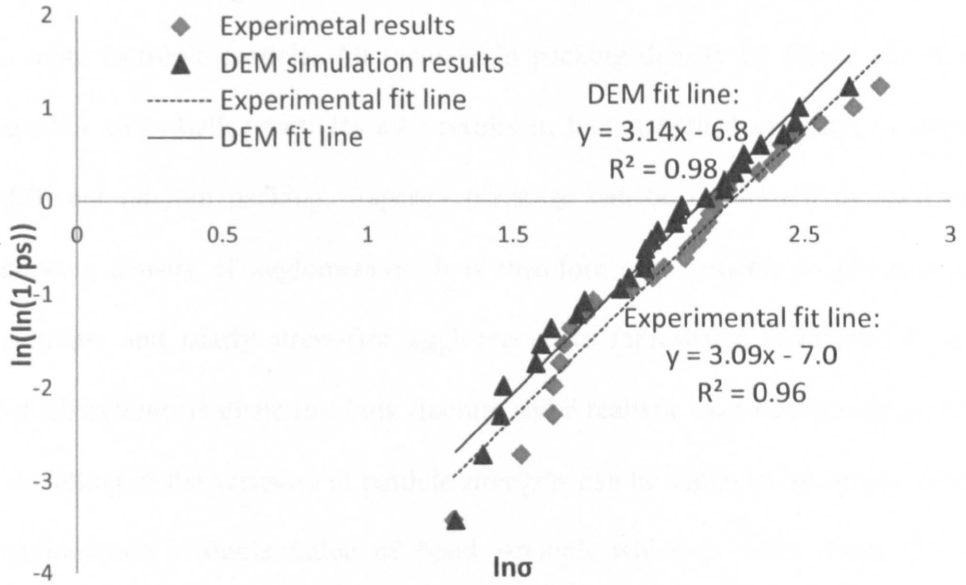

Figure 5.19 Weibull probability distribution for 30 Glensanda ballast experimental results and DEM simulation results

5.5 Summary

A series of experimental diametral compression tests were conducted in this chapter. Thirty particles of three sieve size fractions of Glensanda ballast particles are chosen to be the crushed material: 14-28mm, 30-37.5mm and 40-60mm. Weibull statistic was found to be applicable not only to the static variability of ballast particles strengths but also the size effect on average particle strength. The size distribution of fragments was also analysed and it was concluded that the particles always generally break into two major particles which occupy 60% and 30% of the mass of the original particle and the remaining mass was crushed into fines in diametrical compression tests.

A new algorithm to generate dense random packing agglomerates using DEM has been proposed. The agglomerates were generated by placing new spheres in the tetrahedral void spaces within a relatively loose sample. It was found that the packing

density has a strong influence on the tensile strength. A denser agglomerate results in a more isotropic particle. An increase in packing density by filling the voids with smaller and smaller particles also results in less statistical variation in strength for different random packing. Asperity breakage can be minimised by increasing the packing density of agglomerates. It is therefore now possible to generate a dense, isotropic and nearly stress-free agglomerate to represent a solid particle in DEM, which exhibits realistic fast bulk fracture and a realistic load-displacement curve. The modelling of the variation of particle strengths can be achieved by simply giving each agglomerate a single value of bond strength which is taken from the relevant distribution of the experimental results.

CHAPTER 6 DISCRETE ELEMENT MODELLING OF THE CONE CRUSHER

6.1 Introduction

This chapter introduces the method used to construct a prototype DEM model of a cone crusher chamber. The principal aim of this study was to investigate how prototype fundamental flow and breakage modes may be combined to replicate the size reduction produced by a cone crusher. The study examined the use of the BPM and PBM modelling methods (section 3.4.3) to explore the feasibility of a modelling cone crusher using DEM. A numerical DEM model was built to replicate the performance of a small laboratory scale cone crusher design introduced by Lang (1998). In the application of the PBM method, the octahedral stress induced in each particle was used as the breakage criterion as was proposed by McDowell and De Bono (2013). The breakage criterion and breakage function were determined from a comparison with the results of the experimental compression tests presented in chapter 5. For a given particle feed size distribution, the performance of the computational crusher model was validated by evaluating the effects that changes to the CSS and eccentric speed settings had on the predicted product size distribution. Alternative breakage modes were examined to study their influence on the computed product size distributions. To apply the BPM approach, the feed rock particles are represented by dense random packing agglomerates, introduced in section 5.4.

However, the BPM simulation was performed only once due to the limitation of computation time.

6.2 The construction of cone crusher model

The principal individual rock flow and breakage mode present within a cone crusher chamber are introduced in section 3.1. The feed rock is fed under gravity from a hopper into the top of the crusher chamber. The rocks flowing down the chamber are periodically compressed between the static concave and an eccentric rotating mantle. Figures 6.1 and 6.2 illustrate typical vertical and horizontal cross sectional views through a cone crusher. To construct a representative numerical DEM model of a cone crusher, the geometry of a crusher was defined by the specification of the following eight parameters. The location of these parameter measurements are shown on Figures 6.1 and 6.2.

- The width of feed entrance to the crusher chamber, F.
- The close size setting (CSS): the smallest distance between concave and mantle.
- The throw s: this represents the eccentric distance the cone moves during a half rotation.
- The bite angle β: the angle subtended between the concave and the mantle.
- The cone angle α, measured as the angle as the base of the mantle.
- The eccentric angle γ: the angle of the eccentric rotation of the cone.

- The parallel length of the cone ΔL: the length of the lower part of the concave which is parallel to the mantle in CSS state
- Bottom diameter of the mantle D_c.

As the operation of the DEM cone crusher with a real geometry will consume too much time, a mini artificial cone crusher was simulated in this study. The parameters were determined based on the cone crusher design geometry presented by Lang (1998). Table 6.1 details the values of these parameters.

Table 6.1 Parameter values used to construct the DEM cone crusher model

F(mm)	CSS(mm)	s(mm)	$\beta(^\circ)$	$\alpha(^\circ)$	$\gamma(^\circ)$	ΔL(mm)	D_c(mm)
55	12-18	4.5	18-22	45	2	50	300

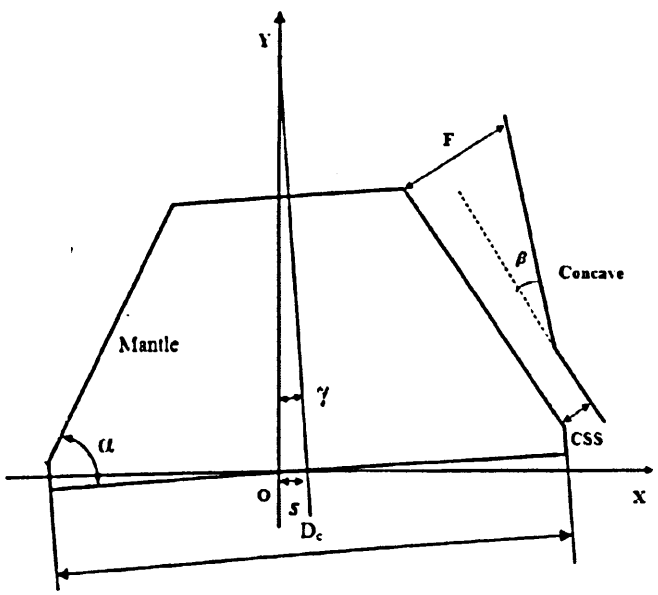

Figure 6.1. A vertical cross-section view through a typical cone crusher.

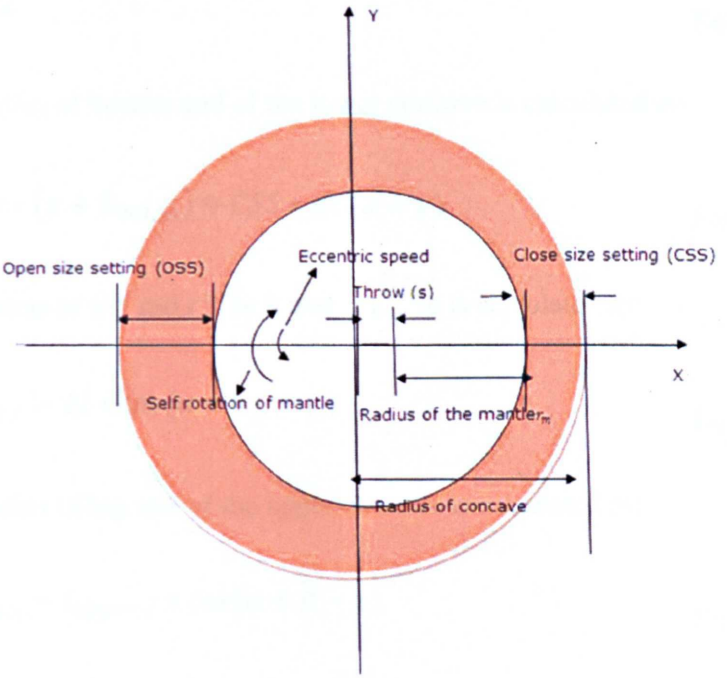

Figure 6.2. A horizontal cross-section view through a typical cone crusher

The mantle was modelled by a cylinder wall, and concave was represented by two cylinder walls of which the lower one was used to model the part of the concave which is parallel to the mantle. The geometry parameters were calculated using values in Table 6.1 by the following procedure; and these parameters were illustrated in Figure 6.3.

- The distance from pivot to the centre of the bottom of the mantle is given by the expression:

$$h = 180s/(2\pi\gamma)$$ **Equation 6-1**

- The length of the upper part of the length of concave is calculated as:

$$l_{upper\_c} = (F - css)/sin\beta$$ **Equation 6-2**

- The radius of the bottom end of the mantle is given by:

$$R_{bot\_m} = D_c/2$$ **Equation 6-3**

- The radius of bottom end of the lower concave is calculated as:

$$R_{bot\_c} = cos\gamma * (s + R_{bot\_m}) + CSS * \sin(\alpha - \gamma)$$ **Equation 6-4**

- The radius of top end of the lower concave is calculated as:

$$R_{mid\_c} = R_{bot\_c} - \Delta l * cos(\alpha - \gamma)$$ **Equation 6-5**

- The radius of top end of the upper concave is calculated as:

$$R_{top\_c} = R_{mid\_c} - l_{upper\_c} * cos(\alpha + \beta - \gamma)$$ **Equation 6-6**

- The radius of the top end of the mantle is derived from:

$$R_{top\_m} = \frac{R_{top\_c} - \sin(\alpha - \gamma) * F}{Cos\gamma * (s + R_{bot\_m})} * R_{bot\_m}$$ **Equation 6-7**

- The side length of the mantle is determined as:

$$l_m = (F - CSS)/\sin\beta$$ **Equation 6-8**

- The coordinate of centre of bottom end of lower concave O_{bot_c} is calculated as: $(0,\ CSS * cos(\alpha - \gamma), 0)$
- The coordinate of centre of top end of the lower concave O_{mid_c} is calculated as: $(0, (0, CSS*\cos(\alpha-\gamma) + \Delta l*\sin(\alpha-\gamma), 0), 0)$
- The coordinate of centre of top end of the upper concave O_{top_c} is calculated as: $(0,\ CSS*\cos(\alpha-\gamma) + \Delta l*\sin(\alpha-\gamma) + \sin(\alpha+\beta-\gamma)*l_m, 0)$
- The coordinate of the centre of bottom end of mantle O_{bot_m}: $(cos\gamma * s,\ -sin\gamma * s, 0)$

- The coordinate of the centre of top end of mantle O_{top_m}: $(R_{top\_c} - \cos\gamma * R_{top\_m}, (CSS - F) * cos(\alpha - \gamma) + \Delta l * \sin(\alpha - \gamma) + \sin(\alpha + \beta - \gamma) * l_m - \sin\gamma * R_{top\_m}, 0)$

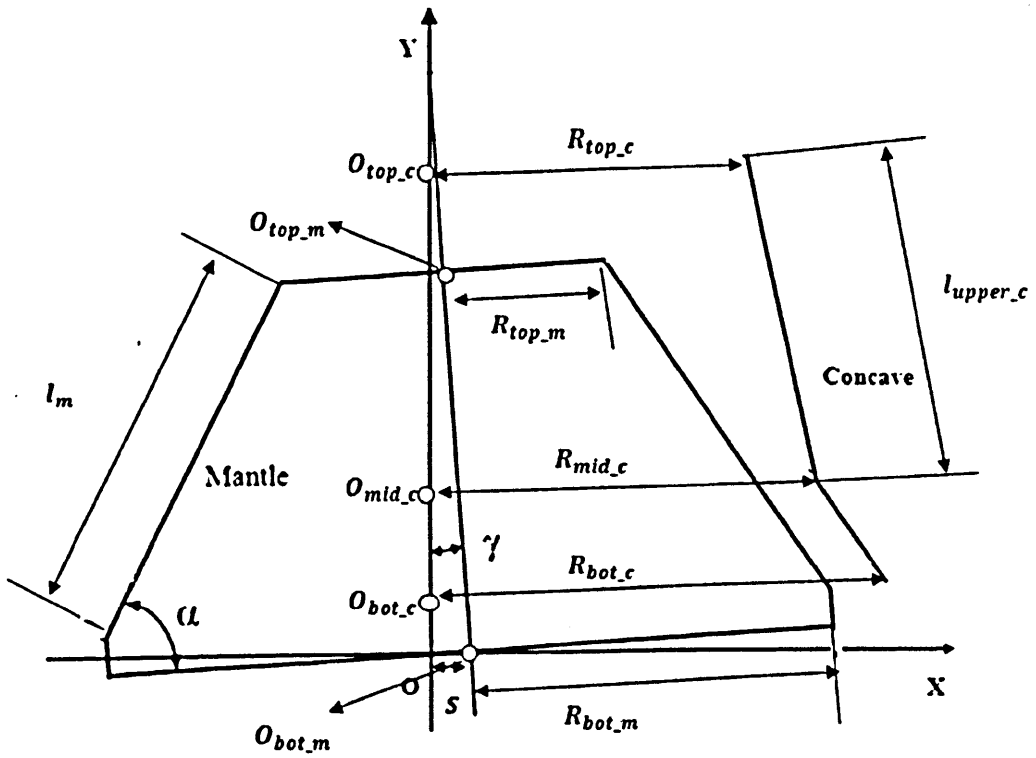

Figure 6.3 Parameters calculated in the DEM cone crusher model

Figure 6.4 shows an illustration of the representative 3D rendered surfaces of the mantle and concaves formed within a typical DEM cone crusher model. The motion of the cone has two components: an eccentric pendular angular velocity ω_{ecc} about the vertical axis of the cone crusher , and a 'spinning' angular velocity of the cone about its own axis ω_{spin}, related to ω_{ecc} by:

$$\omega_{spin} = \frac{R_{bot\_m} + s}{R_{bot\_m}} \omega_{ecc} \qquad \textbf{Equation 6-9}$$

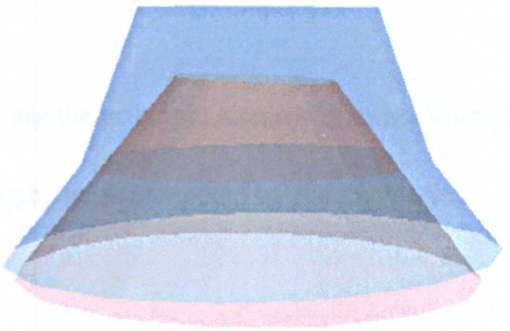

Figure 6.4 The DEM cone crusher model

6.3 PBM model of the cone crusher

The background and theory to the population balance model (PBM) to simulate particle breakage was introduced in section 3.4.3. The basic principle is that the particle will be replaced by a group of new particles of predetermined size when it is subjected to a stress exceeding a specific strength criterion. Each resultant fragment then behaves as a single particle and can be broken again and again until the size of the progeny particle is smaller than a predefined minimum value. The minimum particle size was defined to control the time step of the DEM calculation, the maximum number of particles and thus the computation time. It is essential to determine the breakage criteria and breakage for a population balance model.

6.3.1 Breakage criteria

The octahedral shear stress induced in the particle was used as the breakage criteria in this study, and was first proposed and employed by McDowell and De Bono (2013). The octahedral stress is expressed as:

$$q = \frac{1}{3}[(\sigma_1 - \sigma_2)^2 + (\sigma_1 - \sigma_2)^2 + (\sigma_1 - \sigma_2)^2]^{1/2}$$ **Equation 6-10**

where σ_1, σ_2 and σ_3 are the principle stresses in three directions. In experiments, the results of tensile strengths were computed by the expression:

$$\sigma = \frac{F}{d^2}$$ **Equation 6-11**

where F is the force applied and d is the particle size when fracture occurred. Therefore it is necessary to relate q to σ to calibrate the strength of particles in DEM models. A simple sphere was compressed diametrically between two walls in DEM model. The value of q and σ were both calculated, q was found to be proportional to the characteristic tensile strength

$$q = 0.9\sigma = \frac{0.9F}{d^2}$$ **Equation 6-12**

Therefore the assumption was made that, for the rock particles flowing in the chamber, the particles would be replaced if the octahedral shear stress exceeded its 'strength'. For a given size d, the particle strengths are randomly selected from a Weibull distribution with Weibull modulus m and 37% strength q_o. The quantity q_o is the value of octahedral stress for a particular size such that 37% of particles are stronger. The values of m and q_o are calibrated against the experimental crushing tests in section 5.3 so that m is set as 2.65 and q_o is set as 25.2Mpa. The size effect on the average tensile strengths of a material is usually described in the following form based on the assumption that particles have the same Weibull modulus for all the size fractions:

$$q_o \propto \sigma_{av} \propto d^b$$ **Equation 6-13**

Where q_o denotes the 37% strength for a size d, σ_{av} is the average tensile strength and b is the size effect factor which is constant for a given material. The size effect factor b is set as -1.1 see Figure 5.5.

The Weibull modulus m and the size effect factor b will be decoupled to investigate their influence individually. The Weibull modulus only represents the variability in particle strengths for a given size and the size effect factor only determines the size effect on average particle strengths.

6.3.2 Breakage modes

Two size distributions to represent the post breakage progeny fragments have been investigated. The first model investigated assumed a simple splitting of an idealised original sphere into two new spheres of equal size. To conserve mass, the two progeny fragments were sufficiently overlapped to be contained within the bounding parent sphere. The axis joining the centres of the two new spheres was aligned along the direction of the minor principal stress, as shown in Figure 6.5. This overlap causes the particle fragments to move along the direction of the minor principal stress of the original parent particle, as may occur when a single particle is compressed between two flat parallel platens. (McDowell & De Bono, 2013). The alternative breakage function was shown in Figure 6.6, where the original particle is split into three particles which individually represent 60%, 30% and 10% of the mass of the original particle. As for the previous mechanism, the centres of the three new progeny particles are created along the direction of the minor principal stress (Figure 6.6). The second breakage function is formed to replicate the size distributions of the broken rock particles produced by the diametrical compression tests, described in section

5.3.3. An examination of these experimental results concluded that the particle predominantly divided into two major sized particles which occupied approximately 60% and 30% of the original mass (Figure 5.6), and the remaining 10% mass reported as crushed into fine particles. In the construction of the breakage model, it was decided to represent the 10% mass reporting as fines by a single sphere to decrease the total number of particles generated within the simulation.

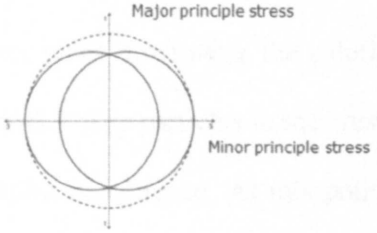

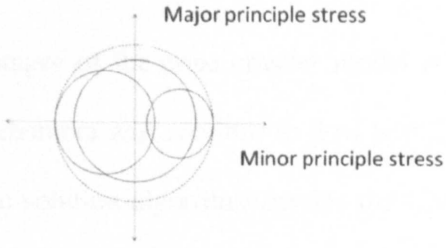

Figure 6.5 Two ball splitting mechanism **Figure 6.6 Triple split mechanism**

However, huge undesirable local pressure spikes were generated by the overlaps of fragments in both size distribution functions. The imposed elastic energy caused by the overlap needs to be accommodated after every update of particle breakages. Otherwise, all the fragments will break infinitely under the artificial created huge pressure. In order to accommodate this problem, the author defined a 'freeze state' to release the artificial energy. The cone crusher model will be set into the freeze state once breakage occurs with the following assumptions:

- When new particles are generated, all other particles are given initial zero rotational and translational velocities. The locations of the boundaries (the walls of the crusher model) are fixed.

- In this state, all of the particles are temporarily assigned an artificially large mass ($3x10^9$ kg/m^3) to minimise the motions caused by collision.
- The new particles are given an artificially low stiffness ($1x10^3$ N/m) to minimise the energy release generated by the overlaps.
- The viscous damping system is removed and a high local damping coefficient 0.9 (section 2.5.1) is added to accelerate the stabilization of the new particles.
- Gravity is removed.

A flow chart illustrating the solution stages of the cone crusher model is shown in Figure 6.7. The particles in the crusher chamber will continue to flow until a breakage condition is achieved. At this point, the solution algorithm applies the 'freeze' state until the artificial energy of the new fragments is released and dissipated. Thereafter, the model reverts to the normal state allowing the particles to continue to flow. It should be noted that the instantaneous velocities of all particles are recorded before the system applies a freeze state, after which these velocities are returned to either the original unbroken particles It is noted that a local damping system was replaced in the model by a viscous damping system, when the solution algorithm reverts from the freeze to the normal state.

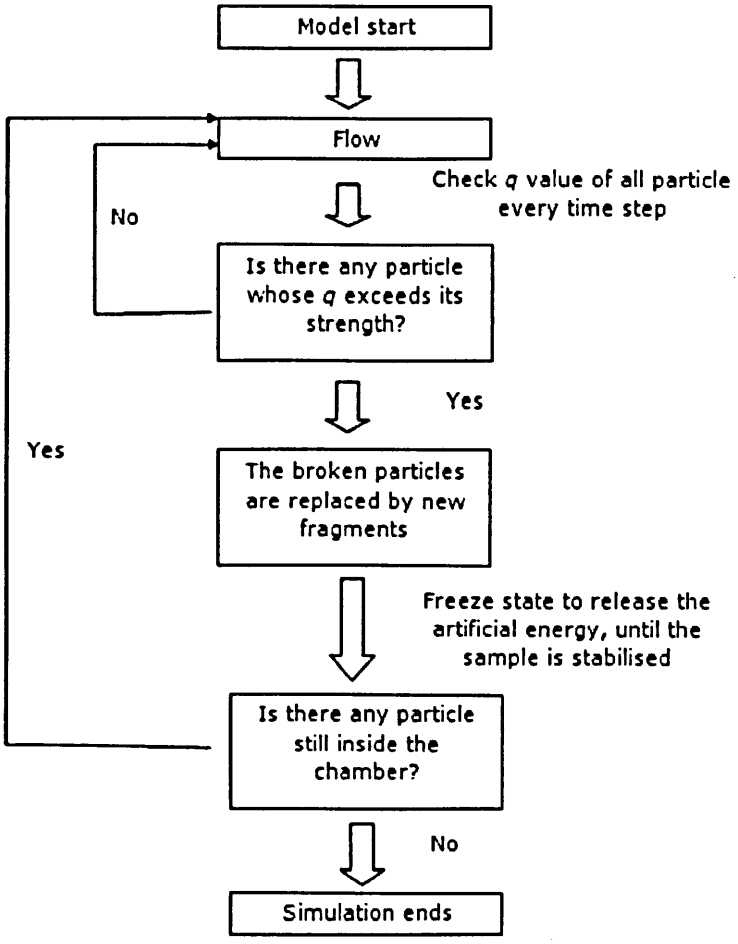

Figure 6.7 Flow chart of the cone crusher model using PBM approach

6.3.3 Parameter decision

A simple sphere was used to present the particle in the current state of this research. The contact model used here is linear contact model (section 2.5.2). Two hundred particles were used as the feed material to save computation time. The size of the feed material needs to be chosen from the size range of the experimentally crushed ballast particles as the experimental results of the tensile strengths are necessary to calibrate the rock breakage criteria in the DEM model. The size fractions of ballast particles

crushed in chapter 5 were 14-28mm, 30mm-37.5mm and 40mm-60mm. The smallest size fraction 14-28mm was chosen as the size range of the feed material. Therefore the feed particles are 200 spheres with a random diameter between 14mm ($\sigma_o = 38.6MPa$) and 28mm ($\sigma_o = 18.2MPa$).

Table 6.2 shows the input parameter of the system. The particle stiffness were calculated by the equation given by Itasca Consulting Group, Inc (2008), which is the Young's modulus of the material E_c to the radius of the balls R and stiffness:

$$k_n = k_s = 4RE_c \qquad \textbf{Equation 6-14}$$

A typical value of the Young's modulus for the Glensanda granite ballast tested in Chapter 4 was determined to be 70GPa. The ball-ball coefficient of friction measured in the flow experiments introduced in chapter 4 was set as 0.37. As the solution of this model represents a dynamic process, the viscous damping model (section 2.5.1.) was chosen to model the energy dispersion experienced during the collision of the particles. The critical damping ratio of 0.11 used in the flow model in chapter 4 was adopted for these models. The minimum size of the spherical particles modelled to flow within the crusher chamber was set at a diameter of 4mm. This defines the smallest breakable size of a particle generated by the solution.

Table 6.2 Input parameter of the cone crusher model for PBM approach

Critical damping ratio	0.11
Ball/wall friction	0.37
Ball/ball friction	0.37
Wall stiffness	1e13 N/m
Particle Young modulus	70Gpa
Ball density	2650kg/m^3

6.3.4 Simulation procedure

Figure 6.8 shows snapshots of the crusher simulation in action. In industry the feed material is usually loaded to the crusher feed bin by a hydraulic shovel or by a conveyer belt. This material is then ideally choke fed under gravity into the top of the cone crusher chamber. It is difficult to entirely replicate this complex feed process within the model, and thus the feed is simplified by assuming that the feed particles flow from a full bin located vertically above the crusher chamber. The computational algorithm is detailed as follows:

- 200 particles are randomly generated inside an artificial cylinder wall 1, representing the feed bin (labelled in Figure 6.8).
- The spheres representing the feed material are deposited by the gravity into the feed bin. A flat artificial wall 2 (labelled in Figure 6.8) is constructed above the concave to avoid the particles from dropping directly through the chamber.
- The flat artificial wall 2 is then deleted to let the particles to flow under gravity through the top of the crusher chamber. A conical artificial wall 3 (labelled in Figure 6.8) was constructed to cap the top of the mantle, and this prevents any particles from flowing into the hollow mantle.

- The mantle is rotated.

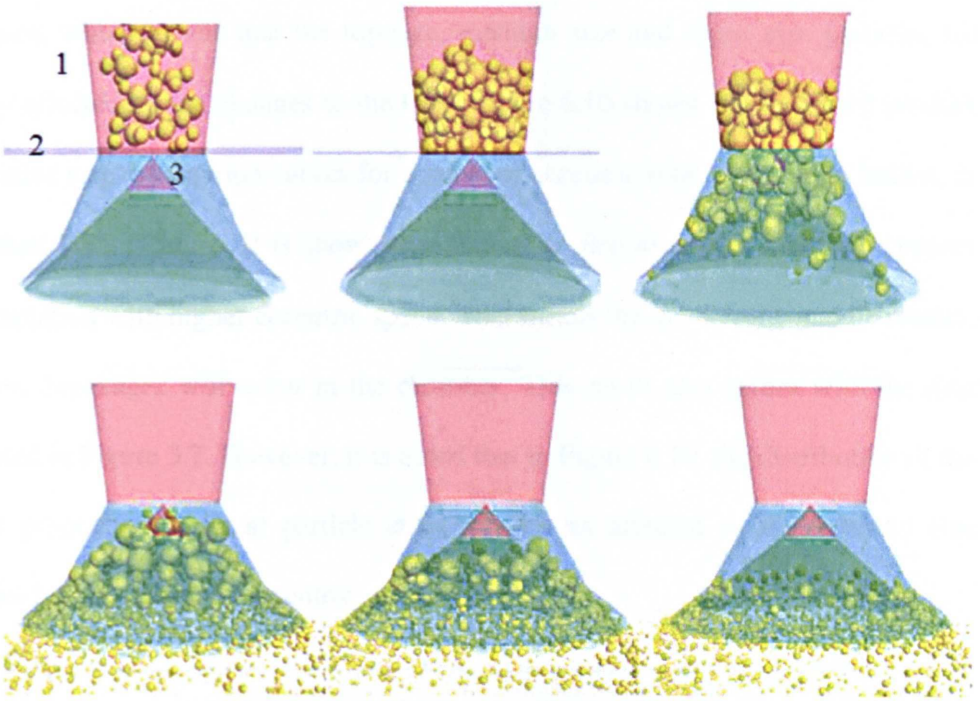

Figure 6.8 A series of computer animation stills depicting the dynamic performance of the crusher predicted by the model

6.3.5 Model validation

For the DEM cone crusher model, the influence of changing the CSS and eccentric speed on the size distribution of the products was first studied. The results were then qualitatively validated with Figure 3.6 and Figure 3.7 in the literature review.

The triple split breakage mode was used to generate the progeny fragments size distribution function. Figure 6.9 shows the product size distributions generated by the model for various CSS for a fixed eccentric speed of rotation of 300 rpm. From an examination of these results it is clear that the feed particles will experience greater size reduction as the CSS decreases. This is qualitatively consistent with the data

presented in Figure 3.6. Note that in both Figure 3.6 and 6.9 the computed product cumulative size distribution curves are translated horizontally to the left as the CSS decreases, which means that the top-size, medium size and finest size particles are equally affected by the changes to the CSS. Figure 6.10 shows the computed product cumulative size distribution curves for a range of eccentric rotational speeds values, at a constant CSS (15mm). It is shown that the upper size distribution curve represent the simulation with higher eccentric speed. That means the quicker the mantle rotates, the more breakages will occur in the chamber. This result also agrees with the data presented in Figure 3.7. However, it is noted that in Figure 6.10, the distribution of the largest products and finest particle sizes are not as affected as the medium size particles by the change of eccentric speed.

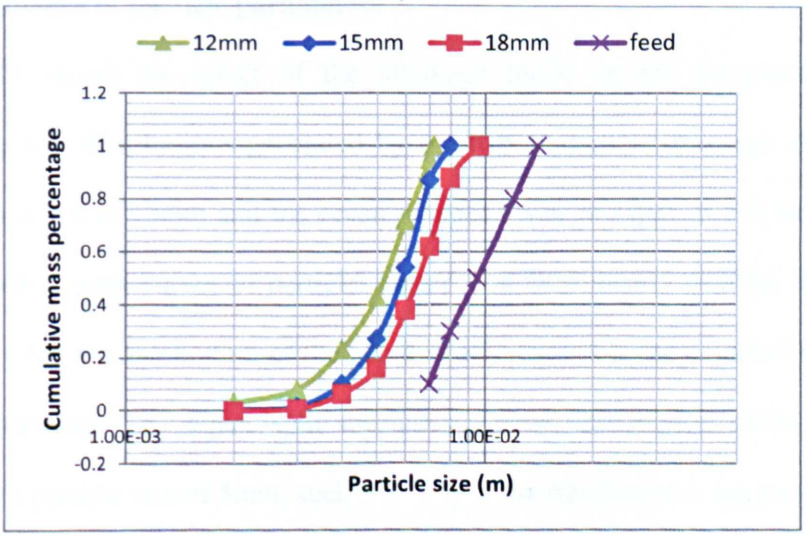

Figure 6.9 The effect of CSS on size distribution of products in DEM simulation

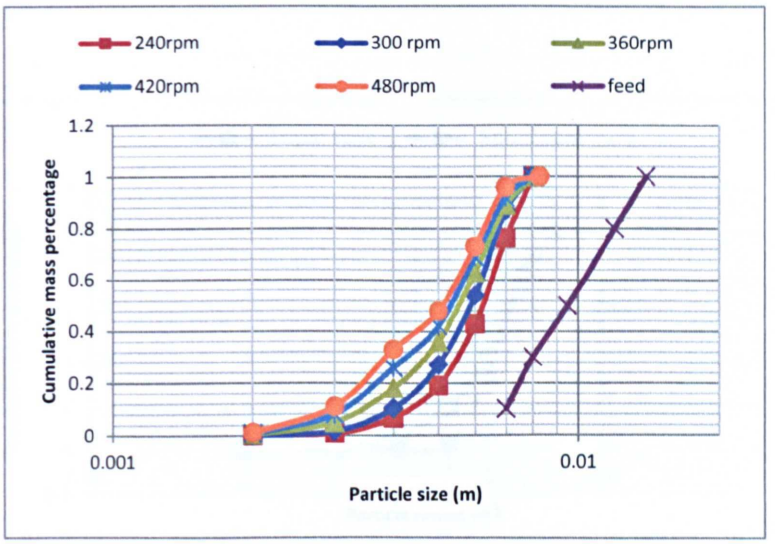

Figure 6.10 The effect of eccentric speed on size distribution of products in DEM simulation

6.3.6 Influence of particle parameters

Figure 6.11 shows the effect of the breakage mode on the computed product cumulative size distributions generated by the two alternative breakage algorithms. The CSS was set at 15mm and the eccentric speed was 300 rpm. It can be seen that the cumulative mass curves of particles larger than 6mm nearly overlap. The major difference occurs at the bottom of the curve which represents the cumulative mass of the fine particles. The equal split mechanism mass distribution curve suddenly changes at a particle size of 5mm, such that only a few fine particles are generated.

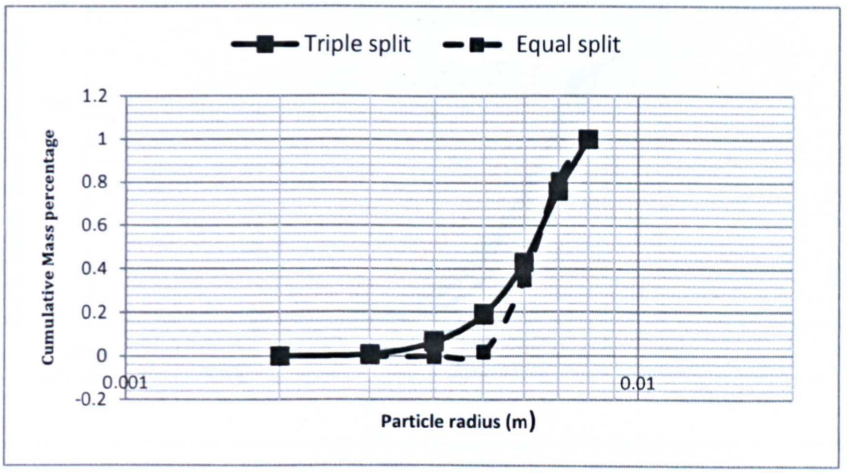

Figure 6.11The effect of breakage mode of fragments

All the particle strengths are governed by a 37% strength, σ_0, the size effect factor, *b*, and the Weibull modulus ,*m* (see section 6.3.1). Model simulations using various values of these three parameters have been performed to investigate their effect on the predicted cumulative size distribution of the products. Figure 6.12 shows the effect of changing the σ_0 parameter, for a constant *b* of -1.1 and constant *m* of 2.65. It can be observed that the predicted solution curves nearly overlap when σ_0 varies from 10MPa to 20MPa. However, if σ_0 is increased or decreased by a factor of 10, to values of 80 or 0.8 MPa, respectively it is clear that more size reduction occurs at lower values of σ_0.

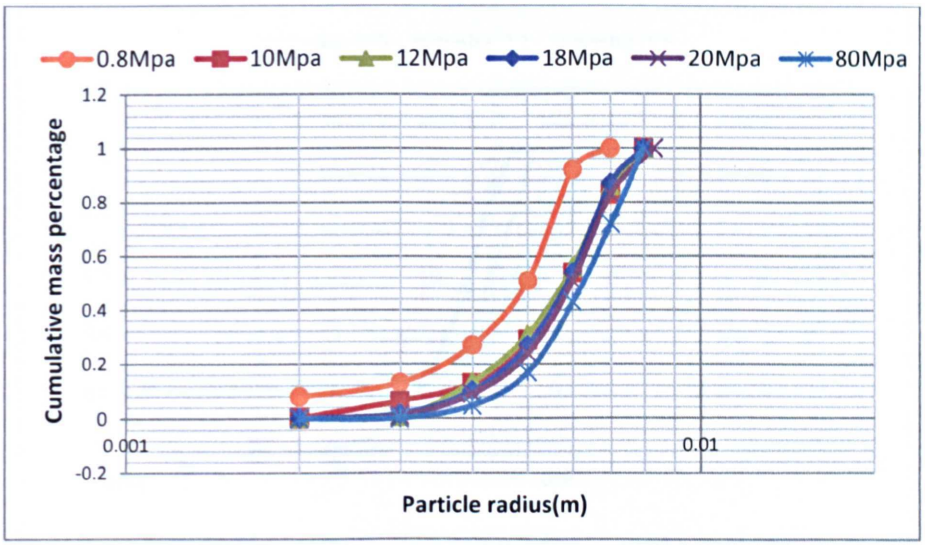

Figure 6.12 effect of σ_o on size distribution of products

Figure 6.13 shows a plot of the computed particle strengths as a function of particle size for various values of *b*. For similarly sized fragments, an increase in the value of *b* results in a lower strength. Figure 6.14 shows the cumulative particle size distribution as a function of the size effect factor *b*. It is evident that the increasing *b* results in more breakage in the crusher chamber.

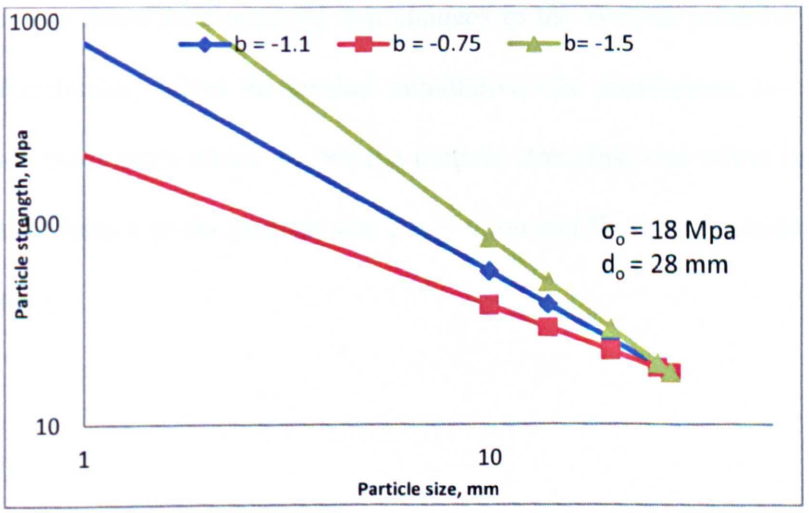

Figure 6.13 Particle strengths as a function for various *b* with initial particle strength 18Mpa

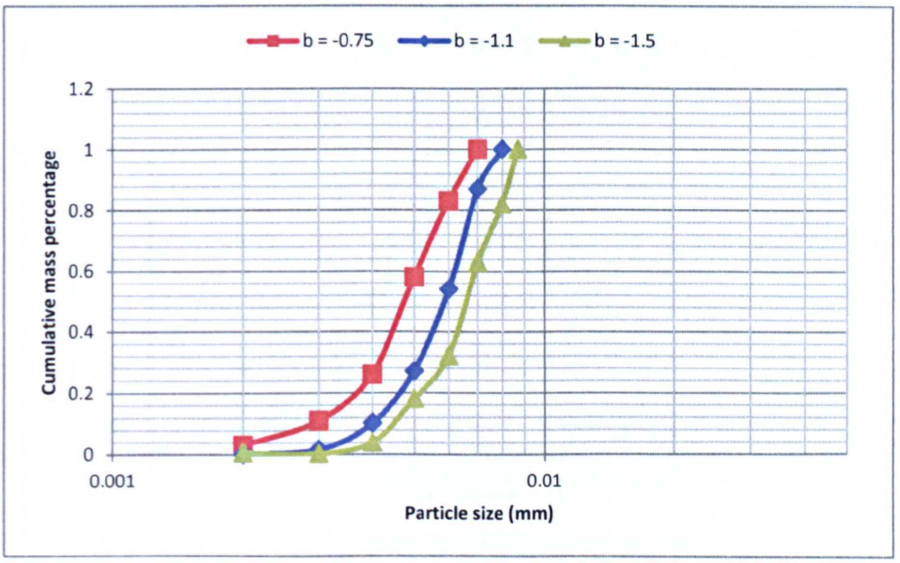

Figure 6.14 effect of *b* on size distribution of products

Figure 3.20 shows the effect that changes in the value of the Weibull modulus parameter have on the predicted particle strengths. Figure 6.15 shows the influence that changes to the value of the Weibull modulus parameter *m* have on the cumulative product size distribution, for a constant value of b=-1.1 and σ_o =18MPa for the largest particle size. The three curves for the different Weibull modulus *m* values are almost coincident. It is therefore concluded that changes to the Weibull modulus parameter does not significantly affect the product cumulative size distribution. In conclusion, for the three parameters which govern the particle strengths, size effect factor *b* has the greatest influence to the product size distribution and Weibull modulus *m* has the least influence.

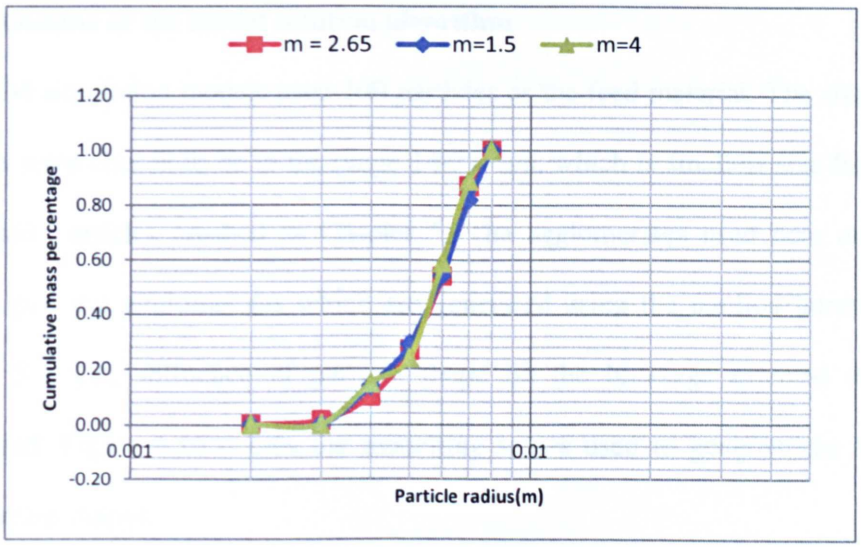

Figure 6.15 effect of *m* on size distribution of products

6.4 BPM model of the cone crusher

The BPM model is based on the principle of bonding spheres together to form an agglomerate to represent a rock particle. Breakage is represented by broken bonds. Compared with the PBM model, the model can take into consideration particle movement as a result of a crushing sequence as the particle is broken into smaller agglomerates directly. This cannot be achieved for the PBM approach because the fragments have to be located at the same position as the original particle. However, the BPM approach consumes much greater computational time than the PBM approach. For example, the agglomerate generated in chapter 5 contains 1600 spheres; 320,000 spheres are needed to construct a 200 particle cone crusher model. This can take 5-6 months for one simulation. Therefore, only one simulation has been performed in this project to examine its feasibility.

6.4.1 Outline of the model solution algorithm

The DEM simulation models used 100 particles as the feed material. The sizes of the particles were chosen to be in the range 14-28 mm, which is smallest size fraction of the ballast particles crushed in Chapter 5. The agglomerates used here are dense random packing agglomerates which are generated using the method introduced in section 5.4. The influence of particle shape on the breakage effected was also considered. Figure 6.16 details the modelling stages used to generate the irregular agglomerate shapes.

- Generate a spherical random dense packing agglomerate of radius ratio 4 using the method introduced in section 5.4. The radius of the agglomerate should be at least equal to the measured sieve size of the real particle.
- Calculate the three dimensional external profile of the real particle. The tool used here was a 3D laser digitizer.
- Check the centres of all the spheres in the agglomerate to reject the spheres whose centres lie outside the boundary.

Figure 6.16 The modelling procedure used to generate irregular particle shapes

The micro input parameters used are calibrated in section 5.4 and shown in Table 5.2. The simulation procedure was shown in Figure 6.17, which depicts animation stills of the sequential stages of the solution of the model. The procedure is as follows:

- 100 particles of radius 28mm were randomly generated inside the artificial cylinder wall above the mantle.
- The spheres are replaced by agglomerates.
- The agglomerates are deposited into the feed bin by gravity. The bonds of the agglomerates are given an artificially high bond strength to avoid breakage during the deposition process. A flat artificial wall is constructed above the concave to avoid the particles dropping into the chamber directly.
- The bonds in the agglomerates are re-allocated their normal values. The flat artificial wall is then deleted to allow the particles to flow into the chamber.
- The mantle is rotated.

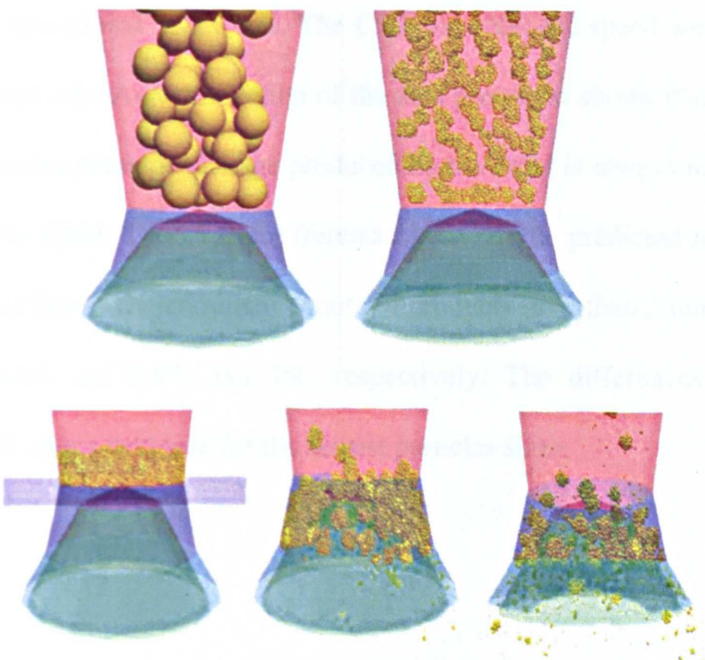

Figure 6.17 Snapshots of the crusher simulation in action using BPM approach

6.4.2 Results

The sizes of the fragments were calculated as the equivalent radius, expressed as:

$$R_f = \sqrt[3]{\frac{3M}{4\pi\rho(1-P)}} \qquad \textbf{Equation 6-15}$$

where R_f represents the equivalent radius of the fragment and M denotes the cumulative mass of all the spheres included in the fragment, ρ is the density of micro spheres which is 2650kg/m^3 shown in Table 6.2, and P is the porosity of the initial agglomerate which is 0.31 shown in Figure 5.16

The stills animations shown on Figure 6.17 show that some fragments are projected upwards out of the crusher chamber or bin. This dynamic phenomenon is caused by particle collisions and may also occur in the operation of real cone crushers. Figure 6.18 shows a graphical comparison of the predicted cumulative product size distributions for the two breakage modes using the same cone crusher model geometry and operational conditions. The CSS and eccentric speed were 15 mm and 300 rpm, respectively. An examination of the data presented shows that for any sieve size, the cumulative mass percentage produced by the BPM is always higher than that computed by the PBM. The largest differences between the predicted solutions occur at the finest size 2mm. The cumulative mass of products finer than 2 mm for the BPM and PBM models are 9.8% and 1%, respectively. The differences between the predicted distributions decrease for the largest particles sizes.

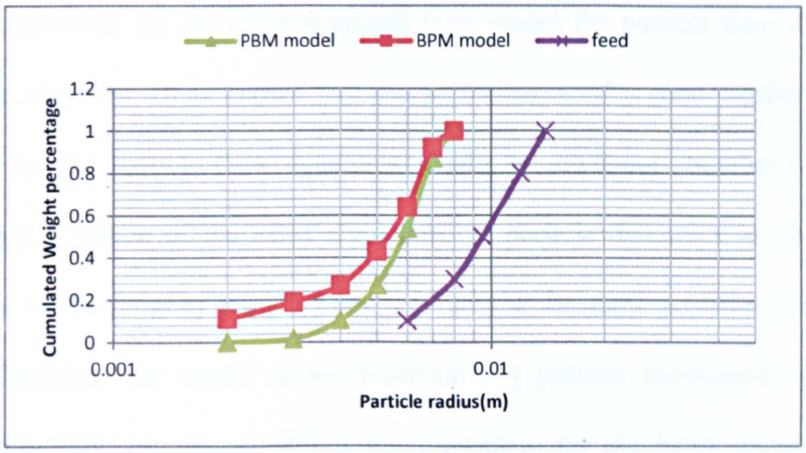

Figure 6.18 Comparison of BMP cone crusher and PBM cone crusher

6.5 Summary

A prototype DEM cone crusher model has been successfully constructed using two approaches: PBM and BPM. The performance of these crusher models were assessed by examining the influence that changes to the CSS and eccentric speed settings have on the predicted cumulative product size distributions. It was found either a decrease in the CSS or an increase in the eccentric rotational speed resulted in more computed breakage events within the crusher chamber, which are consistent with the evidence in the literature. The breakage mode was also found to influence the cumulative size distribution of the products. Three parameters were identified as characterising the strength of a particles: 37% tensile strength σ_o , the size effect factor b and an the Weibull modulus m. The size effect factor b is found to have most influence on the product cumulative size distribution, whilst changes to the Weibull modulus m produced little change. Unfortunately, due to the large number of computations required by the BPM approach, it was only possible to perform a single model simulation using this method.

It was concluded that the use of both breakage modes with the prototype DEM cone crusher model were able to satisfactorily replicate the performance of a cone crusher.

The main challenge for the PBM approach is to model the particle flow dynamic in the crusher chamber. (It is known that the performance of a cone crusher is highly dependent on the particle flow dynamics within the crushing chamber.) However, during the application of the PBM algorithm the particle dynamics are temporarily deactivated as the progeny particles are generated at the same position as the parent particle. Therefore the model cannot replicate any particle movements during the crushing sequence. In contrast, this is not a problem for the BPM approach as the agglomerates are actually broken into smaller agglomerate. However, the PBM approach is much more computationally efficient than the BPM model. Based on the resulting particle size distributions for the two approaches, it can be concluded that the simple PBM model may be very useful in quickly establishing the influence that changes to the parameter values may have on the predicted cone crusher performance if computational time is an issue.

CHAPTER 7 CONCLUSIONS AND SUGGESTIONS FOR FUTURE WORK

7.1 Conclusions

The main aims of the research reported in this thesis were as follows:

1. To develop a DEM model to replicate the flow and breakage through cone crushers
2. To develop a more fundamental understanding of the rock and machine parameters that contribute to the optimum flow and breakage of rock within cone crushers
3. To investigate the influence of the chamber geometry on predicted rock flow and breakage.
4. To investigate the role of feed rock size distribution on the predicted product rock sizes produced.
5. To validate the models developed against known machine and rock parameters.

The following specific objectives have been achieved in order to meet these aims:

1. A critical literature review has been performed on the cone crusher including the working principles of the cone crusher and recent research that has been conducted to characterise the performance of cone crusher.
2. A critical literature review has been performed on rock comminution and the characterisation and analysis of rock particle size.

3. A critical literature review has been performed on the concepts of DEM and PFC^{3D}, and recent relevant applications.
4. Physical experiments of flow of single sized pebbles in a chute have been conducted. Corresponding DEM simulations have been performed and validated with the results.
5. Physical experiments of zones of flow of different sizes (three size fractions) in a chute and corresponding simulations have been conducted. The DEM model has been validated with the experimental results.
6. Experimental work on single ballast particle breakage of three size fractions between parallel steel plates has been performed. The variation of tensile strengths, the size effect on tensile strengths and the size distribution of the fragments have been analysed.
7. Diametrical particle compression tests have been simulated using DEM.
8. The DEM cone crusher model has been constructed using both PBM approach and BPM approach.
9. A parametric study of the cone crusher has been performed to investigate the influence of chamber geometry on the size distribution of the products.
10. The DEM cone crusher model has been validated with the literature.

The conclusions that can be drawn from this research are:

Flow

- A simple inverse method using the heap test to establish the angle of repose (Ferellec & McDowell, 2010) to determine the correct particle–particle friction coefficient of irregular shaped particles is found to be an appropriate way to calibrate the particle-particle friction coefficient in DEM modelling irregular material.

- The viscous damping system should be chosen in DEM for a dynamic model. The critical damping ratio can be calibrated by using the restitution coefficient of the particle which was measured by a drop test in the lab.
- Modelling particle shape is important for DEM modelling of irregular material flow; the four-ball clumps give a more accurate prediction of the velocities of pebbles than simple sphere.
- The deposition method will affect the velocities of the particles in DEM modelling the flow of irregular shaped particle.
- For a given bite angle, there is a minimum value of CSS normalised by particle size below which flow does not occur, and a maximum value beyond which the clearance time does not reduce.
- For a given CSS, the clearance time increases dramatically with an increasing bite angle.
- It is possible to model the flow of irregular shaped particles in three dimensions if due care is taken over the selection of clump shape and determination of the correct particle parameters.

Breakage

- Weibull (1951) statistic is verified to be appropriate to be applied on the variability of ballast particle strengths.
- In diametrical compression tests the particles usually break into two major particles which occupy 60% and 30% of the mass of the original particle and the remaining mass was crushed into fines.
- The hexagonal closed packing is found to be extreme anisotropic so that it may not be suitable to model particle breakage under multiple contacts.

- A new method of forming a dense, isotropic rock particle with negligible initial overlap by inserting particles to fill the voids in the agglomerate was proposed.
- It is found for a dense random packing agglomerate, the packing density has a strong influence on the tensile strength of the particle. The denser agglomerate has a higher tensile strength.
- A denser agglomerate results in a more isotropic particle.
- An increase in packing density by filling the voids with smaller and smaller particles also results in less statistical variation in strength for different random packings.
- Asperity breakage can be minimised by increasing the packing density of agglomerates.
- The modelling of variation of particle strengths can be achieved by simply giving each agglomerate a single value of bond strength which is taken from the same distribution of the experimental results for the target particles.

Cone crusher

- Both the BPM approach and PBM approach can be used to construct a cone crusher model.
- For the PBM approach, decreasing the CSS results in more breakage in the crusher chamber.
- For the PBM approach, more fine particles can be obtained by increasing the eccentric speed of the crusher.
- For the PBM approach, the breakage mode has been found to influence the size distribution of the product.

- For the PBM approach, the size effect factor b has a significant influence on the size distribution of the products.
- For the PBM approach, the initial tensile strength of the largest particle σ_o influences the size distribution of the products.
- For the PBM approach, the Weibull modulus m which represents the variability of tensile strengths of particles has a minor effect on the size distribution of the products.
- Based on the resulting particle size distributions for the two approaches, it can be concluded that the simple PBM model may be very useful in establishing quickly the effects of different micro parameters if computational time is an issue.

7.2 Future work

The breakage mode has been proved to effect the size distribution of product for the PBM cone crusher model. The breakage mode used in this study was obtained from the size distribution in the fragments of the experimental diametral crushing tests. However, the fragments may be different for a particle fractured under diametrically crushing and multi-direction crushing. Thus, the breakage modes of particle under multi-direction crushing are suggested to be examined experimentally. This can provide the PBM cone crusher model with more reasonable breakage modes.

Particle shape has been shown to be important for DEM modelling of particle flow. However, only spheres were used as the feed material in the BPM cone crusher to save time. It is suggested that the feed material is replaced by irregular shaped clumps

to investigate the importance of the shape of the feed material on the size distribution of products for a DEM cone crusher model.

More simulations of the BPM cone crusher model need to be performed. The effect of different parameters (such as CSS, eccentric speed) on the size distribution of products needs to be investigated. The results need to be compared with that of the PBM model to determine if BPM model can be used to research the effects of different micro parameters if time is an issue.

More quantitative validations are necessary for both cone crusher DEM models. It is necessary to validate the models against known machine and rock parameters and refine the models to give greater quantitative agreement with experiments, so that DEM can be used to increase comminution efficiency.

REFERENCES

Astrom, J. A. and Herrmann, H. J.(1998). Fragmentation of grains ina two-dimensional packing. *Eur. Phys. J. B* 5, No. 3, 551–554

Billam, J. (1972). *Some aspects of the behaviour of granular materials at high pressures. Stress-strain behaviour of soils.* Proceedings of the Roscoe Memorial Symposium (ed. R.H.G.Parry). pp.69-80

Bond, F.C. (1952). *The third theory of comminution*, Trans, AIMF, 193, 484

CEEC (2012). Comminution: waging war on Watts, *Mining World*, 9(5), 2012

Cheng, Y. P., Nakata, Y., & Bolton, M. D. (2003). Discrete element simulation of crushable soil. *Geotechnique,53*(7), 633-641.

Cil, M. B., & Alshibli, K. A. (2012) 3D assessment of fracture of sand particles using discrete element method. *Géotechnique Letters, 2*(July-September), 161-166.

Cil, M.B., Alshibli, K.A., McDowell, G.R. and Li, H. (2013) Discussion: 3D assessment of fracture of sand particles using discrete element method. *Geotechnique Letters 3*, No January-March, 13-15

Cleary, P.W. (2001a). Recent advances in DEM modelling of tumbling mills. *Minerals Engineering, 14*(10), 1295-1319.

Cleary, P. (2001b). Modelling comminution devices using DEM. *International Journal for Numerical and Analytical Methods in Geomechanics*, 25(1), 83-105.

Cleary, P.W. (2008), The effect of particle shape on simple shear flows. *Powder Technology*, **179**, No.3, 144-163.

Cleary, P. W., Morrisson, R., & Morrell, S. (2003). Comparison of DEM and experiment for a scale model SAG mill. *International Journal of Mineral Processing*, 68(1), 129-165.

Cleary, P.W., and Sawley, M.L. (2002) DEM modelling of industrial granular flows: 3D case studies and the effect of particle shape on hopper discharge. *Applied Mathematical Modelling*, **26**, No. 2, 89-111.

Cundall, P.A. (1971) A computer model for simulating progressive large scale movements in blocky rock systems. *Proceedings of the Symposium of the International Society of Rock Mechanics, Nancy, France*, Vol.1 Paper, NO. 8

Cundall, P. & Strack, O. (1979). A discrete numerical model for granular assemblies, *Geotechnique*, 29(1) 47-65

Cundall, P.A. (1987) Distinct Element Models of Rock and Soil Structure. *In Analytical and Computational Methods in Engineering Rock Mechanics*, Ch.4, pp. 129-163

Cundall, P. A., (1988) Computer Simulations of Dense Sphere Assemblies, *Micromechanics of Granular Materials*, pp. 113-123.

Cundall, P.A. and Hart, R.D. (1992). Numerical Modelling of Discontinua, *Engineering Computations*, 9(2), 100-113

Davidge, R.W. (1979). *Mechanical behaviour of ceramics*. Cambridge University Press.

Evertsson, C.M. and Bearman, R.A. (1997) Investigation of Interparticle Breakage as Applied to Cone Crushers, *Minerals Engineering, 10*, 199-214

Evertsson, C.M. (1997) *Prediction of Cone Crusher Performance*, Lic. Eng.Thesis, Machine and Vehicle Design, Chalmers University of Technology, January 17, 1997

Evertsson, C.M. (1998) Output Prediction of Cone Crushers. *Minerals Engineering*, 1998, 11(3), 215-232.

Evertsson, C.M. (1999). Modelling flow in Cone Crushers, *Mineral Engineering* Vol.12, 1479-1499, Dec 1999

Evertsson, C.M. (2000). *Cone crusher performance*, Ph.D. thesis, Chalmers University of Technology, Sweden

Evertsson, C.M. (2003). Prediction of worn geometry in cone crushers. *Minerals engineering*. 16(2), 1355-1361

Ferellec, J.F. and McDowell, G.R. (2008). A simple method to create complex particle shapes for DEM. *Geomech. Geoeng* 3, NO. 3, 21-216.

Ferellec, J.F. and McDowell, G.R. (2010). Modelling realistic shape and particle inertia in DEM. *Geotechnique* 60, No. 3, 227-232.

Gauldie, K. (1953) Performance of Jaw Crushers, *Engineering*, 456-458, October 9, 485-486, October 16, 1953

Gauldie, K. (1954) The Output of Gyratory Crushers, *Engineering*, 557-559, April 30, 1954

Ginsberg, H.H., and Genin, J. (1984) *Dynamics*, Seond Edition. New York: John Wiley and Sons.

Grieco, F.W. and Grieco, J.P. (1985). *Manufacturing and Refurbishing of Jaw Crushers*, CIM Bull., 78(Oct.)

Griffith, A. A. (1920). The phenomena of rupture and flow in solids. *Phil. Trans. R. Soc. London A* 221, No. 582–593, 163–198.

Herbst, J.A. and Potapov, A.V. (2004) Making a discrete grain breakage model practical for comminution equipment performance simulation. *Powder Technology* 143-144(2004) 144-150

Herbst, J. A., Lo, Y. C., & Flintoff, B. (2003). *Size reduction and liberation. Principles of Mineral Processing*, MC Fuerstenau and KN Han (eds.), Society of Mining, Metallurgy and Exploration, Littleton, CO, 61-118.

Hiramatsu, Y., & Oka, Y. (1966). Determination of the tensile strength of rock by a compression test of an irregular test piece. *International Journal of Rock Mechanics and Mining Sciences & Geomechanics Abstracts* , 3(2), 89-90

Hukki, R.T. (1961). *Proposal for a solomonic settlement between the theories of von Rittinger*, Rick and Bond. Trans SME/AIME, 403-408

Hulthen, E. (2010). *Real-time optimization of cone crushers*. PhD thesis. Chalmers University of Technology.

Inglis, C.E.(1913). Stresses in a plate due to the presence of cracks and sharp comers. *Proc. Inst. Nav. Arch.*

Itasca Consulting Group (2008). Inc. *PFC^{3D} (Particle Flow Code in Three Dimensions)*, version 3.0. Minneapolis: ICG.

Jaeger, J. C. (1967). Failure of rocks under tensile conditions. *Int. J.Rock. Mech. Min. Sci. Geomech. Abstr.* 4, No. 2, 219–227

Iwashita, K. and Oda, M. (1998), Rolling resistance at contacts in simulation of shear band development by DEM. *Engineering Mechanics*, **124**, No.3, 285-293.

Karra, V.K. (1983) *Process performance model for cone crushers, XIV International mineral processing congress*, CIM, Montreal, Que, Canada, Toronto, Canada, pp. III 6.1 - III 6.14.

Kick, F. (1885). *Des Gesetz der Proportionalem widerstand und Seine Anwendung*, Felix, Leipzig

Lang, B.X. (1998) *The Cone Crusher* (first ed.) Mechanical Industry Publishing Company, Beijing

Langston, P.A., Al-Awamleh, M.A., Fraige, F.Y. and Asmar, B.N. (2004) Distinct element modelling of non-spherical frictionless particle flow. *Chemical Engineering Science* 59, 425-435.

Langston, P. A., Matchett, A. J., Fraige, F. Y., & Dodds, J. (2009). Vibration induced flow in hoppers: continuum and DEM model approaches. *Granular Matter*, *11*(2), 99-113.

Lee, D. M. (1992). The *angles of friction of granular fills*. PhD dissertation, University of Cabridge

Li, H., McDowell, G.R. and Lowndes, I. (2012) A laboratory investigation and discrete element modelling of rock flow in a chute. *Powder Technology* 229, 199-205.

Li, H., McDowell, G.R. and Lowndes, I. (2013) Discrete element modelling of rock breakage using dense random packing agglomerates. *Géotechnique Letters 3*, No. July-September (2013): 98-102.

Lim, W.L. (2004). *Mechanics of railway ballast behaviour.* Ph.D. Thesis, University of Nottingham, U.K.

Lim, W. L., McDowell, G. R., & Collop, A. C. (2004). The application of Weibull statistics to the strength of railway ballast. *Granular Matter,6*(4), 229-237.

Lim, W. L., & McDowell, G. R. (2007). The importance of coordination number in using agglomerates to simulate crushable particles in the discrete element method. *Géotechnique,* 57(8), 701-705.

Li, J., Langston, P.A., Webb, C. and Dyakowski, T. (2004) Flow of sphero-disc particles in rectangular hoppers- a Dem and experimental comparison in 3D. *Chemical Engineering Science* **54**, 5917-5929.

Li, Y., Xu, Y. and Jiang, S. (2009), DEM simulations and experiments of pebble flow with monosized spheres. *Powder Technology* **193** 312-318.

Lindqvist, M. and Evertsson C.M. (2004), Improved flow- and pressure model for cone crusher *Minerals Engineering* 17 1217-1225.

Lobo-Guerrero, S. & Vallejo, L. E. (2005). Crushing a weakgranular material: experimental numerical analyses. *Geotechnique* 55, No. 3, 245–249,

.Lu, M. and McDowell, G.R (2007), The importance of modelling ballast particle shape in DEM. *Granular Matter*, **9** No. 1-2 (2007) 71-82.

Lubachevsky, B. D., & Stillinger, F. H. (1990). Geometric properties of random disk packings. *Journal of Statistical Physics*, *60*(5-6), 561-583.

Mack, S., Langston, P., Webb, C., & York, T. (2011). Experimental validation of polyhedral discrete element model. *Powder Technology*, *214*(3), 431-442.

Mindlin, R. D., and H. Deresiewicz., (1953) "Elastic Spheres in Contact under Varying Oblique Forces," *J. Appl. Mech.*, *20*, 327-344.

McDowell, G. R., & Amon, A. (2000). The application of Weibull statistics to the fracture of soil particles. *Soils and foundations*, *40*(5), 133-141.

McDowell, G.R. and Bolton, M.D. (1998). On the micro mechanics of crushable aggregates. *Geotechnique* 48, No. 5, 667-679

McDowell, G.R. (2001) Statistics of soil particle strength. *Geotechnique* **51**, No.10, 897-900.

McDowell, G.R. and Harireche, O. (2002a). Discrete element modelling of soil particle fracture *Geotechnique* 52, No2, 131-135

McDowell, G.R. and Harireche, O. (2002b). Descrete element modelling of yielding and normal compression of sand. *Geotechnique* 52, No4, 299-304

McDowell, G.R., Li, H. and Lowndes, I. (2011) The importance of particle shape in discrete element modelling of particle flow in a chute. *Geotechnique Letters* 1, No. 3, 59-64.

McDowell, G., & de Bono, J. P. (2013). On the micro mechanics of one-dimensional normal compression. *Geotechnique ,63.* Volume 63, Issue 11, 895 –908

Napier-Munn, T. J., Morrell, S., Morrison, R. D., and Kojovic, T. (1996) *Mineral Comminution Circuits: Their Operation and Optimization*, Julius Kruttschnitt Mineral Research Centre, Indooroopilly, Queensland, Australia

Potyondy, D. O., & Cundall, P. A. (2004). A bonded-particle model for rock.*International journal of rock mechanics and mining sciences*, *41*(8), 1329-1364.

Potyondy, D. O. (2007). Simulating stress corrosion with a bonded-particle model for rock. *International Journal of Rock Mechanics and Mining Sciences*,*44*(5), 677-691.

Price, M., Murariu, V., & Morrison, G. (2007). Sphere clump generation and trajectory comparison for real particles. *Proceedings of Discrete Element Modelling 2007.*

Refahi, A., Aghazadeh, J., and Rezai, B. (2010) Discrete element modelling for predicting breakage behaviour and fracture energy of a single particle in a jaw crusher. International *Journal of Mineral Processing* 94 (2010) , 84-91

Robertson, D. (2000). *Numerical simulations of crushable aggregates*. Ph.D. Thesis, University of Cambridge, U.K.

Robertson D. and Bolton M.D. (2001). DEM simulations of crushable grains and soils. *Proc. Powders and Grains 2001. Sendai*, 623-626

Schöpfer, M. P., Abe, S., Childs, C., & Walsh, J. J. (2009). The impact of porosity and crack density on the elasticity, strength and friction of cohesive granular materials: Insights from DEM modelling. *International Journal of Rock Mechanics and Mining Sciences*, 46(2), 250-261.

Schwager T. and Pöschel T. (2007), Coefficient of restitution and linear–dashpot model revisited. *Granular Matter 9*, No. 6, 465–469.

Shipway, P.H. and Hutchings, I.M. (1993). Fracture of brittle spheres under compression and impact loading. I. Elastic stress distribution. *Phil. Mag. A* 67, No, 6, pp. 1309-1404

Tavarez, F. A., & Plesha, M. E. (2007). Discrete element method for modelling solid and particulate materials. *International journal for numerical methods in engineering*, *70*(4), 379-404.

Von Rittinger, P.R. (1867) *Lehrbuch der Aufbereitungs Kunde*, Ernst and Korn, Berlin.

Vu-Quoc, L., Zhang, X., and Walton, O.R., (1999) A 3D discrete element method for dry granular material flows of ellipsoidal particles. *Computer Methods in Applied Mechanics and Engineering.* 187(3), 483-528

Wang, L., Park, J, and Fu, Y., 2007. Representation of real particles for DEM simulation using X-ray tomography. *Construction and Building Material*, 21, 338-346

Weibull, W. (1951). A statistical distribution function of wide applicability. *J.Appl. Mech.* 18, pp. 293-297

Whiten, W.J.(1972) *Simulation and model building for mineral processing.* PhD Thesis, University of Queensland (JKMRC)

Wills, B.A. and Napier-Munn, T., (2006). *Wills' mineral processing technology: an introduction to the practical aspects of ore treatment and mineral recovery.* Butterworth-Heinemann.

Zhang, J.Y., Hu, Z., Li, T.H., Zhang, Y.J., Ge, W., and Li, J.H. (2004) Application of the disctete approach to the simulation of size segregation in granular chute flow. *Industrial & Engineering Chemistry Research*. Vol. 43(18): 5521-5528

Zhang, X., and Vu-Quoc, L. (2000). Simulation of chute flow of soybeans using an improved tangential force-displacement model. *Mechanics and Materials* 32, 115-129

Zhou, J., Su, Y. AND Chi Y. (2006). Simulation of soil properties by particle flow code, *Chinese Journal of Geotechnical Engineering*, Vol.28, No.3.